The Influence of Metal Oxide Transport Layer and Annealing Temperature on Perovskite Solar Cells (PSCs)

By

Lehlohonolo Petrus Lekesi

(BSc Hons)

A dissertation is submitted in fulfilment of the requirements for the degree

MASTERS IN PHYSICS

In the

College of Agriculture, Engineering and Science (AES)

School of Chemistry and Physics

At the

UNIVERSITY OF
KWAZULU-NATAL

INYUVESI
YAKWAZULU-NATALI

under Supervision of

Dr Thembinkosi Donald Malevu

Co-Supervisors

Prof T.E Motaung and DR B.P Gumbi

December 2021

Declaration

I Mr Lekesi L.P, hereby declare the following:

1. The research work presented in this dissertation has not been submitted to the University of KwaZulu-Natal or any other tertiary institutions for purpose of obtaining an academic qualification for myself or any party.
2. The information contained in this dissertation is my work and has entirely been written by myself and also I have made it my duty to acknowledge all sources of information used in the completion of this work.

Student details

Title : Mr

Names : Lehlohonolo Petrus

Surname : Lekesi

Email : hlonnylekesi@gmail.com
220111443@stu.ukzn.ac.za

_____ _____2022/02/17_____

(Signature) (Date)

Supervisor details

Title : Dr

Names : Thembinkosi Donald

Surname : Malevu

Email : malevu.td@gmail.com

_____ _____2022/01/17_____

(Signature) (Date)

Dedicated to my loving family

Acknowledgements

To my loving father thank you for looking after me until this point, thank you for the unconditional love, thank you for your faith in God and prayers. Without you, I can not imagine myself being a better person than who I am now. The childhood memories that you made for me reflect the person I am. I am sorry that I have always been absent from home throughout my academic journey and thank you for understanding that I am fighting for a better and brighter future. This journey is almost over, the struggle is almost over. God has plans for the family we shall also see better days and prosper. I pray to God that wherever life takes me you will enjoy the fruits of your child.

To my late mother and grandmother please know that I love you and I am working very hard to make you proud.

To my younger brother, I hope that in your eyes I am a role model.

To my supervisor Dr. Malevu. Thank you for extending the invitation to pursue my masters degree in perovskite solar cells. Thank you for the teachings and guidance you gave me. Thank you for the countless hours you spent with me in the lab to see to it that the research work becomes a success. I am very lucky and grateful to have a supervisor like you. You were more like an older brother to me. As I've fallen on my knees countless times and ready to give up, you always found a way to motivate and lift my spirits to keep working hard. Thank you for showing me that there good people in this world. This is the beginning of many more research projects.

I would also like to give thanks to UKZN physics department senior technician Miss Thabezhe. Thank you for making my presence in the department as a senior student appreciated.

Table of contents

List of Tables

List of figures

Abstract

Organic-inorganic halide Perovskite Solar Cells (PSCs) are the leading third-generation solar cells with the possibility to provide a fraction of green and affordable energy in the next technological era of solar energy. This type of photovoltaic cell is still new and has recently gained interest due to its low production cost, easy fabrication and rapidly improving power conversion efficiency (PCE). The performance of PSCs depends on the metal oxide/perovskite interface. This work focuses on improving the intermediate contact between the light-active perovskite layer and the electron transport layer (ETL) in a fully ambient PSC by annealing titanium dioxide (TiO_2) ETL at extreme temperatures. The TiO_2 semiconducting material was successfully synthesized using the hydrothermal method due to the method's ability to produce pure and crystalline nanoparticles at low temperatures. With the future application of TiO_2 projected to flexible conductive substrates, the as-synthesized TiO_2 nanopowders were preheated from 200 to 1200 ℃ temperature range prior to deposition to avoid substrate deformation. To investigate the effect of annealing on the synthesized TiO_2 nanopowders X-ray diffraction (XRD), transmission electron microscopy (TEM), Scanning electron microscopy (SEM), Energy dispersive x-ray (EDX) spectroscopy, Fourier transform infrared spectroscopy (FT-IR), and Ultraviolet-visible spectroscopy (UV-Vis) techniques were employed to study the structural, morphological, and opto-chemical property changes according to the temperature range described. From the crystal and morphology analysis, the as-synthesized TiO_2 nanomaterial appears to be a crystalline multiphase material showing coexistence of anatase and rutile phases. Annealing increases the metal oxide crystallinity, porosity, and particle dispersion. The optical analysis of TiO_2 material reveals successful bandgap tuning of the metal oxide wide-bandgap structure. The perovskite active layer was formed through the two-step spin coating of lead iodide (PbI_2) and methylammonium iodide (CH_3NH_3I) respectively. To investigate the morphological structure, thermal and optical properties of $TiO_2/CH_3NH_3PbI_3$ SEM, Thermogravimetric analysis (TGA), Photoluminescence spectroscopy (PL), and UV-Vis techniques were used. Finally, perovskite solar cells of device structure ITO/c-TiO_2/m-TiO_2/$MAPbI_3$/Spiro-MeoTAD/Conductive Ag ink/ITO were fabricated and their performance was evaluated using the Keithley solar simulator.

Chapter 1

Introduction.

1.1 Overview

The supply of energy is a driving factor that encourages economic growth and without the supply of energy in the form of electricity, there would be no changes in the world. This includes the industrialization of poor and developing countries. Concerning South Africa, the current energy resources are coal, petroleum, natural gas, nuclear, and renewables. With coal and oil being the leading energy resources [1]. According to the sustainable development goals, the shift to developing a greener energy supply is important to secure a future with the minimum negative impact caused by present actions [2]. Therefore, the use of renewable energy such as solar energy is an ongoing global scientific innovation with a target set to reach a 50% supply of energy in the next coming decades [3].

Photovoltaic (PV) technology is a promising alternative for green and affordable energy generation. This technology uses semiconducting materials to generate electricity from the abundant sunlight radiation. The major drawback in PV technology affecting its wide use in applications arises from the manufacturing cost and design of the commercially available silicon solar cells. Silicon-based solar cells are heavy and consume high capital during manufacturing causing silicon solar panels to be expensive in the niche market [4]. With the overarching aim to manufacture green and affordable solar energy new emerging perovskite solar cell (PSC) technology is underway. This emerging solar technology uses extremely thin perovskite light active semiconducting materials, producing efficiencies higher than any commercial solar panels [5]. PSCs are interesting PV devices, from the first component to the final device structure the device is fabricated from relatively easy low-temperature methods and affordable organic, inorganic, and transition metal oxide nanomaterials [6]. Similar to any solar technology PSCs are layered devices that consist of a perovskite material sandwiched between n-type and p-type semiconductors known to act as electron transporter and hole transporter respectively. **Figure 1.1** shows a simplified schematic representing the PSC device structure.

As represented in **Figure 1.1**, the nature of the n-type semiconductor and perovskite interface is similar to traditional PN-junction solar cells. Therefore, the performance of PSC devices depends on the electron collection from the light-active perovskite material by the n-type semiconductor [7]. Transition metal oxides such as TiO_2, ZnO, NiO, and Cu_2O are compatible n-type semiconductors due to their high surface area. maximum electron collection, easy synthesis methods, environmental friendliness, and less expensive nature. Among others, the

mesoporous nanostructure in TiO_2 renders TiO_2 an efficient n-type semiconductor in PSCs [8,9].

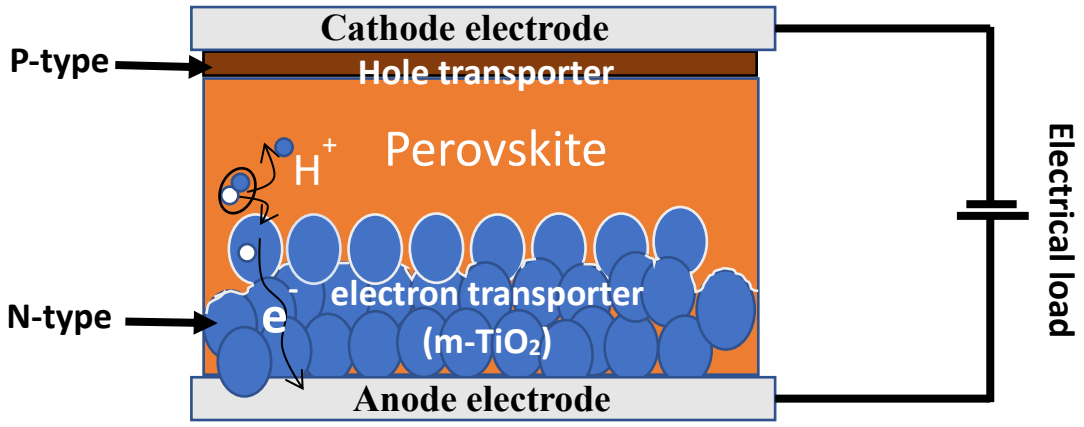

Figure 1.1: Simplifies representation of a PSC device structure.

1.2 Problem statement

The energy demand is an increasing global crisis. To meet the high energy demands the use of fossil fuels is constantly rising. However, the use of fossil fuels is risky as this means of energy generation produces toxic greenhouse gas emissions and also questions the sustainability, as fossils are constantly becoming depleted. While PV technology provides a sustainable and environmentally friendly means of energy generation there are still issues that need to be addressed to maximize PV solar cells globally. The new emerging PSCs are promising high efficiency and cost-effective devices. This type of PV solar cell is still new and lab-based, with only a decade in research and development. The issue of stability in PSCs is a major problem, with device lifespan approximated to be a few hours, days, weeks, and months depending on the fabrication laboratories with the necessary expensive equipment [10]. However, the PSC performance does not only depend on the light active materials only but it also depends on the intermediate contact with the electron transport layer (ETL). TiO_2 is a unique wide bandgap (3.0-3.2 eV) ETL. Successfully tuning TiO_2 nano-properties such as structure, morphology, optical properties is effective for improving the metal oxide/perovskite interaction.

1.3 Motivation statement

Green and affordable energy is essentially important to secure a future with sustainable electricity generated from the interaction of solar radiation/photons and electrons. Of course, the stability in the emerging PSCs is a major setback hindering the commercialization of the device currently. However, studies on the device performance such as the outstanding power conversion efficiencies motivate further development of the device. TiO_2 is a good photoanode

(or ETL) across many types of solar cells, to name a few dye-sensitized solar cells (DSSCs) and quantum dot solar cells (QDSCs). The TiO_2 photoanode can be synthesized into a variety of excellent nanostructures for solar cell applications ranging from nanorods, nanowires, and nanoparticles. Annealing of TiO_2 has been proven to alter the TiO_2 crystalline structure, morphology, and optical properties by encouraging phase transitions, increasing surface area, porous nature, and further decreasing the 3.0-3.2 eV wide-bandgap structure [11,12]. Such properties improve the nature contact of metal oxide ETL/perovskite interface contact reducing the electron recombination from the small bandgap perovskite (~1.5 eV).

1.4 Aims and objectives

1.4.1 Aims

This study aimed to fabricate a functional ambient perovskite solar cell based on the traditional $CH_3NH_3PbI_3$ light active material and indirectly optimize the device performance by investigating the effect of annealing titanium dioxide (TiO_2) metal-oxide electron transport layer.

1.4.2 objectives

The objectives of this study are as outlined as follows:

1. Synthesize titanium dioxide (TiO_2) nanoparticles by hydrothermal preparation method.
2. Investigate the effect of annealing on TiO_2 structural, morphological, and optical properties for solar cell applications.
3. Fabricate an open-air perovskite solar cell and characterize the influence of annealed TiO_2 nanoparticles on the device performance.

1.5 Thesis outline

1. **Chapter 1:** This chapter raises awareness of the current state of energy production and the impact it has on the environment and introduces the use of renewable energy as a sustainable development to secure a continuous supply of green and affordable energy.

2. **Chapter 2:** This chapter provides a literature review on perovskite solar cell theoretical background, the principle of operation, device architecture and fabrication techniques.

3. **Chapter 3:** This chapter gives detailed information on the preparation methods of TiO_2 nanoparticles, fabrication of the ambient perovskite solar cells, and characterization techniques used in this study.

4. **Chapter 4:** This chapter investigates the effect of annealing TiO_2 on the structural, morphological, and optical properties of TiO_2 nanoparticles.

5. **Chapter 5:** This chapter investigates the influence of annealed TiO_2 nanoparticles electron transport layer on perovskite solar cell performance.

Reference

[1] Pollet, B.G., Staffell, I. and Adamson, K.A. (2015) Current energy landscape in the Republic of South Africa. *International Journal of Hydrogen Energy*, Elsevier Ltd. **40**, 16685–701. https://doi.org/10.1016/j.ijhydene.2015.09.141

[2] Dincer, I. (1999) Environmental impacts of energy. *Energy Policy*, **27**, 845–54. https://doi.org/https://doi.org/10.1016/S0301-4215(99)00068-3

[3] Turner, J.A. (1999) A realizable renewable energy future. *Science*, **285**, 687–9. https://doi.org/10.1126/science.285.5428.687

[4] Lewis, N.S. (2007) Toward cost-effective solar energy use. Science (80-.). https://doi.org/10.1126/science.1137014

[5] Song, Z., Watthage, S.C., Phillips, A.B. and Heben, M.J. (2016) Pathways toward high-performance perovskite solar cells: review of recent advances in organo-metal halide perovskites for photovoltaic applications. *Journal of Photonics for Energy*, **6**. https://doi.org/10.1117/1.jpe.6.022001

[6] Ehtesham, A., Wong, W.W., Wong, H.Y. and Zaman, M. (2016) Recent advances in fabrication techniques of perovskite solar cells: A review. Am. J. Appl. Sci. https://doi.org/10.3844/ajassp.2016.1290.1314

[7] Cheng, M., Zuo, C., Wu, Y., Li, Z., Xu, B., Hua, Y. et al. (2020) Charge-transport layer engineering in perovskite solar cells. Sci. Bull. https://doi.org/10.1016/j.scib.2020.04.021

[8] Okada, W., Suga, T., Oyaizu, K., Segawa, H. and Nishide, H. (2019) Perovskite/TiO2 Interface Passivation Using Poly(vinylcarbazole) and Fullerene for the Photovoltaic Conversion Efficiency of 21%. *ACS Applied Energy Materials*, **2**. https://doi.org/10.1021/acsaem.9b00162

[9] Tiwana, P., Docampo, P., Johnston, M.B., Snaith, H.J. and Herz, L.M. (2011) Electron mobility and injection dynamics in mesoporous ZnO, SnO 2, and TiO2 films used in dye-sensitized solar cells. *ACS Nano*, **5**. https://doi.org/10.1021/nn201243y

[10] Chen, J., Cai, X., Yang, D., Song, D., Wang, J., Jiang, J. et al. (2017) Recent progress in stabilizing hybrid perovskites for solar cell applications. J. Power Sources. https://doi.org/10.1016/j.jpowsour.2017.04.025

[11] Muthee, D.K. and Dejene, B.F. (2021) Effect of annealing temperature on structural, optical, and photocatalytic properties of titanium dioxide nanoparticles. *Heliyon*, **7**, p.e07269. https://doi.org/10.1016/j.heliyon.2021.e07269

[12] Zhao, D., Peng, T., Lu, L., Cai, P., Jiang, P. and Bian, Z. (2008) Effect of annealing temperature on the photoelectrochemical properties of dye-sensitized solar cells made with mesoporous TiO2 nanoparticles. *Journal of Physical Chemistry C*, **112**.

https://doi.org/10.1021/jp800127x

Chapter 2

Developments on perovskite solar cells (PSCs): A Critical Review

Applied Sciences Editorial Office <applsci@mdpi.com> Fri, Dec 3, 2021 at 3:49 AM
Reply-To: angie.you@mdpi.com
To: Thembinkosi Malevu <Malevu.td@gmail.com>
Cc: Lehlohonolo Lekesi <hlonnylekesi@gmail.com>, Lehlohonolo Koao <koaoLF@ufs.ac.za>, Setumo Motloung <cchataa@gmail.com>, Tshwafo Motaung <motaungte@live.com>, Thembinkosi Malevu <thembinkosi.malevu@smu.ac.za>, Applied Sciences Editorial Office <applsci@mdpi.com>

Dear Dr. Malevu,

Thank you again for your manuscript submission:

Manuscript ID: applsci-1507883
Type of manuscript: Review
Title: Developments on Perovskite solar cells (PSCs): A Critical Review
Authors: Lehlohonolo Lekesi, Lehlohonolo Koao, Setumo Motloung *, Tshwafo Motaung, Thembinkosi Malevu *
Received: 29 November 2021
E-mails: hlonnylekesi@gmail.com, koaoLF@ufs.ac.za, cchataa@gmail.com, motaungte@live.com, thembinkosi.malevu@smu.ac.za

Your manuscript has now been reviewed by experts in the field. Please find your manuscript with the referee reports at this link:

https://susy.mdpi.com/user/manuscripts/resubmit/6e663fb2bfb0a178bdf8887d85d36469

Please revise the manuscript according to the referees' comments and upload the revised file within 10 days.

2.1 Overview

This review provides detailed information on perovskite solar cell device background and monitors stepwise scientific efforts applied on improving the device performance with time. The work reviews previous studies and latest developments in the perovskite crystal structure, electronic structure, device architecture, fabrication methods and challenges. Advantages such as easy bandgap tunability, low charge recombination rates and low fabrication cost are amongst those discussed. One of the most important elements highlighted in this review are concerns regarding commercialization and prototyping. By the way, perovskite solar cells (PSCs) are generally still lab-based devices suffering from drawbacks such as device intrinsic and extrinsic instabilities and also the rising environmental concerns due to the use of the toxic inorganic lead (Pb) element in the perovskite (ABX_3) light active material. Some interesting recommendations and possible future perspectives are well articulated.

Keywords: Perovskite solar cells, Chemical stability, Material toxicity, Device structure, Efficiency

2.2 Introduction.

PSCs are photovoltaic (PV) solar cells able to convert absorbed sunlight radiation to electricity. The cell operates similarly as a p-n junction, with the perovskite material producing electron-hole pairs for electricity generation. The PV solar cell is novel and has gained attention recently due to mainly its low production cost and easy fabrication [1–5]. PSCs offers a shift from overusing the earth non-renewable resources to harvesting the infinite sunlight supply. The world is in great demand of energy in the form of electricity, as it contributes to economic growth [6]. However, depending on burning fossil fuel for this purpose is consequential, as fossils are slowly becoming depleted and emit harmful toxins in the atmosphere [7,8]. Therefore, resorting to renewable energy such as solar energy offers the advantage to counteract both issues of energy supply and negative impact on the environment. Hence resources that generate electrons for the above purposes are promising alternative sources of energy.

2.3 Perovskite Solar Cells (PSCs).

PSCs belong to the 3rd generation of photovoltaic cells, with their device structure integrated from the dye-sensitized solar cells (DSSCs) configuration [9,10]. Because of the low absorption coefficient of organic sensitizers in DSSCs, this limits the light-harvesting ability of the cell hence DSSCs are low-efficiency cells. Kojima [2009] studied the PV effect in a photoelectrochemical (PEC) dye-sensitized cell by replacing the dye organic molecules with organic-inorganic halide perovskite molecules such as $CH_3NH_3PbBr_3$ ($MAPbBr_3$) and $CH_3NH_3PbI_3$ ($MAPbI_3$) and registered power conversion efficiencies (PCE) of 3.1% and 3.8% respectively [2]. Although the perovskites show good PV properties including optical, excitonic and electrical conductivity the above unfavourable low efficiencies are due to the dissolution of the perovskite material by the liquid electrolyte [11].

Attempts have been made to stabilize the crystalline perovskite material in DSSCs. Lee [2009] reported an increase in PCE of lead halide perovskites while many researchers focused on quantum dot sensitized solar cells (QDSSCs) using inorganic metal chalcogenides sensitizers such as PbS, CdSe, and CdS as light-absorbing materials exhibiting intense bandgap light absorption [12–14]. However, the quantum dot cells suffered from low efficiencies between 1.2-6.4% due to charge recombination at the interface and chemical instability. To overcome the challenges, the $MAPbI_3$ perovskite materials were explored as quantum dots in PECs and an increase to 6.5% in PCE was achieved [15]. To further increase the efficiencies in PECs Fujishima [2005] proposed the use of hole transport materials (HTMs) in DSSCs to eliminate the drawbacks caused by the liquid electrolytes. In a later study, Lee [2012] developed a 10%

PCE solid-state perovskite solar device using Spiro-MeOTAD HTM in a dye-sensitized perovskite cell [16,17].

Device fabrication of a solid-state PSC consists of a perovskite precursor solution deposition between spaces of mesoporous titanium dioxide (TiO_2) thin-film on a transparent conductive oxide (TCO) substrate forming a ABX_3 perovskite layer by an ordered ion agglomeration process then followed by Spiro-MeOTAD (HTM) deposition resulting in device reaching efficiencies of up to 9.7% (See **Figure 2.1 (a)** and **(b)**). The use of mixed halide perovskite crystals such as $MAPbI_{3-x}Cl_x$ helps avoid the dissolution of the perovskite material by the Spiro-MeOTAD dissolving solvents during the deposition [18,19]. It is further found that the use of insulating mesoporous aluminium oxide (Al_2O_3) instead of mesoporous TiO_2 results in better PCE. The Al_2O_3 appears to act as a structural scaffold in the perovskite material demonstrating that the ABX_3 perovskite crystal structure contributes to the electron transport, hence demonstrating devices with high charge collection (see **Figure 2.1 (c)**) [20–22]. The reduction in device thickness shown in **Figure 2.1 (d)** to **(g)** from the sensitized cell structure to the mesoporous structure, leading to meso-superstructure, and lastly the planar cell structure has also contributed to achieving high photon to electron efficient thin-films.

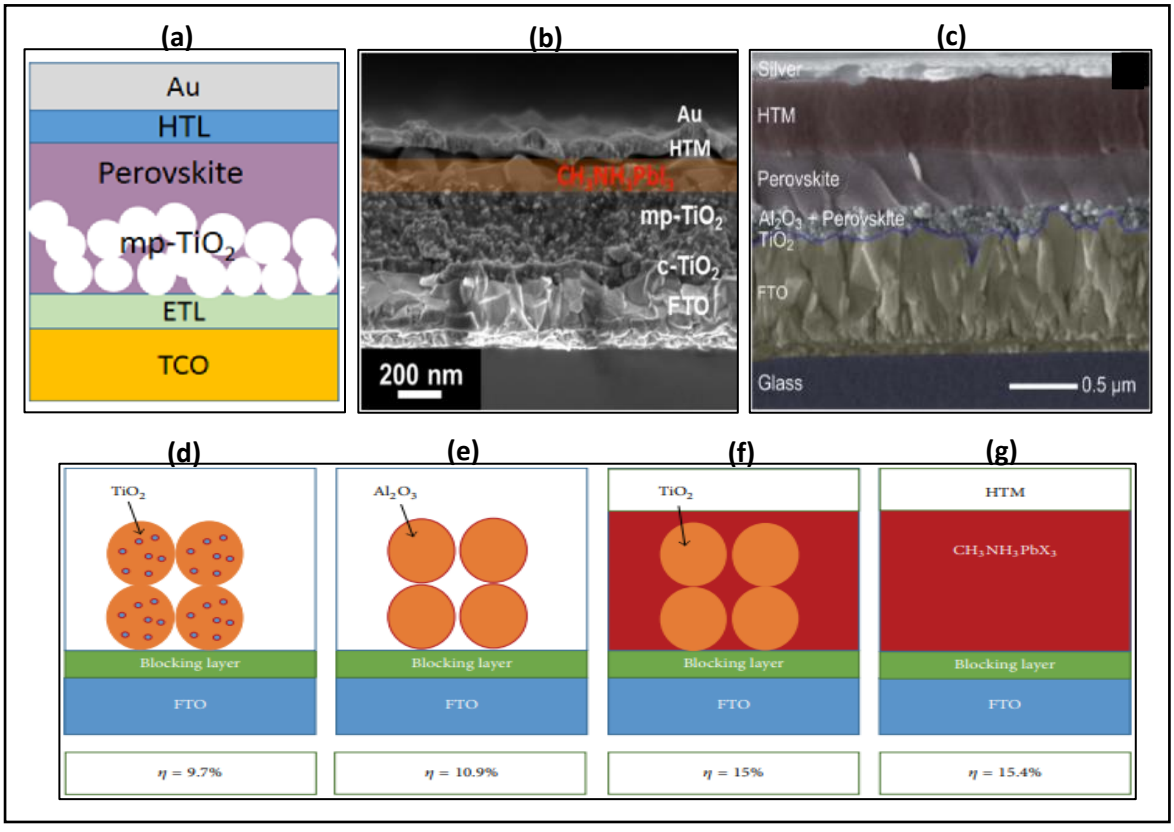

Figure2.1: (a) Schematic representation of a solid state perovskite sensitized device structure. SEM cross-sectional images of PSCs based on mesoporous, **(b)** TiO_2, and **(c)** Al_2O_3. Progress in PSC efficiency with the cell structure (η): **(d)** sensitized PSC η=9.7%, (e) mesoporous PSC η=10.9%, (f) meso-superstructure PSC η=15%, and (g) planar heterojunction thin-film PSC η=15.4% [9,10,20,22].

The developments in designing the ABX_3 crystal structure and advances in device structure is of topical research, attracting the interest of many chemists and physicists across the world. This has attributed a rapid increase in PSC efficiencies towards its theoretical Shockley-Queisser limit of ~27% and efficiencies above the traditional inorganic solar cells [23,24]. However, PSCs are still lab-based devices and have not reached commercialization due to the device instabilities and the current use of the harmful inorganic lead (Pb) element. Factors affecting the PSC's stability include environmental variations such as oxygen, light, moisture, temperature, and UV [25–27]. Thus, the major challenge in manufacturing PSCs is achieving a device with a high-performance, environmentally friendly, and a life span approaching 25 years.

The perovskite active layer together with the counter electron and hole transporting layer (HTL and ETL) are key components in the solar cell device [28]. Therefore, this work provides comprehensive literature on perovskite crystal structure modelling, perovskite (ABX_3) compositional engineering, and maps out the road towards establishing the perfect required ETL/perovskite and perovskite/HTM intermediate contacts [29,30]. Interesting recommendations and possible future perspectives are also outlined.

2.4 Modelling the perovskite crystal structure.

In perovskite solar cells $MAPbI_3$, $FAPbBr_3$ and $CsPbCl_3$ are standard ABX_3 light-absorbing layers [31]. The arrangement of ions in the absorber crystal structure varies in space around the unit cell depending on temperature (T), pressure (P) and tolerance factor (t). The shape of the crystal structure ranges from orthorhombic, tetragonal and cubic in order of increasing crystal perfection, respectively [32]. The tolerance factor (t) predicts stability in perovskite crystal systems. In a perfect cubic structure (t) factor equals 1.0, whereas in a non-ideal case the cubic structure is within 0.8 to 1.0 (t) factor. Less ordered crystal structures such as orthorhombic and tetragonal are obtained at low (t) factor [19,26]. FA^+ containing perovskite layers have a high (t) factor. Metal alloys of MA^+ and Cs^+ multi-cation perovskites result in materials with properties comparable to FA^+ alone. This concluding that FA^+ containing perovskites are more stable than individual MA^+ and Cs^+ containing perovskite materials [33]. **Figure 2.2** shows $MAPbI_3$ phase transitions with an increase in temperature. The (t) factor equation is given as follows.

$$t = \frac{r_A + r_X}{\sqrt{2}\,(r_B - r_X)} \qquad (1)$$

where r_A, r_B and r_X represent the ionic radii for the organic cation A, inorganic cation B and the halide anion X, respectively [31].

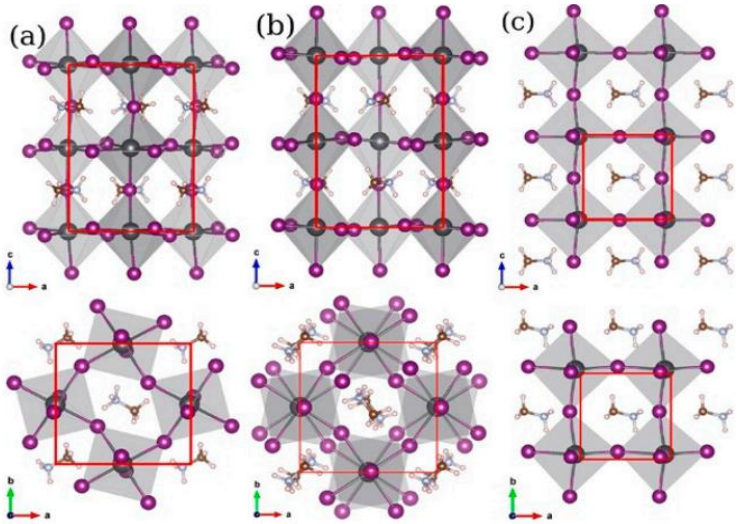

Figure 2.2: $MAPbI_3$ phase transitions arranged in order of increasing temperature (a) orthorhombic, (b) tetragonal and (c) cubic perovskite phases [26].

2.5 Modelling the perovskite electronic structure.

Methylammonium lead iodide ($MAPbI_3$) is the simplest and well-studied perovskite absorber compound. Its crystal structure consists of an organic MA^+ molecule surrounded by a 3-dimensional inorganic Pb-I molecule. **Figure 2.3 (a)** to **(c)** and **(d)** to **(f)** represent the electronic structure of $MAPbI_3$ showing the effect of 001-, 110- and 111-MA^+ ion orientations in a cubic and tetragonal $MAPbI_3$ crystal system respectively. It is observed that the conduction (CB) and valence (VB) band of the $MAPbI_3$ electronic structure vary with MA^+ orientation however the overall electronic bandgap remains the same throughout 001-, 110- and 111-MA^+ orientations. This leads to the suggestion that the material's bandgap energy (E_{gap}) depends on the 3D Pb-I system surrounding the MA^+ ion and not on the MA^+ ion [17,33–35]. In an additional study on $MAPbI_3$ electronic structure, Yin [2014] studies on the density of states (DOSs) emphasizes more on the above suggestion. **Figure 2.3 (g)** to **(j)** illustrates $MAPbI_3$ total and partial DOSs. It is observed from the DOS positions of lead (Pb) and iodide (I) p-orbitals in **Figure 2.3 (i)** and **(j)** occupy the CB and VB respectively indicating that $MAPbI_3$ optical transitions rely on Pb and I p-p transitions (see **Figure 2.3** (**g**)) [34,36].

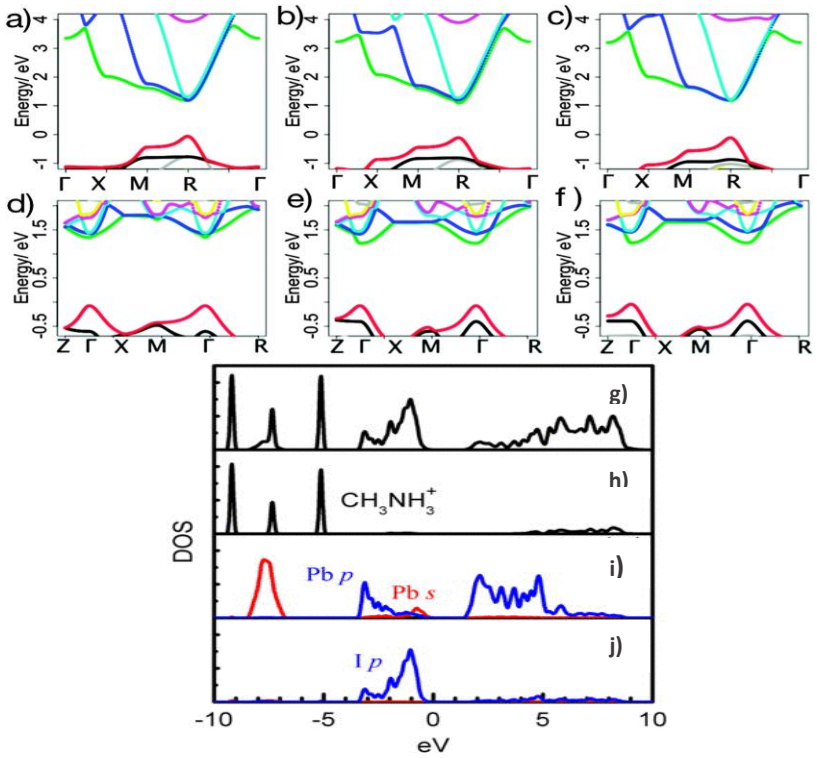

Figure 2.3: Band gap structure of a cubic **(a)** to **(c)** and tetragonal **(d)** to **(f)** $MAPbI_3$ crystal structure. Total and partial density of states of MAPbI3 and ions **(g)** to **(j)** [34,35].

2.6 Perovskite solar cell device architecture.

PSCs were first reported by Kojima [2009] whereby the perovskite ABX_3 organic-inorganic lead halide material was used as a light absorber in sensitized solar cells. In this study, the perovskite device structure preserved the same cell structure as DSSCs. Hence assumed that PSCs operate similar to DSSCs. However, as knowledge developed in this field, it is found that the fundamental basis of operation in PSCs is distinctive to DSSCs [15,17]. In a PSC device, the perovskite material (ABX_3) is deposited onto a conductive glass substrate bearing an n-type (compact or mesoporous) electron transport material (ETM) which is followed by the deposition of a p-type hole transport material (HTM). When light is absorbed by the perovskite material, electrons are excited to the LUMO leaving behind holes in the perovskite HOMO generating excitons that diffuse within the perovskite layer towards the opposite ETM and HTM contacts. At the interface with the perovskite material, the ETM and HTM selectively transport charge carriers. Electrons then travel from the anode electrode (TCO) to the external circuit generating electricity across an electrical load. The perovskite absorber regenerates as electrons recombine with holes at the cathode electrode (e.g., Au, Ag, Pt, and Al) minimizing charge imbalance at opposite electrodes [37].

A conventional PSC has a device architecture similar to a p-n junction solar cell with the perovskite intrinsic (i) absorber sandwiched between n-type and p-type semiconducting materials as illustrated in **Figure 2.4 (a)** referred to as the mesoscopic-(n-i-p) device architecture. The realization that the perovskite on its own is dominant in transporting electrons and holes and the rearrangement in device architecture has also led to enhanced device performance [38]. **Figure 2.4 (b)** to **(d)** illustrates schematic images of such devices which are referred to as planar-(n-i-p), planar-(p-i-n), and mesoscopic-(p-i-n) respectively. The planar-(n-i-p) architecture results from PSC devices without the mesoscopic metal oxide required in DSSCs as a structural scaffold. A planar architecture is a promising architecture for large surface area manufacturing on flexible substrates because they are fabricated from low-temperature preparation methods [39]. The planar-(n-i-p) devices are reported to reach high efficiencies of up to 23.6% slowly approaching the 25.5% of mesoscopic-(n-i-p) architecture. Although the (n-i-p)-devices demonstrate high PCE, their stability still suffers due to negative impacts (e.g., degradation) imposed on the perovskite layer by the acidic and hydrophilic nature of the traditional Spiro-MeOTAD and PEDOT:PSS HTMs [26,40,41]. The (p-i-n)-planar and mesoscopic architecture are inverted architectures of the conventional-(n-i-p) whereby the sequence of deposition is reversed. The inverted architecture partially overcomes the above-stated instability issues by reducing the corrosive effect of the HTMs on the device active layer.

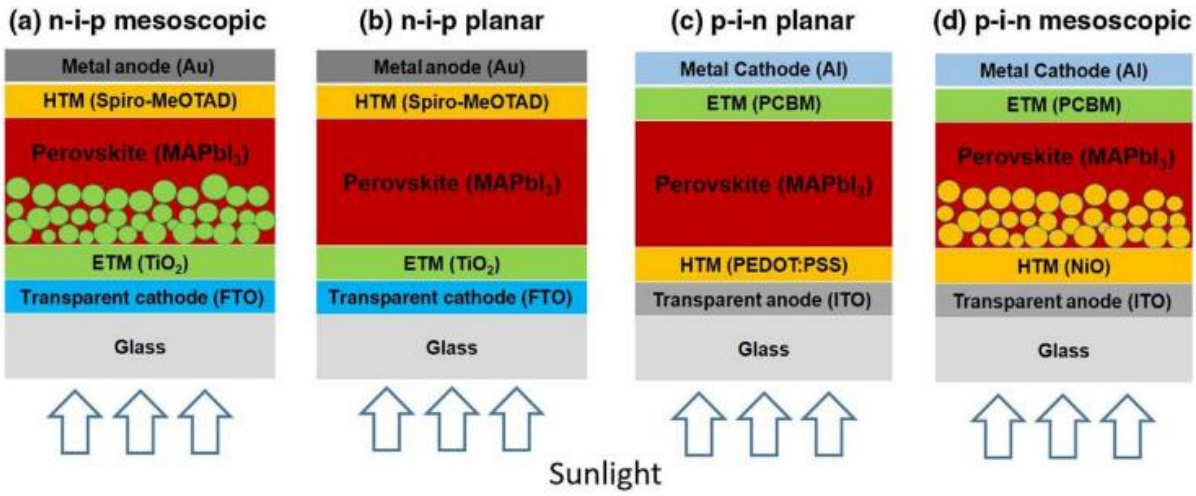

Figure 2.4: (a) and **(b)** represent a simplified image of a PSC conventional n-i-p device architecture. **(c)** and **(d)** represent an inverted p-i-n PSC device architecture [38].

Optimizing the device thickness by removing the mesoporous ETM and the change in device architecture has shown to be efficient for high-performance PSCs. Another significant route for improving the device PCE and operational stability lies in designing the perovskite ABX_3 composition using simple chemical approaches. Over the past years of research in PSCs, significant milestones have been reached through the ABX_3 design. **Figure 2.5** shows the basis of ABX_3 designing. **Figure 2.5 (a)** and **(b)** presents the initial IPCE and I-V characteristic performance based on $MAPbI_3$ and $MAPbBr_3$ single halide perovskites, the distinctive difference in the iodide and bromide performance presented sufficient motivation in achieving hybrid materials of organic-inorganic perovskite materials through ABX_3 designing [2]. From

the IPCE curve, $MAPbBr_3$ (solid line) shows a photon to current conversion ratio of 62- 65% at wavelengths less than 550 nm however change behaviour at higher wavelengths indicating that $MAPbBr_3$ is most active at lower wavelengths. Whereas $MAPbI_3$ (dash line) shows a 45% conversion rate over a wide wavelength range of 450- 750 nm. The good short circuit current of 10.8 mAcm-2 in $MAPbI_3$ and open-circuit voltage of 0.94 V in $MAPbBr_3$ in the corresponding I-V curve is attributed to the long-wavelength IPCE ratio in $MAPbI_3$ and good electron transfer between the active layer's LUMO and ETM's conduction band in $MAPbBr_3$, respectively. This study paved a path for a multitude of ideas in varying the perovskite ABX_3 crystal structure resulting in hybrid mixed halide, mixed cation. all organic, all-inorganic perovskite light active thin-films.

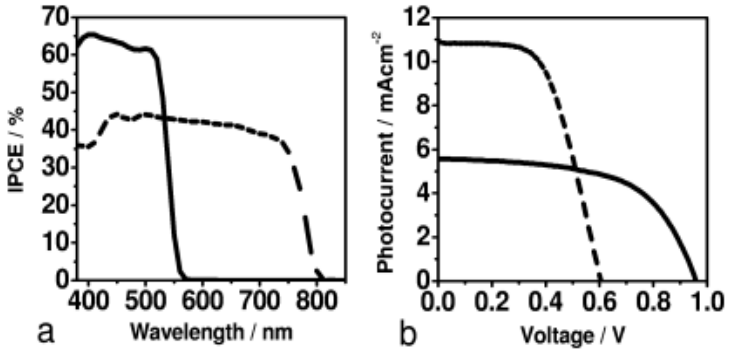

Figure 2.5: (a) IPCE and **(b)** I-V curve for $MAPbBr_3$ (solid line) and $MAPbI_3$ (solid line) [2].

Hybrids of mixed halide PSCs result in synergistic properties not obtained in single halide PSCs. Docampo [2013] compared the optical and PV properties of planar $MAPbI_3$ single halide and planar $MAPbI_{3-x}Cl_x$ mixed halide PSCs prepared via solution dip coating of PbI_2 thin-films into precursor solutions containing MAI plus the addition of MACl at a controlled concentration ratio (wt%) as shown in **Figure 2.6 (a)**. It is observed that the PSC performance increases in mixed halide perovskite systems. In the time-resolved photoluminescence results reported in **Figure 2.6 (b)** the planar $MAPbI_3$ device exhibit a short photoexcitation lifetime minimizing the charge carrier diffusion length in the relatively thick $MAPbI_3$ film. Remarkably it is observed that the inclusion of Cl at small wt% into the $MAPbI_3$ composition increases the charge carrier lifetime resulting in diffusion lengths that are a few nanometers greater than the resulting $MAPbI_{3-x}Cl_x$ thickness. Corresponding I-V results are reported in **Figure 2.6 (c)**, the mixed halide $MAPbI_{3-x}Cl_x$ PSC reaches maximum short circuit current (J_{sc}) and efficiency (η) values of 22.9 $mAcm^{-2}$ and 15.41% in comparison to the low PV parameters in single halide $MAPbI_3$. This improved PSC performance is suggested to be attributed to the small average crystal sizes and minimum grain boundaries within the mixed halide, promoting higher diffusion lengths. This study indicates that further addition of the second halide component (Cl) slightly decreases the device short circuit current and open-circuit voltage from maximum therefore optimization in the preparation method is required for optimum device performance [21].

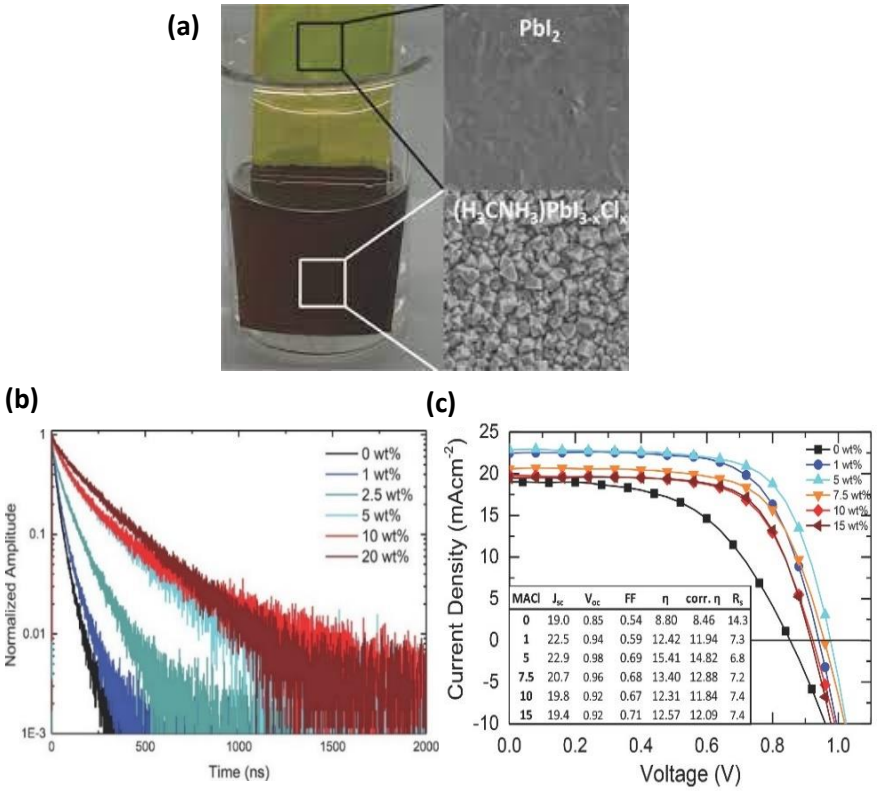

Figure 2.6: (a) Solution dip-coating preparation method for the perovskite films and the corresponding surface morphologies in PbI_2, $MAPbI_{3-x}Cl_x$, and/or $MAPbI_3$ thin-films. (b) Time-resolved photoluminescence spectrum and (c) photovoltaic performance in planar heterojunction solar cells of $MAPbI_3$ and $MAPbI_{3-x}Cl_x$ at various wt% addition of MACl [21].

Table 1.1: Types PSCs with device architecture "TCO/ETM/Perovskite layer/HTM/metal contact" varied by the perovskite layer, ETM and HTM [2,21,30,41–50].

Device variations	**`Type**	**V_{oc}**	**J_{sc}**	**FF**	**PCE**	**Year**	**ref**
Single halide PSC	FTO/ m-TiO_2/$MAPbBr_3$ /LiBr|Br_2/Pt-FTO	0.96	5.57	59.0	3.13	2009	2
	FTO/m-TiO_2/$MAPbI_3$/HTM/ LiI|I_2/Pt-FTO	0.61	11.0	57.0	3.81	2009	2
Mixed halide PSC	ITO/PCBM/$MAPbI_{3-x}Cl_x$ /Spiro-MeOTAD/metal contact	0.97	17.9	70.0	12.2	2013	20
	FTO/TiO_2/$MAPbI_{3-x}Cl_x$ / PTAA/ Au	1.10	21.4	77.6	18.3	2016	40
	ITO/ETM/ $MAPb(Br_xI_{1-x})_{3-y}Cl_y$ /HTM/metal contact	1.05	10.01	70.0	8.7	2014	41
Mixed cations	FTO/co-TiO_2/mp-TiO_2/ $(FAPbI_3)_{0.85}(MAPbBr_3)_{0.15}$/ Spiro-MeOTAD/ Au	1.15	22.7	76.0	20.2	2016	29
	FTO/c-TiO2/m-TiO_2/Cs/FA/MA/Spiro-MeOTAD/Au	1.14	23.6	77	20.8	2017	42
	$(Rb_{0.1}Cs_{0.05}FA_{0.85})Pb(I_{1-x}Br_x)$	1.15	22.2	73.0	18.7	2016	43
Metal Oxide (ETM)	ITO/TiO_2/$MAPbI_{3-x}Cl_x$/Spiro-MeOTAD/Ag	0.95	21.4	60.0	12.2	2014	44
	ITO/ZnO/$MAPbI_3$/Spiro-MeOTAD/Au	0.87	19.2	67.6	11.3	2016	45
	FTO/NiO/$MAPbI_{3-x}Cl_x$/PCBM/Al (inverted)	0.97	15.89	57	8.78	2014	46
HTM	FTO/ETM/ $FA_{0.8}MA_{0.1}Cs0._{01}$/Spiro-MeOTAD/Au	1.16	21.5	73.0	18.1	2017	47
	ITO/ PEDOT:PSS /$MAPbI_{3-x}Cl_x$/PCBM/Ag (Inverted)	1.11	20.11	80.6	16.5	2018	48
	FTO/c-TiO_2/m-TiO_2/MAPbI3/TTF/Ag	0.86	19.9	64.4	11.0	2012	49

Further to the ABX_3 designing, processing conditions such as thermal annealing, ageing, doping, moisture and solvent treatment are strategies used to optimize device performance during PSC fabrication. Adhyaksa [2016] studied the effect of ageing (a device placed in the dark at room temperature) on the diffusion length and bandgap energy of mixed $MAPb(I_{1-x}Br_x)_3$ halide perovskite. **Figure 2.7 (a)** shows a plot of the mixed perovskite diffusion length L (nm) against bandgap energy (eV) values, the insert images are the aged PSC thin-films arranged according to their bandgap energies, the white and black dots present corresponding diffusion length and bandgap values for aged and non-aged PSCs films, respectively. It is noted in both cases that the bandgap structure is tuned by varying the bromine (Br) and iodide (I) weight fractions. Bandgap values in the thin films increase with increasing Br content. A distinctive phase change is observed by colour change towards high bandgap values from black to yellow, indicating that the devices can be optimized to absorb specific regions in the solar spectrum. The aged film at ~1.8 eV recorded the highest diffusion length, double of the non-aged films. This study, therefore, shows that the application of processing conditions on either single or mixed halide perovskite thin films offers the ability to fine-tune the resulting perovskite optical properties for better and desired performances [28,51].

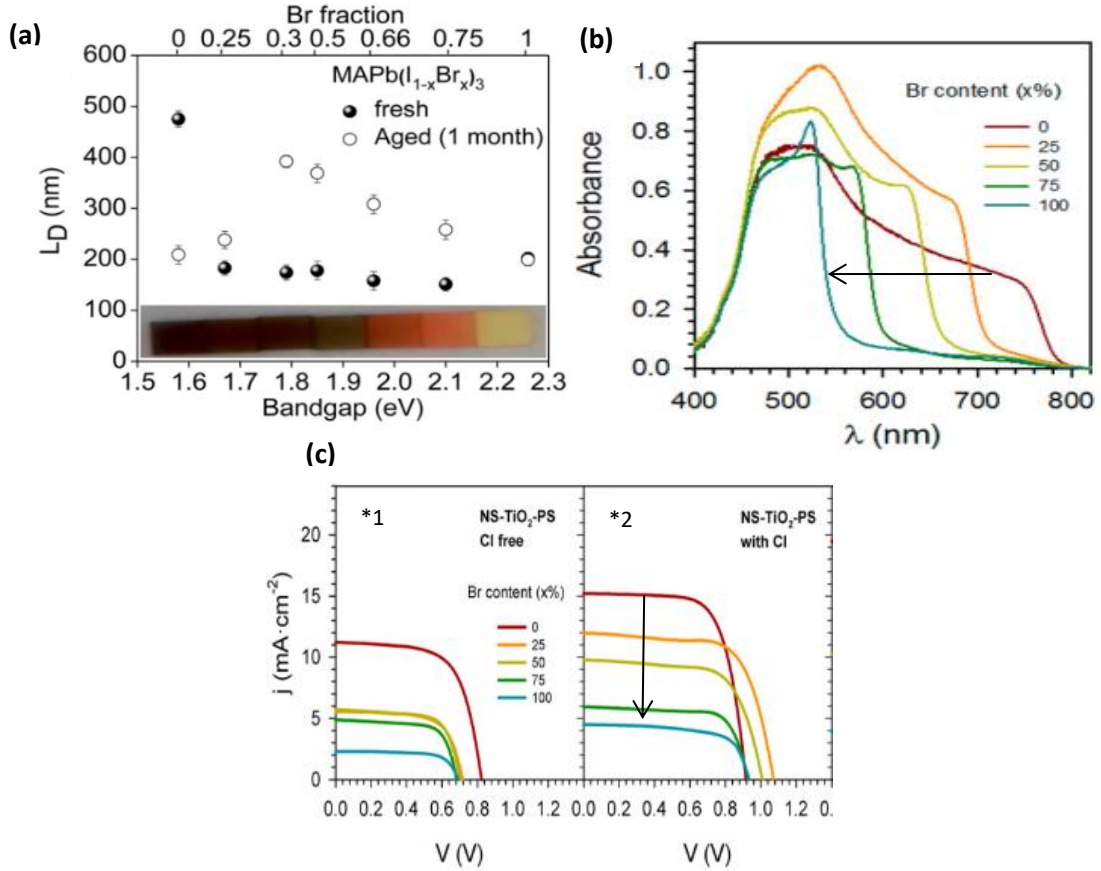

Figure 2.7:(a) A plot of diffusion length (L nm) against bandgap energies of aged and non-aged $MAPb(I_{1-x}Br_x)_3$ perovskite thin films, **(b)** Absorption spectra of mixed halide perovskite film, **(c)** I-V curve in a hybrid mixed halide PSC [28,45].

In a similar study Suarez [2014] characterized the effect of halogen (x%= I, Br, and Cl) composition in mixed halide PSCs optical and PV properties. In **Figure 2.7 (b)** a shift towards lower wavelengths is observed in the absorption spectra as indicated by the arrow. This absorption behaviour further confirms the successful bandgap tunability in **Figure 2.7 (a)** reported above with an increase in Br(%) ratio [45]. In **Figure 2.7 (c)*1** a significant reduction in device performance is observed due to the low J_{sc} and V_{oc} values. This is attributed to the shift towards lower wavelengths observed from the reported absorption spectra. **Figure 2.7 (c)*2** shows an appreciable increase in J_{sc} and V_{oc} with the introduction of a third halogen (Cl) component. However, the shift in absorption further persists to decrease the device performance in the triple halide PSCs.

The complex perovskite crystal structure ABX_3 offers the advantage off composition modelling the resulting absorber layer by stochiometric solution preparation methods [52,53]. Singh [2017] studied cell properties of a mixed cation (Cs/FA/MA) perovskite device and obtained characteristic results of a PSC with the device configuration FTO/TiO_2/Meso-TiO_2/Cs/FA/MA/Spiro-MeOTAD/Au as shown by the cross-sectional image in **Figure 2.8 (d)** [46]. In previous studies of MA/FA perovskite thin-films, it is reported that the MA^+ cation at small ratiosratio acts as a FA^+ nucleating site, increasing the degree of crystallinity in the FA photoactive film. Thus, also enhancing the light sensitivity of thein FA film.$^+$ thin-films. However, MA/FA system showed traces of small phase impurities that eventually affect the overall morphology and stability. It is reported that the incorporation of cesium (Cs) inorganic cation improves MA/FA intrinsic properties [54,55].

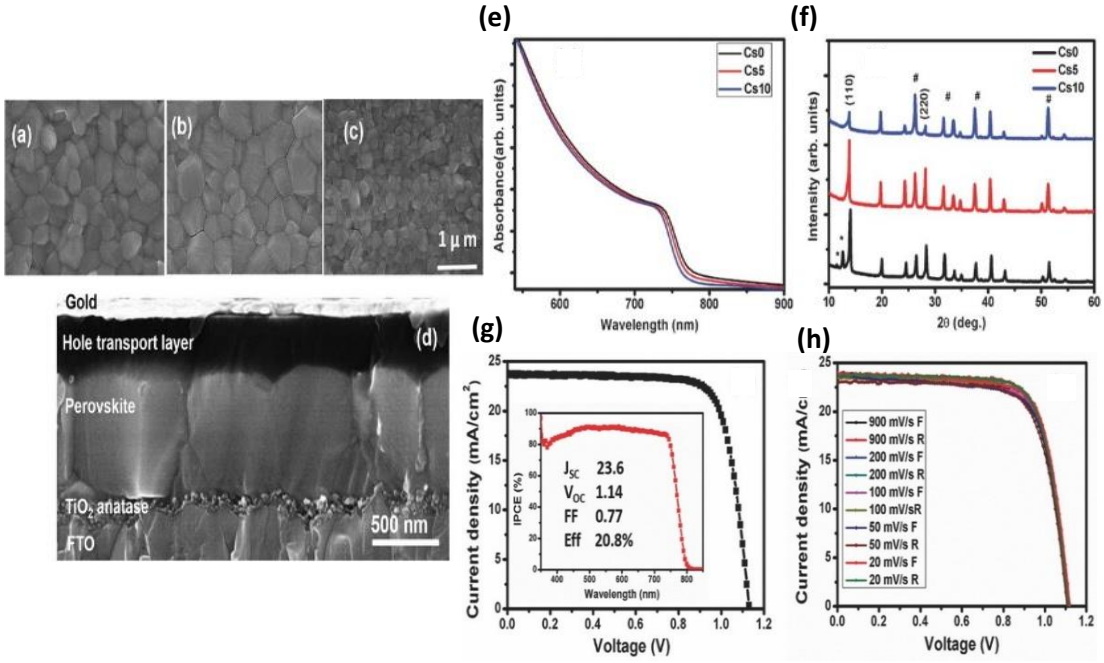

Figure 2.8: Characteristic performance of triple cation perovskite solar cell. (a-d) SEM micrographs images, **(a)** Cs0/MA/FA, **(b)** Cs5/MA/FA, **(c)** Cs10/MA/FA and **(d)** cross-sectional area at Cs5/MA/F, **(e)** characteristic perovskite absorption spectrum, **(f)** XRD

pattern of Cs/MA/FA at 0, 5 to 10 wt% Cs addition, **(g)** I-V curve of the best Cs10/MA/FA device and the insert represents the device corresponding IPCE, and (h) J-V hysteresis effect on I-V scans [46].

Figure 2.8 (a) shows SEM micrograph image of a neat MA/FA system with a bumpy distribution of grains and the presence of surface grooves indicating a low level of adhesion between grain interfaces, in **Figure 2.8 (b)** at 5wt% addition of Cs the crystal grains increase in size and the surface boundary between the grain becomes diluted, this might suggest an improved surface adhesion between grains and hence high degree of crystallinity. However, at high additions of 10wt% Cs indicated in **Figure 2.8 (c)** the surface adhesion disappears, and grains are reduced to smaller particle size increasing the possibility of crystal defects. **Figure 2.8 (e)** shows characteristic absorption band of a perovskite absorber layer with absorption over UV-vis spectrum. **Figure 2.8 (f)** shows XRD patterns at 0, 5 to 10wt% Cs addition all showing perovskite characteristic peak at ~14° diffraction angle corresponding to the (110) plane. Defect peaks at diffraction angels lower than 14° are seen for the neat MA/FA system, this might be assigned to the groove boundaries between grains. At 5wt% Cs addition the defect peaks disappear and a significant increase in perovskite peak intensity at 14° diffraction angle suggesting an increase in crystallinity. This behaviour is however not favoured for higher concentrations of Cs addition. The inorganic Cs metal encourages crystallization and increases the device stability as shown in **Figure 2.8 (f)** and **(h)** by the occurrence of little to no J-V hysteresis effect between forward and reverse bias connections.

Electricity is generated by the direct absorption of sunlight in a PV solar cell. The absorbed light creates electron-hole pairs (excitons) in the absorber layer, electrons are then collected at the anode electrode to the external circuit and through an electrical load. Electrons are thereafter reinjected into the absorber layer by a cathode counter electrode where recombination with holes occurs. The energy difference of the electron at the anode and cathode is used to determine the open-circuit voltage (V_{oc}) [56]. **Figure 2.9 (a)** underlines the basic cell operation of a perovskite solar cell. Nagarjuna [2015] studied the effect of transporting materials in a perovskite solar cell and reports that the correct choice of cell transporting material is at most necessary for better PCE, FF and V_{oc} [57]. A compatible transporting material should have high charge extraction, high mobility and proper energy alignment with the absorber layer at their interface as indicated in **Figure 2.9 (b)**. The traditional materials used as ETM and HTM in PSCs include titanium dioxide-(TiO_2) and Spiro-MeOTAD. Other common alternatives such as aluminium oxide (Al_2O_3), zinc oxide (ZnO), and PCBM are used as ETMs while copper iodide (CuI), nickel oxide (NiO), PEDOT: PSS, poly(triarylamine) (PTAA) materials are common alternative HTMs.

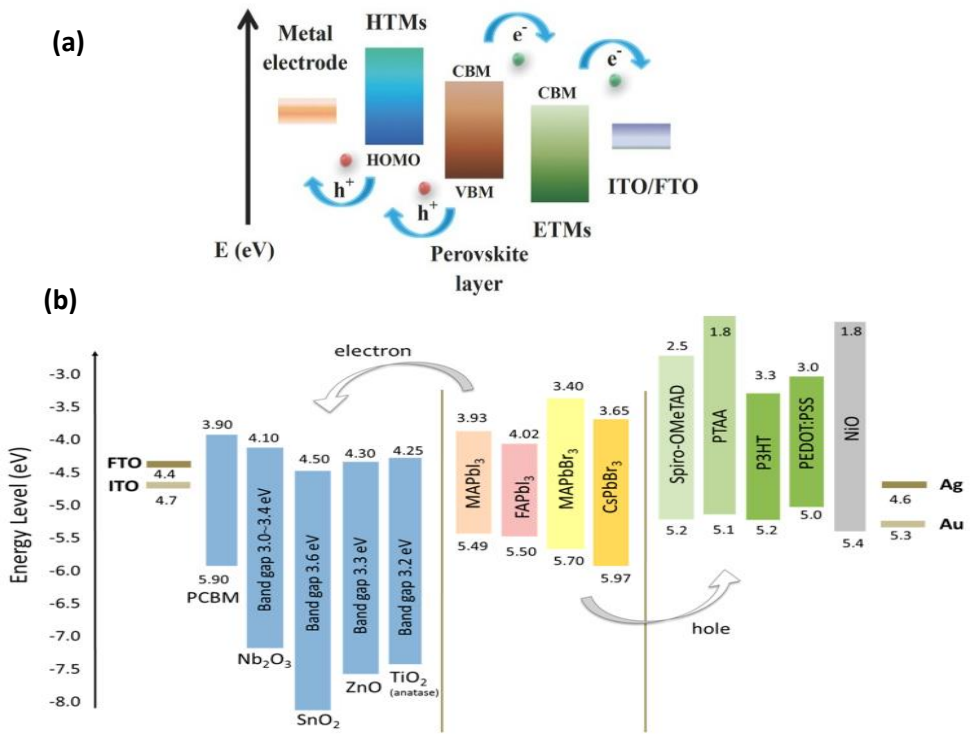

Figure 2.9: (a) Schematic diagram showing the basic device operation in a PSC. **(b)** Simplified energy alignment of possible ETM and HTM materials in PSC applications [19,30].

2.7 Fabrication methods

As already discussed PSCs has taken many routes to achieve high performances such as the device transition from sensitized solar cells to the recent planar thin-film solar cells, preparation of hybrid perovskite light active materials, the use of processing conditions and lastly the use of different charge ETMs and HTMs. In addition, PSC fabrication methods play a role in high-quality perovskite materials.

2.7.1 One-step method

The one-step deposition method involves spin-coating a perovskite precursor solution onto a pre-treated transparent conductive oxide (TCO) substrate followed by annealing to form the perovskite active layer as shown in **Figure 2.10 (a)**. This is the widely used deposition method due to its simplicity and low production cost for small lab-based PSCs and is not suitable for large surface area device fabrications. To form a perovskite layer of crystal structure ABX_3, organic (e.g., MAI/FAI) and inorganic (e.g., PbX_2,/SnX_2) halides are dissolved into a common dipolar aprotic solvent such as dimethyl sulfoxide (DMSO),

dimethylformamide (DMF), and γ-butyrolactone (GBL) then spin-coated on an ETM bearing conductive substrate. The early PSC fabrication that triggered research interest was achieved through one-step spin-coating solutions of organic salts (MABr and MAI) and inorganic salts ($PbBr_2$ and $PbCl_2$) reporting efficiencies of 3.31% and 3.81% in the resulting $MAPbBr_3$ and $MAPbI_3$ PSCs, respectively [2]. In a later study, Miyasaka [2012] reported PCE of up to 10.9% by spin-coating a solution of mixed halide perovskite precursor over a mesoporous Al_2O_3 scaffold [4].

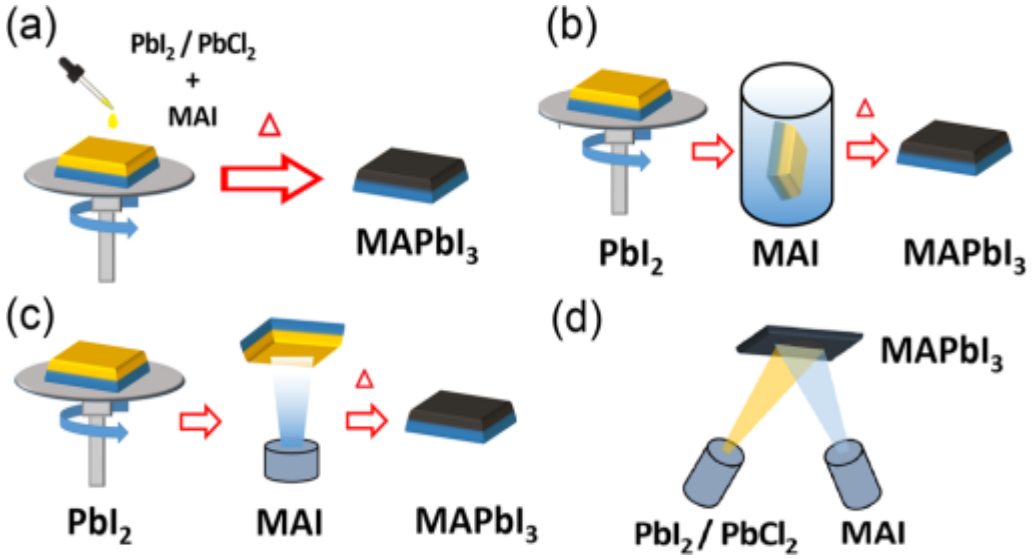

Figure 2.10: Schematic representation of perovskite solar cell fabrication methods. (a) One-step method, (b) Two-step method, (c) Vapour assisted solution method and (d) Thermal vapour deposition method. Precursor concentrations, dipping coating time, spin coating time, and spinning rates are perovskite film quality and morphology controlling parameters during fabrication [38].

In one step deposition method, the solution ionic strength and post-annealing improve the perovskite crystal formation [58]. However, drawbacks such as lack of control over film uniformity and morphology are observed. Chen [2015] *fabricated* a p-i-n perovskite device with 210nm perovskite thickness by spin coating and acquired PCE= 11.99%, V_{oc} = 0.81V and J_{sc}= 21.9mAcm^{-2}. **Figure 2.11 (a)** shows XRD peaks at diffraction angles 28.39° and 31.86° indicating the perovskite crystal formation and further suggesting that the depositing solvent did not destroy the perovskite crystal structure [59]. Despite observed good device efficiency of 3.8 to 11.99% **Figure 2.11 (b)** shows perovskite film FESEM surface image with the presence of pinholes due to the incomplete crystallization and distribution of non-uniform grains along the film morphology.

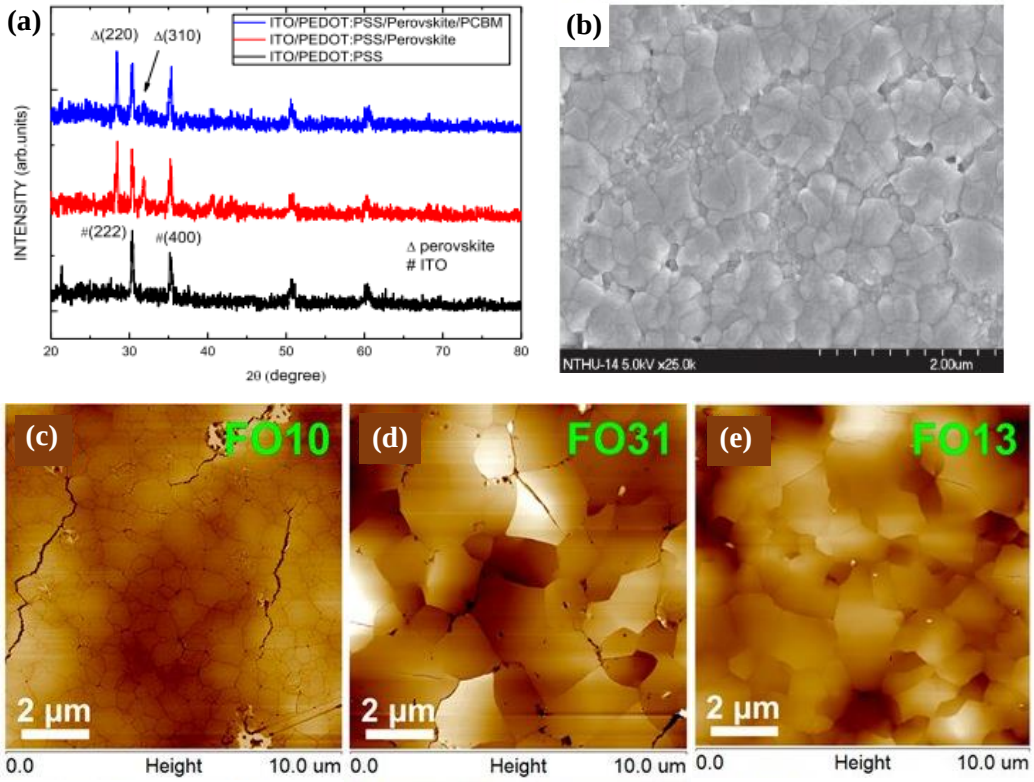

Figure 2.11: (a) X-ray diffraction patterns, (b) SEM micrograph, (c)-(d) AFM images [37,59].

Zhang [2019] worked on improving the perovskite surface morphology by using binary solvent engineering systems during the perovskite film deposition. The technique offers control over the perovskite crystal formation allowing complete and well oriented homogeneous perovskite films [37]. This unique control over morphologies is achieved by a mixture of solvents such as the above mentioned DMF, DMSO, and GBL [37,60]. **Figure 2.11 (c)-(e)** shows AFM images at different DMF/DMSO solvent ratios of 1:0, 3:1, and 1:3 denoted as FO10, FO31 and FO13 respectively. At the presence of only the DMF solvent in **Figure 2.11 (c)** the AFM image reveals similar results reported in **Figure 2.11 (b)**. The addition of a second solvent at a solvent ratio of 3:1 and 1:3 assists the film to eliminate the observed morphology cracks, pinholes and incomplete crystallization defects. The volatile DMF solvent activates a homogeneous perovskite crystal nucleation and the presence of DMSO helps with crystal growth in an ordered orientation. Hence the observed large, smooth and closely packed perovskite grain morphologies in **Figure 2.11 (e)**. In a similar study using a solvent mixture of GBL/DMSO at a ratio of 7:3, Jeon [2014] acquired an increased PCE of ~16.2% with no hysteresis in forward and reverse bias I-V measurements [60].

2.7.2 Two-step method

The two-step fabrication or sequential fabrication method involves the spin coating of individual organic (MAI/FAI) and inorganic (PbX_2/SnX_2) precursor solutions. This method offers the advantage to control the surface morphology and film quality by optimizing precursor concentrations, dip coating or spin coating time, and spinning rates during the deposition of either organic or inorganic halide precursors. In the two-step method, the first step of deposition is spin coating of the inorganic halide (PbX_2) on a substrate then the second step of deposition follows by either (i) dipping PbX_2 coated substrate into the MAI solution or (ii) spin coating the MAI solution over the PbX_2 substrate (see **Figure 2.10 (b)**) [61]. Burschka [2013] used the two-step method to fabricate a PSC with PCE= 15.0% the study confirms a better control of device morphology by the X-ray diffraction (XRD) patterns and SEM cross-sectional micrographs of the device [62]. The reported cross-sectional SEM images show firstly, the introduction of PbI_2 into the nanoporous TiO_2 film. This is confirmed by the formation of a single layer of TiO_2/PbI_2 with complete PbI_2 crystal absorption indicating successful PbI_2 deposition onto TiO_2 nanopores. The XRD pattern shows a characteristic perovskite peak at 14° diffraction angle confirming the formation of the perovskite absorber layer upon second step deposition of MAI by (i) dip coating the TiO_2/PbI_2 bearing substrate.

The presence of PbI_2 residuals reduces the solar cell light-harvesting ability and charge carrier transport hence reducing the overall PSC performance [63,64]. Similar to the one-step deposition method above, solvent engineering and the use of additives may be applied to overcome this fabrication drawback in the two-step method. Li [2015] reported a solvent mixture based on DMF and DMSO for PbI_2 powder dissolution. In which the DMSO in the solvent mixture prevents early PbI_2 crystallization and further acting as an intermolecular intermediate exchanging agent with MAI during $MAPbI_3$ film formation. Low temperature and low spinning time of MAI during the second step of deposition results in perovskite crystal formation only at the PbI_2 surface which blocks further MAI infiltration into PbI_2 lattice. Such mass infiltration forms a rough surface with the presence of voids and pinholes [65,66].

2.7.3 Vapour assisted solution method

Vapour assisted solution deposition method is considered as a modification of the two-step method which improves the infiltration of the precursor solutions. The only difference between vapour assisted solution and two-step method is that during the second step of deposition a vapour phase of either MAI/FAI is reacted with the PbI_2 film (see **Figure 2.10 (c)**) [61,67]. Chen [2015] investigated the performance of PSCs prepared by two-step and vapour assisted solution methods and highlighted that perovskites fabricated with different techniques result in different properties. Flat films fabricated through vapour assisted deposition show

high surface coverage and pore filling of the mesoporous TiO_2. The device performance records a high V_{oc} of 0.96V and an IPCE value of 81% over a wide wavelength range of 400-740nm. Photoluminescence (PL) spectra showed an intense peak in the two-step fabricated film confirming defect densities caused by poor surface coverage [68]. Vapour assisted solution method is promising as PSC efficiencies continue to increase as different approaches are designed. The disadvantage of vapour assisted method is hours of device fabrication [69,70].

2.7.4 Thermal vapour deposition method

The thermal vapour deposition method involves simultaneous deposition of the organic (e.g., MAI or FAI) and inorganic (e.g., PbI_2/$PbCl_2$) halides in the vapour phase on a rotating substrate (see **Figure 2.10 (d)**). This method offers a uniform surface morphology due to ease of control over precursor depositing parameters and the speed of rotating substrate [29]. Liu [2013] reported a planar mixed halide PSC recording efficiencies of up to 15.4%. The perovskite $MAPbI_{3-x}Cl_x$ thin films were prepared by vapour deposition of MAI and $PbCl_2$ precursor powder materials at a 4:1 deposition ratio [71]. In an attempt to produce a large surface area PSC device, Liang [2018] reported a large-scale PSC with a surface area of $100cm^2$ (see **Figure 2.12 (a)**) [72]. The device showed a PCE equal to 7.73%. This study serves as a benchmark for the fabrication of commercial PSC through thermal vapour deposition. The device maintained a uniform composition throughout the film with no presence of impurities and subsequently high solar cell performance. **Figure 2.12 (c)** depicts consistent XRD patterns at different regions of the solar cell marked A, B, C, E and D as shown in **Figure 2.12 (b)**.

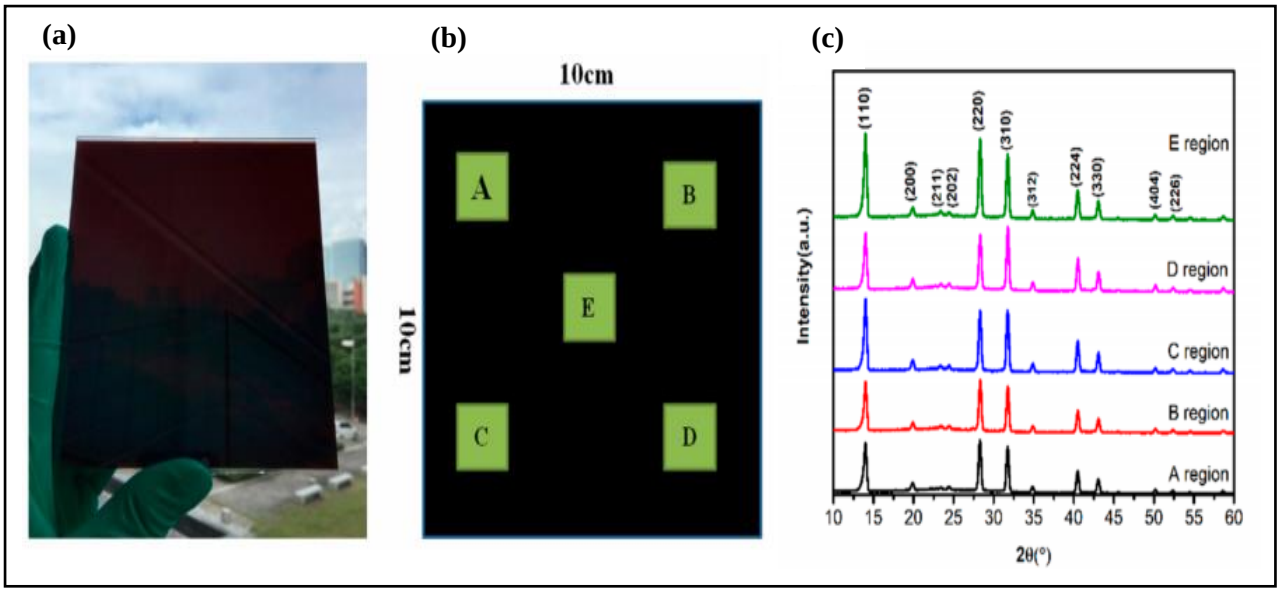

Figure 2.12: Low-(a) and (b) Low-resolution images (a) and (b)of the 100cm2 PSC prepared by the thermal vapour-deposited method. (c) XRD patterns at the marked regions A, B, C, D, and E [72].

2.8 Device challenges

2.8.1 Perovskite solar cell device stability

The development of the PSCs in the past decade has shown massive improvement in efficiency over a short period in comparison with other existing solar cells. PSCs have already surpassed the performance of commercially available silicon-based PVs making them the future in solar energy. However, the device lifespan is below the required 25 years for a normal PV cell, ranging from days to months. The degradation of PSCs performance suggests that the device instability stands in the way of commercialization [73]. Therefore, it is necessary to understand PSC degradation mechanics to improve on the device flaws. In the characterization of perovskite cell stability, the device is subjected to harsh environments in order to obtain superior performance at normal conditions. The degradation response results from failure of device components caused by external factors (moisture, oxygen, temperature, and UV radiation), internal factors (crystal structure, ion migration, interfacial contact), the constituting materials, device architecture, and fabrication process. Therefore, it is important to note that PSC stability is affected by a handful of factors. Suggesting that it is necessary to further study PSCs thoroughly, develop standard procedures and protocols towards building a fully functional and stable device.

2.8.2 Stability in the perovskite crystal structure (ABX_3)

The stability of the perovskite crystal structure is determined using the Goldschmidt tolerance factor (t), shown by equation (1) above. The cubic (α) phase is the most stable crystal structure followed by the tetragonal (β) phase and the least stable crystal structure is the orthorhombic (γ) phase. In any crystal structure, the tolerance factor depends on the ABX_3 constituting organic (e.g., $MA^{+}= r_A$), inorganic (e.g., $Pb^{2+}= r_B$) and halogen (e.g., $I^{-}= r_0$) ionic radius [74]. Further research has relieved that the crystal structure stability is also affected by changes in temperature and pressure. In the study to investigate the effect of temperature on perovskite crystal structure Cojocaru [2015] reported a $MAPbI_3$ phase transition from tetragonal to cubic at temperatures greater than 55°C. In **Figure 2.13 (a)** the XRD results confirm a tetragonal phase at perovskite characteristic diffraction angles of 14.1°, 28.5°, and 43.3° associated with the (110), (220) and (330) planes, respectively [75]. An increase in sample temperature affects the crystal shape as illustrated in **Figure 2.13 (b)-(d)**, the diffraction peaks shift to lower diffraction angles as the temperature is increased. The observed shift in the XRD peaks suggests the rearrangement of the crystal lattice. **Figure 2.13 (b)-(d)** shows the phase transition from a tetragonal phase to a lower diffraction angle cubic phase for samples heated in a temperature range of -95 to 100°C. In another study, Gratzel [1998] reported the thermal stability of $FAPbI_3$. The $FAPbI_3$ has higher thermal stability than $MAPbI_3$ due to its tetragonal-cubic phase transition occurring at a high temperature of 150°C [76]. Therefore, in conclusion, a stable perovskite crystal structure is found at high temperatures and also depends on the perovskite material in question.

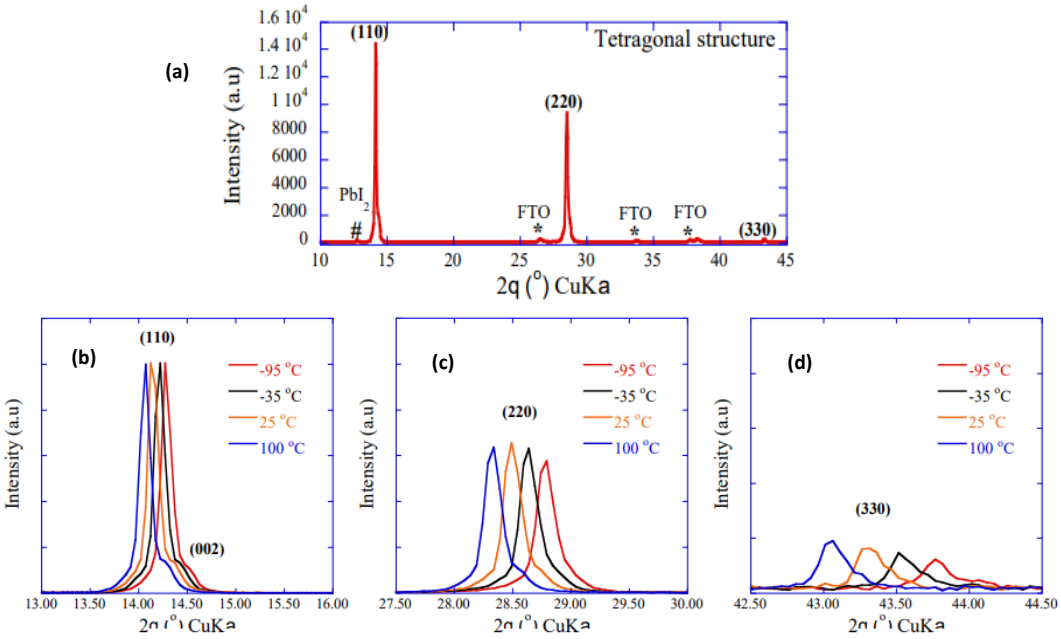

Figure 2.13: X-ray diffraction pattern of a perovskite sample (a) heated at 25◦C, (b-d) magnified perovskite CH3NH3PbI3 characteristic peaks heating at temperature range -95◦C to 100◦C [75].

The perovskite crystal structure response mechanism to pressure remains a mystery, as there is an unusual sequence of phase transition with an increase in pressure. For example, tetragonal-cubic-orthorhombic, orthorhombic-tetragonal-cubic, and vice versa phase transitions are observed [77,78]. Jaffe [2016] conducted a study to understand $MAPbX_3$ (X= Br and I) perovskite crystal structure response to compression. Single crystal and powder X-ray Diffraction (SCXRD and PXRD) techniques were used to characterize material crystal structure at ambient pressure and during high-pressure conditions [79]. The applied pressure had a significant effect on Pb-X (X= Br and I) bond lengths, volume and α-β phase transition. **Figure 2.14 (a)** and **(b)** shows $MAPbX_3$ SCXRD crystal structure model at ambient and high pressure. **Figure 2.14 (c)** and **(d)** shows $MAPbX_3$ PXRD diffraction patterns under a continuous increase in pressure (compression). At ambient pressure, Pb-X-Pb bond angles are at 180° as shown in **Figure 2.14 (a)** and **(b)**, compression results in the Pb-X-Pb bond angle contraction to angles < 180°, reduction in Pb-X bong length, and subsequently the occurrence of α-β phase transitions at pressures greater than 1.7 and 0.7 GPa for $MAPbBr_3$ and $MAPbI_3$ perovskite crystal structures, respectively. Further compression in the β phase results in further bond length and volume reductions. Strong intermolecular interactions develop due to the tight conformation in the ABX_3 unit cell. The XRD patterns in **Figure 2.14 (c)** and **(d)** shows changes in $MAPbBr_3$ and $MAPbI_3$ crystal structure as pressure is continuously increased up to a maximum pressure of 9 GPa. In both perovskite materials $MAPbX_3$ (X= Br and I) a normal perovskite behaviour is expected at low pressures as indicated by arrow 1. An increase in pressure destroys the normal perovskite crystal structure behaviour hence the disappearance of perovskite characteristic peaks indicated by arrow 2. Arrow 3 shows that the perovskite materials can restore their initial configuration or normal behaviour upon decompression. Therefore, in conclusion, the perovskite crystal structure does respond to pressure. Subjecting the material to high pressures suppresses or reduces the perovskite structural features. Therefore, a stable perovskite crystal structure (α phase) is obtained at relatively low pressures.

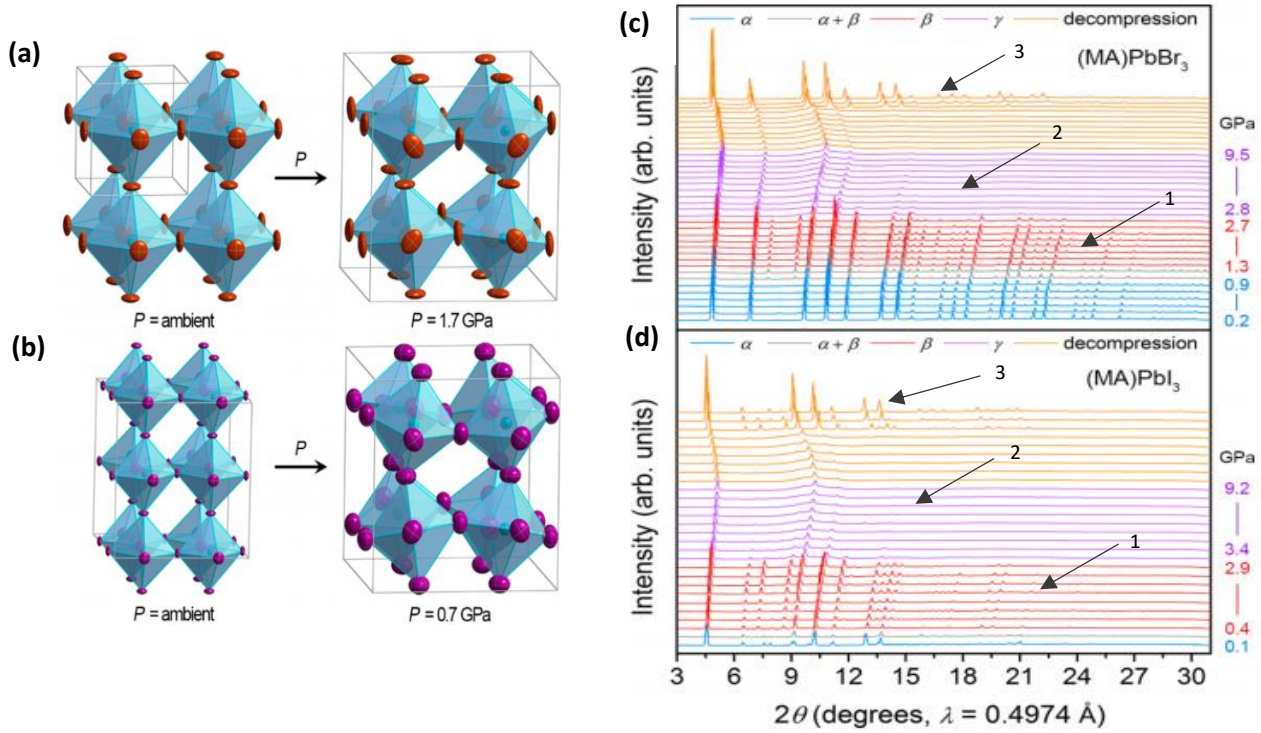

Figure 2.14: SCXRD schematic representation of crystal structure for (a) MAPbBr3 and (b) MAPbI3 at ambient and high pressures of 1.7 and 0.7GPa. Changes PXRD patterns for (c) MAPbIBr3 and (d) MAPbI3 in response to the applied pressure [79].

2.8.3 Environmental stability.

The perovskite ABX_3 materials are chemically active in environmental conditions. A series of chemical reactions occur which slowly break down the ABX_3 material into its constituents and additional by-products. Installation of PSCs exposes the device to environmental contaminants. Oxygen, moisture and UV radiation constantly wear off the PV perovskite active layer. The chemical reactions below suggest possible perovskite degradation. Moisture breaks down the perovskite layer by dissolving the organic cation (MA^+) to yield PbI_2 and HI. This degradation mechanism is an irreversible process as the presence of oxygen and UV radiation further breaks down the hydroiodic acid (HI) producing water (H_2O), hydrogen (H_2) and iodine (I_2) gas as by-products (see chemical reactions (2)-(5)) [80]. The chemical reactions (2)-(5) and (6)-(9) are proposed degradation reactions initiated by the presence of sunlight and moisture. In a study to investigate the degradation of $MAPbI_3$ material exposed to a humid environment Shirayama [2016] reported a rapid decomposition in the perovskite material at low relative humidity of 40% caused by either or both of the following: formation of PbI_2 phase from the desorption of the volatile organic MAI cation or formation of perovskite hydrate phase resulting from the interaction of H_2O molecules and the absorber N-H bond [81]. In a similar study, Yang [2015] suggested that proper selection of a hydrophobic HTM stabilize

the perovskite layer deterioration, however, the effort only shifts the perovskite lifespan to a few more hours before it begins degrading [82].

$$CH_3NH_3PbI_3(s) \leftrightarrow PbI_2(s) + CH_3NH_3I(aq) \quad (2)$$

$$CH_3NH_3I(aq) \leftrightarrow CH_3NH_2(aq) + HI(aq) \quad (3)$$

$$4HI(aq) + O_2 \leftrightarrow 2I_2 + 2H_2O(l) \quad (4)$$

$$2HI(aq) \leftrightarrow H_2(g) + I_2(s) \quad (5)$$

$$CH_3NH_3PbI_3(s) \leftrightarrow PbI_2(s) + CH_3NH_2 \uparrow + HI \uparrow \quad (6)$$

$$2I^- \leftrightarrow I_2 + 2e^- \quad (7)$$

$$3CH_3NH_3^+ \leftrightarrow 3CH_3NH_2 \uparrow + 3H^+ \quad (8)$$

$$I^- + I_2 + 3H^+ + 2e^- \leftrightarrow 3HI \uparrow \quad (9)$$

In **Figure 2.15 (a)-(c)** SEM surface images reveal perovskite film morphology exposed to 40% relative humidity (RH) at various exposure times. **Figure 2.15 (a)** reports a smooth surface at 20 min exposure with a high level of surface coverage, **Figure 2.15 (b)** reports SEM surface morphology at 24 hours of exposure showing the formation of evenly distributed holes reducing surface homogeneity (indicated by arrow 1). The generation of holes results from the PbI_2 phase structure coalescence as the MAI organic cation dissolves in moisture, in **Figure 2.15 (c)** the SEM image at 48 hours of exposure shows well defined rod-like PbI_2 structures (indicated arrow 2) and the extend of hole formation in film [82]. Many attempts focus on eliminating the effect of moisture on PSCs by encapsulation of the device, Many attempts focus on eliminating the effect of moisture on PSCs by designing new architectures, encapsulating the device using polymers, proposing new ETM and HTM materials and among others modifying the ABX_3 materials.

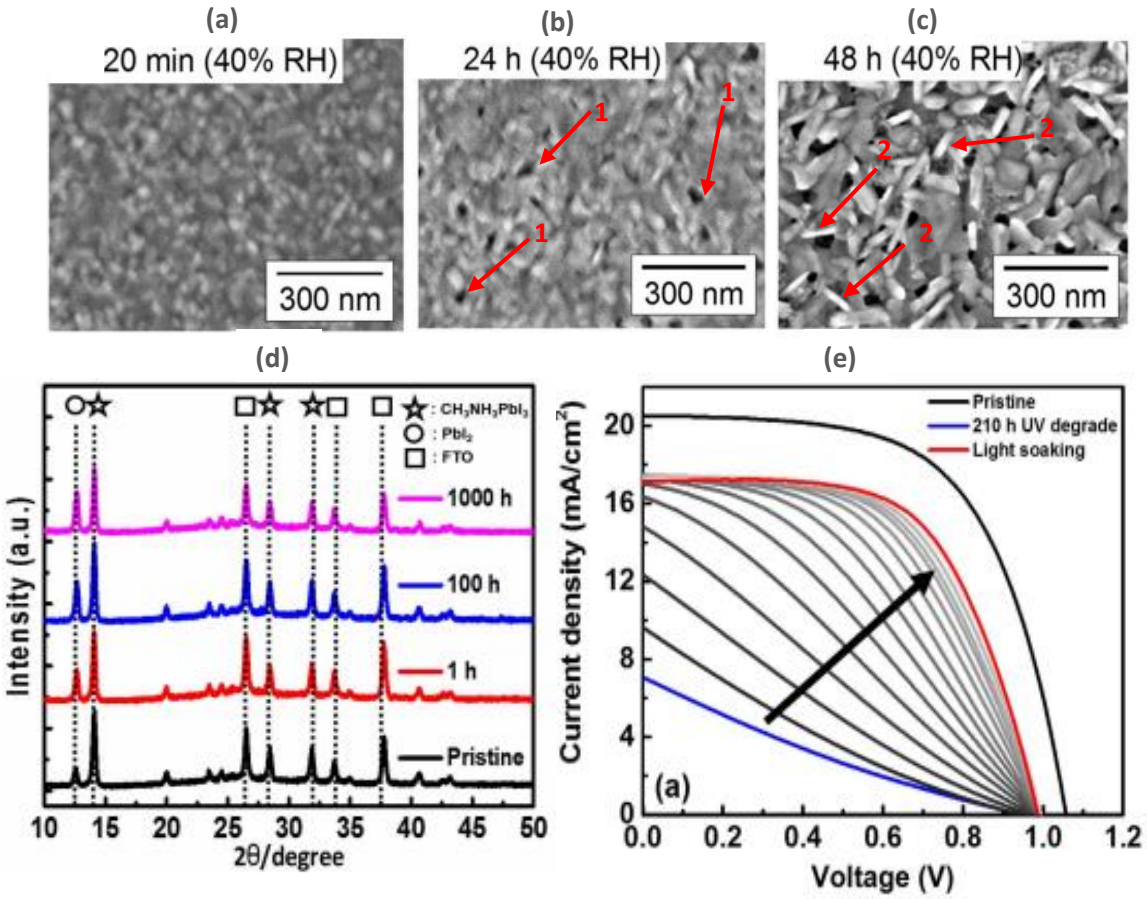

Figure 2.15: Characterization of perovskite device degradation upon exposure to 40% relative humidity (RH) and UV light. SEM surface images of the device exposed to 40% RH for **(a)** t= 20 min, **(b)** 24 hr,and **(c)** 48 hrs. **(d)** XRD and **(e)** I-V curve perovskite response in UV light degradation [81,83].

In order to eliminate the effect of moisture and investigate the effect on UV radiation alone, Lee [2016] studied the degradation of PSCs in an inert atmosphere (glove box) by exposing the PSC devices to UV light. The effect of UV exposure on the device was characterized through XRD and I-V techniques as shown in **Figure 2.15 (d)** and **(e)**, respectively. From both characterizations, it is observed that UV degradation is slightly reversible via light soaking the devices. From **Figure 2.15 (d)** the XRD patterns show the development of PbI_2 peak at 12.6° diffraction angle accompanied by a fading perovskite characteristic peak at 14.1° with an increase in UV exposure time. These results are comparable to that of perovskite moisture decomposition. . In **Figure 2.15 (e)** the I-V curves show that the occurrence of degradation constantly weakens the device performance after 210 hours of exposure to UV radiation (blue curve). However light soaking of the device works against the degradation process partially restoring the device performance.

2.9 Other challenges.

2.9.1 Toxicity.

The toxicity in perovskite devices comes from the presence of the toxic lead (Pd) element. This raises environmental concerns for the upcoming device scaleup for commercialization. The lack of device stability provides a possible way for toxic lead (Pb) leakage from the installed solar panels to the environment [29] Due to the high demand for energy globally, a rising number of studies encourage the use of Pb containing devices as pollution from these devices will be insignificantly small in comparison with other lead polluting sources around the world [84]. However, there is several promising alternatives for lead replacement with environmentally friendly elements. Noel [2015] worked on replacing the Pb component and devised a tin (Sn) based perovskite device ($MASnX_3$) with a promising PCE of 6%. Later studies reported that Sn-based perovskites suffer from instability due to the easy 2+ oxidation of Sn element in moisture to 4+ states. Hoshi [2016] proposed the use of additives for stability. This effort showed significant improvement however the efficiencies achieved were not certifying [85,86]. To reinstate the purpose of perovskites which is high efficiency and stability, a hybrid of Sn-Pb perovskite film was proposed and achieved efficiencies of up to 15.2% [87].

2.10 Future research

Future work will focus on revising and designing new methods to improve the PSC performance. We will in particular investigate the effect of annealing and doping of trivalent and pentavalent dopants on synthesized nanoparticles and nanotubes metal oxides such as titanium and zinc oxide (TiO_2 and ZnO) for enhanced electron extraction in PSCs. For environmental concerns, further research work will focus more on replacing the highly toxic lead (Pb) element with Tin (Sn) due to their similar chemical properties. The widely used hole transporting material to date is the Spiro-MeOTAD, to fabricate cost-effective devices cheaper p-type hole-transporting materials such as Cu_2O and NiO will be explored. As a reference or benchmark in our research group, a well thought fabrication method will be proposed from where we can build towards achieving a fully functional highly efficient and stable perovskite device. Aspects to be evaluated in the fabrication method include the effect of precursor concentration, annealing temperatures, annealing time, synthesis period, annealing at various gaseous environments, and exploration of different device architectures.

References

[1] H.-S. Kim, N.-G. Park, Parameters Affecting I−V Hysteresis of CH 3 NH 3 PbI 3 Perovskite Solar Cells: Effects of Perovskite Crystal Size and Mesoporous TiO 2 Layer, J. Phys. Chem. Lett. 52 (2014) 53. https://doi.org/10.1021/jz501392m.

[2] A. Kojima, K. Teshima, Y. Shirai, T. Miyasaka, Organometal Halide Perovskites as Visible-Light Sensitizers for Photovoltaic Cells, 10 (2021) 43. https://doi.org/10.1021/ja809598r.

[3] H.-S. Kim, S.H. Im, N.-G. Park, Organolead Halide Perovskite: New Horizons in Solar Cell Research, (2014). https://doi.org/10.1021/jp409025w.

[4] M.M. Lee, J. Teuscher, T. Miyasaka, T.N. Murakami, H.J. Snaith, Efficient hybrid solar cells based on meso-superstructured organometal halide perovskites, Science (80-.). 338 (2012) 643–647. https://doi.org/10.1126/science.1228604.

[5] A. Roghabadi, F, M. Alidaei, S.. Mousavi, T. Ashjari, A.. Ehrani, V. Ahmadi, S.. Sadrameli, Best Research-Cell Efficiency Chart, (2021). https://www.nrel.gov/pv/cell-efficiency.html.

[6] B.G. Pollet, I. Staffell, K.A. Adamson, Current energy landscape in the Republic of South Africa, Int. J. Hydrogen Energy. 40 (2015) 16685–16701. https://doi.org/10.1016/j.ijhydene.2015.09.141.

[7] I. Dincer, Environmental impacts of energy, Energy Policy. 27 (1999) 845–854. https://doi.org/https://doi.org/10.1016/S0301-4215(99)00068-3.

[8] J.A. Turner, A realizable renewable energy future, Science (80-.). 285 (1999) 687–689. https://doi.org/10.1126/science.285.5428.687.

[9] L. Meng, J. You, T.-F. Guo, Y. Yang, Recent Advances in the Inverted Planar Structure of Perovskite Solar Cells, (2015). https://doi.org/10.1021/acs.accounts.5b00404.

[10] M. Abdi-Jalebi, M.I. Dar, A. Sadhanala, S.P. Senanayak, M. Grätzel, R.H. Friend, H. Monovalent Cation Doping of CH 3 NH 3 PbI 3 for Efficient Perovskite Solar Cells, J. Vis. Exp. (2017) 55307. https://doi.org/10.3791/55307.

[11] C.H. Ng, H.N. Lim, S. Hayase, Z. Zainal, N.M. Huang, Photovoltaic performances of mono- and mixed-halide structures for perovskite solar cell: A review, Renew. Sustain. Energy Rev. 90 (2018) 248–274. https://doi.org/10.1016/j.rser.2018.03.030.

[12] Y. Liu, J. Wang, Co-sensitization of TiO2 by PbS quantum dots and dye N719 in dye-sensitized solar cells, Thin Solid Films. 518 (2010) e54–e56. https://doi.org/10.1016/j.tsf.2010.03.126.

[13] J. Chen, D.W. Zhao, J.L. Song, X.W. Sun, W.Q. Deng, X.W. Liu, W. Lei, Directly assembled CdSe quantum dots on TiO2 in aqueous solution by adjusting pH value for quantum dot sensitized solar cells, Electrochem. Commun. 11 (2009) 2265–2267. https://doi.org/10.1016/J.ELECOM.2009.10.003.

[14] Q. Zhang, Y. Zhang, S. Huang, X. Huang, Y. Luo, Q. Meng, D. Li, Application of carbon counterelectrode on CdS quantum dot-sensitized solar cells (QDSSCs), Electrochem. Commun. 12 (2010) 327–330. https://doi.org/10.1016/J.ELECOM.2009.12.032.

[15] J.-H. Im, C.-R. Lee, J.-W. Lee, S.-W. Park, N.-G. Park, 6.5% efficient perovskite quantum-dot-sensitized solar cell †, (n.d.). https://doi.org/10.1039/c1nr10867k.

[16] A. Fujishima, X.T. Zhang, Solid-State Dye-Sensitized Solar Cells, Nanostructured Mater. Sol. Energy Convers. (2006) 255–273. https://doi.org/10.1016/B978-044452844-5/50010-X.

[17] H.S. Kim, C.R. Lee, J.H. Im, K.B. Lee, T. Moehl, A. Marchioro, S.J. Moon, R. Humphry-Baker, J.H. Yum, J.E. Moser, M. Grätzel, N.G. Park, Lead iodide perovskite

sensitized all-solid-state submicron thin film mesoscopic solar cell with efficiency exceeding 9%, Sci. Rep. 2 (2012). https://doi.org/10.1038/srep00591.
[18] H. Zhang, Y. Lv, J. Wang, H. Ma, Z. Sun, W. Huang, Influence of Cl Incorporation in Perovskite Precursor on the Crystal Growth and Storage Stability of Perovskite Solar Cells, (2019). https://doi.org/10.1021/acsami.8b19390.
[19] A.K. Jena, A. Kulkarni, T. Miyasaka, Halide Perovskite Photovoltaics: Background, Status, and Future Prospects, Chem. Rev. 119 (2019) 3036–3103. https://doi.org/10.1021/acs.chemrev.8b00539.
[20] J.M. Ball, M.M. Lee, A. Hey, H.J. Snaith, Low-temperature processed meso-superstructured to thin-film perovskite solar cells †, (n.d.). https://doi.org/10.1039/c3ee40810h.
[21] P. Docampo, F.C. Hanusch, S.D. Stranks, M. Döblinger, J.M. Feckl, M. Ehrensperger, N.K. Minar, M.B. Johnston, H.J. Snaith, T. Bein, Solution Deposition-Conversion for Planar Heterojunction Mixed Halide Perovskite Solar Cells, Adv. Energy Mater. 4 (2014) 1400355. https://doi.org/https://doi.org/10.1002/aenm.201400355.
[22] M. Imran Ahmed, A. Habib, S. Saad Javaid, Perovskite Solar Cells: Potentials, Challenges, and Opportunities, (2015). https://doi.org/10.1155/2015/592308.
[23] O. Grånäs, D. Vinichenko, E. Kaxiras, Establishing the limits of efficiency of perovskite solar cells from first principles modeling OPEN, Nat. Publ. Gr. (2016). https://doi.org/10.1038/srep36108.
[24] J.P. Correa-Baena, A. Abate, M. Saliba, W. Tress, T. Jesper Jacobsson, M. Grätzel, A. Hagfeldt, The rapid evolution of highly efficient perovskite solar cells, Energy Environ. Sci. 10 (2017). https://doi.org/10.1039/c6ee03397k.
[25] F.A. Roghabadi, M. Alidaei, S.M. Mousavi, T. Ashjari, A.S. Tehrani, V. Ahmadi, S.M. Sadrameli, Stability progress of perovskite solar cells dependent on the crystalline structure: From 3D ABX3 to 2D Ruddlesden-Popper perovskite absorbers, J. Mater. Chem. A. 7 (2019) 5898–5933. https://doi.org/10.1039/c8ta10444a.
[26] Z. Shi, A.H. Jayatissa, Perovskites-Based Solar Cells: A Review of Recent Progress, Materials and Processing Methods, Mater. . 11 (2018). https://doi.org/10.3390/ma11050729.
[27] B. Li, Y. Li, C. Zheng, D. Gao, W. Huang, Advancements in the stability of perovskite solar cells: Degradation mechanisms and improvement approaches, RSC Adv. 6 (2016) 38079–38091. https://doi.org/10.1039/c5ra27424a.
[28] G.W.P. Adhyaksa, L.W. Veldhuizen, Y. Kuang, S. Brittman, R.E.I. Schropp, E.C. Garnett, Carrier Diffusion Lengths in Hybrid Perovskites: Processing, Composition, Aging, and Surface Passivation Effects, Chem. Mater. 28 (2016). https://doi.org/10.1021/acs.chemmater.6b00466.
[29] Y. Chen, L. Zhang, Y. Zhang, H. Gao, H. Yan, Large-area perovskite solar cells-a review of recent progress and issues, RSC Adv. 8 (2018). https://doi.org/10.1039/c8ra00384j.
[30] M.S.G. Hamed, G.T. Mola, Mixed Halide Perovskite Solar Cells: Progress and Challenges, Crit. Rev. Solid State Mater. Sci. 45 (2020). https://doi.org/10.1080/10408436.2018.1549976.
[31] K. Shen, J. Hu, Z. Liang, J. Hu, H. Sun, Z. Jiang, F. Song, Emerging characterizing techniques in the fine structure observation of metal halide perovskite crystal, Crystals. 8 (2018). https://doi.org/10.3390/cryst8060232.
[32] W.F. Forrester, R.M. Hinde, Crystal structure of barium titanate [15], Nature. 156 (1945). https://doi.org/10.1038/156177b0.
[33] J. Chen, X. Cai, D. Yang, D. Song, J. Wang, J. Jiang, A. Ma, S. Lv, M.Z. Hu, C. Ni, Recent progress in stabilizing hybrid perovskites for solar cell applications, J. Power

Sources. 355 (2017). https://doi.org/10.1016/j.jpowsour.2017.04.025.
[34] W.J. Yin, T. Shi, Y. Yan, Unusual defect physics in CH3NH3PbI3 perovskite solar cell absorber, Appl. Phys. Lett. 104 (2014). https://doi.org/10.1063/1.4864778.
[35] Y. Zhou, F. Huang, Y.B. Cheng, A. Gray-Weale, Photovoltaic performance and the energy landscape of CH3NH3PbI3, Phys. Chem. Chem. Phys. 17 (2015). https://doi.org/10.1039/c5cp03352g.
[36] Y. Wang, T. Gould, J.F. Dobson, H. Zhang, H. Yang, X. Yao, H. Zhao, Density functional theory analysis of structural and electronic properties of orthorhombic perovskite CH3NH3PbI3, Phys. Chem. Chem. Phys. 16 (2014). https://doi.org/10.1039/c3cp54479f.
[37] J. Zhang, L. Zhang, X. Li, X. Zhu, J. Yu, K. Fan, Binary Solvent Engineering for High-Performance Two-Dimensional Perovskite Solar Cells, ACS Sustain. Chem. Eng. 7 (2019). https://doi.org/10.1021/acssuschemeng.8b05734.
[38] Z. Song, S.C. Watthage, A.B. Phillips, M.J. Heben, Pathways toward high-performance perovskite solar cells: review of recent advances in organo-metal halide perovskites for photovoltaic applications, J. Photonics Energy. 6 (2016). https://doi.org/10.1117/1.jpe.6.022001.
[39] G.E. Eperon, V.M. Burlakov, P. Docampo, A. Goriely, H.J. Snaith, Morphological control for high performance, solution-processed planar heterojunction perovskite solar cells, Adv. Funct. Mater. 24 (2014). https://doi.org/10.1002/adfm.201302090.
[40] S. Yang, Q. Han, L. Wang, Y. Zhou, F. Yu, C. Li, X. Cai, L. Gao, C. Zhang, T. Ma, Over 23% power conversion efficiency of planar perovskite solar cells via bulk heterojunction design, Chem. Eng. J. 426 (2021). https://doi.org/10.1016/j.cej.2021.131838.
[41] J.H. Heo, M.H. Lee, M.H. Jang, S.H. Im, Highly efficient CH3NH3PbI3−xClx mixed halide perovskite solar cells prepared by re-dissolution and crystal grain growth via spray coating, J. Mater. Chem. A. 4 (2016) 17636–17642. https://doi.org/10.1039/C6TA06718B.
[42] T. Matsui, J.Y. Seo, M. Saliba, S.M. Zakeeruddin, M. Grätzel, Room-Temperature Formation of Highly Crystalline Multication Perovskites for Efficient, Low-Cost Solar Cells, Adv. Mater. 29 (2017). https://doi.org/10.1002/adma.201606258.
[43] H. Wang, Z. Yu, X. Jiang, J. Li, B. Cai, X. Yang, L. Sun, Efficient and Stable Inverted Planar Perovskite Solar Cells Employing CuI as Hole-Transporting Layer Prepared by Solid–Gas Transformation, Energy Technol. 5 (2017). https://doi.org/10.1002/ente.201700422.
[44] J. Liu, Y. Wu, C. Qin, X. Yang, T. Yasuda, A. Islam, K. Zhang, W. Peng, W. Chen, L. Han, A dopant-free hole-transporting material for efficient and stable perovskite solar cells, Energy Environ. Sci. 7 (2014). https://doi.org/10.1039/c4ee01589d.
[45] B. Suarez, V. Gonzalez-Pedro, T.S. Ripolles, R.S. Sanchez, L. Otero, I. Mora-Sero, Recombination study of combined halides (Cl, Br, I) perovskite solar cells, J. Phys. Chem. Lett. 5 (2014). https://doi.org/10.1021/jz5006797.
[46] T. Singh, T. Miyasaka, Stabilizing the Efficiency Beyond 20% with a Mixed Cation Perovskite Solar Cell Fabricated in Ambient Air under Controlled Humidity, Adv. Energy Mater. 8 (2018). https://doi.org/10.1002/aenm.201700677.
[47] M. Saliba, T. Matsui, K. Domanski, J.Y. Seo, A. Ummadisingu, S.M. Zakeeruddin, J.P. Correa-Baena, W.R. Tress, A. Abate, A. Hagfeldt, M. Grätzel, Incorporation of rubidium cations into perovskite solar cells improves photovoltaic performance, Science (80-.). 354 (2016). https://doi.org/10.1126/science.aah5557.
[48] B.J. Kim, D.H. Kim, Y.Y. Lee, H.W. Shin, G.S. Han, J.S. Hong, K. Mahmood, T.K. Ahn, Y.C. Joo, K.S. Hong, N.G. Park, S. Lee, H.S. Jung, Highly efficient and bending

durable perovskite solar cells: Toward a wearable power source, Energy Environ. Sci. 8 (2015). https://doi.org/10.1039/c4ee02441a.
[49] M.M. Tavakoli, Q. Lin, S.F. Leung, G.C. Lui, H. Lu, L. Li, B. Xiang, Z. Fan, Efficient, flexible and mechanically robust perovskite solar cells on inverted nanocone plastic substrates, Nanoscale. 8 (2016). https://doi.org/10.1039/c5nr08836d.
[50] Y. Bai, H. Yu, Z. Zhu, K. Jiang, T. Zhang, N. Zhao, S. Yang, H. Yan, High performance inverted structure perovskite solar cells based on a PCBM: Polystyrene blend electron transport layer, J. Mater. Chem. A. 3 (2015). https://doi.org/10.1039/c4ta05309e.
[51] A.T. Barrows, A.J. Pearson, C.K. Kwak, A.D.F. Dunbar, A.R. Buckley, D.G. Lidzey, Efficient planar heterojunction mixed-halide perovskite solar cells deposited via spray-deposition, Energy Environ. Sci. 7 (2014). https://doi.org/10.1039/c4ee01546k.
[52] M. Saliba, J.P. Correa-Baena, C.M. Wolff, M. Stolterfoht, N. Phung, S. Albrecht, D. Neher, A. Abate, How to Make over 20% Efficient Perovskite Solar Cells in Regular (n-i-p) and Inverted (p-i-n) Architectures, Chem. Mater. 30 (2018). https://doi.org/10.1021/acs.chemmater.8b00136.
[53] A. Dubey, N. Adhikari, S. Mabrouk, F. Wu, K. Chen, S. Yang, Q. Qiao, A strategic review on processing routes towards highly efficient perovskite solar cells, J. Mater. Chem. A. 6 (2018). https://doi.org/10.1039/c7ta08277k.
[54] F. Xu, T. Zhang, G. Li, Y. Zhao, Mixed cation hybrid lead halide perovskites with enhanced performance and stability, J. Mater. Chem. A. 5 (2017). https://doi.org/10.1039/c7ta00042a.
[55] M. Saliba, T. Matsui, J.Y. Seo, K. Domanski, J.P. Correa-Baena, M.K. Nazeeruddin, S.M. Zakeeruddin, W. Tress, A. Abate, A. Hagfeldt, M. Grätzel, Cesium-containing triple cation perovskite solar cells: Improved stability, reproducibility and high efficiency, Energy Environ. Sci. 9 (2016). https://doi.org/10.1039/c5ee03874j.
[56] T.D. Malevu, B.S. Mwankemwa, K.G. Tshabalala, M. Diale, R.O. Ocaya, Effect of 6R and 12R lead iodide polytypes on MAPbI3 perovskite device performance, J. Mater. Sci. Mater. Electron. 29 (2018). https://doi.org/10.1007/s10854-018-9422-4.
[57] P. Nagarjuna, K. Narayanaswamy, T. Swetha, G.H. Rao, S.P. Singh, G.D. Sharma, CH3NH3PbI3 perovskite sensitized solar cells using a D-A copolymer as hole transport material, Electrochim. Acta. 151 (2015) 21–26. https://doi.org/10.1016/j.electacta.2014.11.003.
[58] N.K. Elumalai, M.A. Mahmud, D. Wang, A. Uddin, Perovskite solar cells: Progress and advancements, Energies. 9 (2016). https://doi.org/10.3390/en9110861.
[59] L.C. Chen, J.C. Chen, C.C. Chen, C.G. Wu, Fabrication and Properties of High-Efficiency Perovskite/PCBM Organic Solar Cells, Nanoscale Res. Lett. 10 (2015). https://doi.org/10.1186/s11671-015-1020-2.
[60] N.J. Jeon, J.H. Noh, Y.C. Kim, W.S. Yang, S. Ryu, S. Il Seok, Solvent engineering for high-performance inorganic-organic hybrid perovskite solar cells, Nat. Mater. 13 (2014). https://doi.org/10.1038/nmat4014.
[61] N. Torabi, A. Behjat, Y. Zhou, P. Docampo, R.J. Stoddard, H.W. Hillhouse, T. Ameri, Progress and challenges in perovskite photovoltaics from single- to multi-junction cells, Mater. Today Energy. 12 (2019). https://doi.org/10.1016/j.mtener.2018.12.009.
[62] J. Burschka, N. Pellet, S.J. Moon, R. Humphry-Baker, P. Gao, M.K. Nazeeruddin, M. Grätzel, Sequential deposition as a route to high-performance perovskite-sensitized solar cells, Nature. 499 (2013). https://doi.org/10.1038/nature12340.
[63] Q. Zhao, R. Wu, Z. Zhang, J. Xiong, Z. He, B. Fan, Z. Dai, B. Yang, X. Xue, P. Cai, S. Zhan, X. Zhang, J. Zhang, Achieving efficient inverted planar perovskite solar cells with nondoped PTAA as a hole transport layer, Org. Electron. 71 (2019).

https://doi.org/10.1016/j.orgel.2019.05.019.
[64] Y. Zhou, M. Yang, A.L. Vasiliev, H.F. Garces, Y. Zhao, D. Wang, S. Pang, K. Zhu, N.P. Padture, Growth control of compact CH3NH3PbI3 thin films via enhanced solid-state precursor reaction for efficient planar perovskite solar cells, J. Mater. Chem. A. 3 (2015). https://doi.org/10.1039/c4ta07036d.
[65] W. Li, J. Fan, J. Li, Y. Mai, L. Wang, Controllable grain morphology of perovskite absorber film by molecular self-assembly toward efficient solar cell exceeding 17%, J. Am. Chem. Soc. 137 (2015). https://doi.org/10.1021/jacs.5b06444.
[66] Q. Wang, Y. Shao, H. Xie, L. Lyu, X. Liu, Y. Gao, J. Huang, Qualifying composition dependent p and n self-doping in CH3NH3PbI3, Appl. Phys. Lett. 105 (2014). https://doi.org/10.1063/1.4899051.
[67] H. Zhou, Q. Chen, Y. Yang, Vapor-assisted solution process for perovskite materials and solar cells, MRS Bull. 40 (2015). https://doi.org/10.1557/mrs.2015.171.
[68] S. Chen, L. Lei, S. Yang, Y. Liu, Z.S. Wang, Characterization of Perovskite Obtained from Two-Step Deposition on Mesoporous Titania, ACS Appl. Mater. Interfaces. 7 (2015). https://doi.org/10.1021/acsami.5b07511.
[69] D.B. Khadka, Y. Shirai, M. Yanagida, T. Masuda, K. Miyano, Enhancement in efficiency and optoelectronic quality of perovskite thin films annealed in MACl vapor, Sustain. Energy Fuels. 1 (2017). https://doi.org/10.1039/c7se00033b.
[70] J. Chen, J. Xu, L. Xiao, B. Zhang, S. Dai, J. Yao, Mixed-organic-cation (FA)x(MA)1-xPbI3 planar perovskite solar cells with 16.48% efficiency via a low-pressure vapor-assisted solution process, ACS Appl. Mater. Interfaces. 9 (2017). https://doi.org/10.1021/acsami.6b13410.
[71] M. Liu, M.B. Johnston, H.J. Snaith, Efficient planar heterojunction perovskite solar cells by vapour deposition, Nature. 501 (2013). https://doi.org/10.1038/nature12509.
[72] G. Liang, H. Lan, P. Fan, C. Lan, Z. Zheng, H. Peng, J. Luo, Highly uniform large-area (100 cm2) Perovskite CH3NH3PbI3 thin-films prepared by single-source thermal evaporation, Coatings. 8 (2018). https://doi.org/10.3390/coatings8080256.
[73] T.A. Berhe, W.N. Su, C.H. Chen, C.J. Pan, J.H. Cheng, H.M. Chen, M.C. Tsai, L.Y. Chen, A.A. Dubale, B.J. Hwang, Organometal halide perovskite solar cells: Degradation and stability, Energy Environ. Sci. 9 (2016). https://doi.org/10.1039/c5ee02733k.
[74] G. Han, H.D. Hadi, A. Bruno, S.A. Kulkarni, T.M. Koh, L.H. Wong, C. Soci, N. Mathews, S. Zhang, S.G. Mhaisalkar, Additive Selection Strategy for High Performance Perovskite Photovoltaics, J. Phys. Chem. C. 122 (2018). https://doi.org/10.1021/acs.jpcc.8b00980.
[75] L. Cojocaru, S. Uchida, Y. Sanehira, V. Gonzalez-Pedro, J. Bisquert, J. Nakazaki, T. Kubo, H. Segawa, Temperature effects on the photovoltaic performance of planar structure perovskite solar cells, Chem. Lett. 44 (2015). https://doi.org/10.1246/cl.150781.
[76] U. Bach, D. Lupo, P. Comte, J.E. Moser, F. Weissörtel, J. Salbeck, H. Spreitzer, M. Grätzel, Solid-state dye-sensitized mesoporous TiO2 solar cells with high photon-to-electron conversion efficiencies, Nature. 395 (1998). https://doi.org/10.1038/26936.
[77] S. Jiang, Y. Fang, R. Li, H. Xiao, J. Crowley, C. Wang, T.J. White, W.A. Goddard, Z. Wang, T. Baikie, J. Fang, Pressure-dependent polymorphism and band-gap tuning of methylammonium lead iodide perovskite, Angew. Chemie - Int. Ed. 55 (2016). https://doi.org/10.1002/anie.201601788.
[78] D. Errandonea, D. Santamaria-Perez, D. Martinez-Garcia, O. Gomis, R. Shukla, S.N. Achary, A.K. Tyagi, C. Popescu, Pressure Impact on the Stability and Distortion of the Crystal Structure of CeScO3, Inorg. Chem. 56 (2017).

https://doi.org/10.1021/acs.inorgchem.7b01042.
[79] A. Jaffe, Y. Lin, C.M. Beavers, J. Voss, W.L. Mao, H.I. Karunadasa, High-pressure single-crystal structures of 3D lead-halide hybrid perovskites and pressure effects on their electronic and optical properties, ACS Cent. Sci. 2 (2016). https://doi.org/10.1021/acscentsci.6b00055.
[80] G. Niu, X. Guo, L. Wang, Review of recent progress in chemical stability of perovskite solar cells, J. Mater. Chem. A. 3 (2015). https://doi.org/10.1039/c4ta04994b.
[81] M. Shirayama, M. Kato, T. Miyadera, T. Sugita, T. Fujiseki, S. Hara, H. Kadowaki, D. Murata, M. Chikamatsu, H. Fujiwara, Degradation mechanism of CH3NH3PbI3 perovskite materials upon exposure to humid air, J. Appl. Phys. 119 (2016). https://doi.org/10.1063/1.4943638.
[82] J. Yang, B.D. Siempelkamp, D. Liu, T.L. Kelly, Investigation of CH3NH3PbI3degradation rates and mechanisms in controlled humidity environments using in situ techniques, ACS Nano. 9 (2015) 1955–1963. https://doi.org/10.1021/nn506864k.
[83] S.W. Lee, S. Kim, S. Bae, K. Cho, T. Chung, L.E. Mundt, S. Lee, S. Park, H. Park, M.C. Schubert, S.W. Glunz, Y. Ko, Y. Jun, Y. Kang, H.S. Lee, D. Kim, UV Degradation and Recovery of Perovskite Solar Cells, Sci. Rep. 6 (2016). https://doi.org/10.1038/srep38150.
[84] D. Fabini, Quantifying the Potential for Lead Pollution from Halide Perovskite Photovoltaics, J. Phys. Chem. Lett. 6 (2015). https://doi.org/10.1021/acs.jpclett.5b01747.
[85] N.K. Noel, S.D. Stranks, A. Abate, C. Wehrenfennig, S. Guarnera, A.A. Haghighirad, A. Sadhanala, G.E. Eperon, S.K. Pathak, M.B. Johnston, A. Petrozza, L.M. Herz, H.J. Snaith, Lead-free organic-inorganic tin halide perovskites for photovoltaic applications, Energy Environ. Sci. 7 (2014). https://doi.org/10.1039/c4ee01076k.
[86] H. Hoshi, N. Shigeeda, T. Dai, Improved oxidation stability of tin iodide cubic perovskite treated by 5-ammonium valeric acid iodide, Mater. Lett. 183 (2016). https://doi.org/10.1016/j.matlet.2016.07.048.
[87] H.L. Zhu, J. Xiao, J. Mao, H. Zhang, Y. Zhao, W.C.H. Choy, Controllable Crystallization of CH3NH3Sn0.25Pb0.75I3 Perovskites for Hysteresis-Free Solar Cells with Efficiency Reaching 15.2%, Adv. Funct. Mater. 27 (2017). https://doi.org/10.1002/adfm.201605469.

Chapter 3

Preparation methods and Characterization techniques

3.1 Overview

This chapter presents the experimental methods used in the preparation of titanium dioxide (TiO_2) nanoparticles and the fabrication of the perovskite solar cell (PSC) device. The research characterization techniques and setup used in this study are also discussed.

3.2 Experimental methods

3.2.1 Synthesis of titanium dioxide nanoparticles

The TiO_2 nanoparticles were synthesized using the hydrothermal method. Chemical reagents used during preparation were used as supplied from the manufacture without any further purification. The gel was prepared by mixing 45 mL of deionized water with 15 mL of hydrochloric acid (Sigma-Aldrich) under constant stirring for 5 min in a fume hood. 2 mL of titanium (IV) isopropoxide (Sigma-Aldrich) was added to the solution under a constant stirring for 10 min. The mixture was transferred into a preheated Teflon-lined stainless steel autoclave oven at 100 ℃ for 2 hours (hrs) and then allowed to cool at room temperature before centrifugation. The collected white particles were washed several times using deionized water and finally vacuum dried. The as-prepared nano-powders were divided into five samples, placed in a furnace, and annealed for 2 hrs in an open-air atmosphere at different T_a of 200, 400, 800, 1000, and 1200 ℃. **Figure 3.1** shows a schematic diagram of TiO_2 nano-powder hydrothermal preparation.

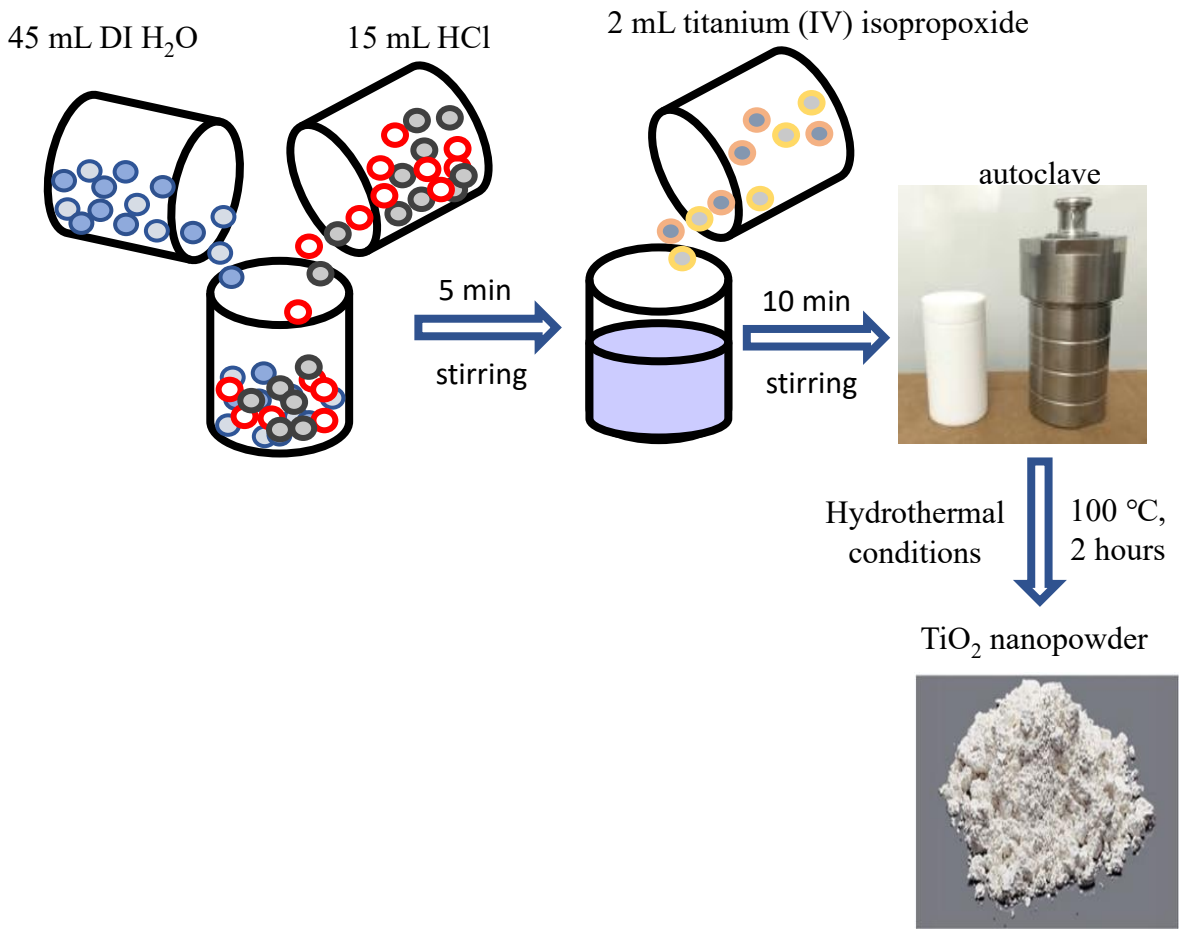

Figure 3.1: Schematic representation of TiO_2 hydrothermal preparation method.

3.2.2 Perovskite solar cell device fabrication

The solar cells were fabricated on a transparent glass substrate by a simple doctor blade and two-step spin coating methods. ITO glass substrates (Sigma-Aldrich) were first cleaned with a detergent and ultrasonicated three times using water, isopropanol, and ethanol for 20 minutes separately. The glass substrates were later allowed to dry at ambient atmosphere thereafter subjected to UV-Ozone cleaning for a period of 15 minutes. To form a dense compact TiO_2 blocking layer, the UV-Ozone cleaned substrates were coated with a 0.15 M titanium diisopropoxide bis(acetylacetonate) (75% in isopropanol, Sigma-Aldrich) in 1-butanol by spin-coating at 2000 rpm for 20s which were then heated at 100 ℃ for 5 min. After the coated glass substrates were allowed to cool at room temperature the process was repeated two times using a 0.3 M titanium diisopropoxide bis(acetylacetonate). Following the three-times coating of titanium diisopropoxide bis(acetylacetonate) the glass substrates were then heated at 250 ℃ for 15 minutes and allowed to cool at room temperature. A few micrometer thick layer of mesoporous-TiO_2 photoelectrode was formed from a paste of the synthesized TiO_2. Pastes of TiO_2 were obtained by dissolving the synthesized and annealed TiO_2 nanopowders in ethanol (Sigma-Aldrich). The micrometer thick layers were coated over the compact layer using the doctor blade technique thereafter the substrates were heated at 250 ℃ for 45 minutes. From

here the substrates/photoelectrodes were treated with a 0.02 M $TiCl_4$ (98%, Sigma-Aldrich) solution maintained at 80 ℃ for 10 minutes, washed with deionized water, and dried at 100 ℃ in an open atmosphere. A single halide perovskite layer of $CH_3NH_3PbI_3$-($MAPbI_3$) was formed by two-step spin coating of PbI_2 and MAI at ambient conditions (relative humidity= 45-60%) to form TiO_2/$MAPbI_3$ heterogeneous thin films. Firstly, a solution of 0.02 ml of 1 M PbI_2 (4.61g) in a solvent mixture of DMF: DMSO (3:1) prepared at 70 ℃ was spin-coated over the mesoporous TiO_2 layers at 3000 rpm for 10s without loading time. The ITO/c-TiO_2/m-TiO_2/PbI_2 glass substrates were then dried at 100 ℃ for 10 minutes and allowed to cool to room temperature. The perovskite layer was completed by spin-coating 0.2 ml of 0.038 M CH_3NH_3I at 4000 rpm for 20s with a loading time of 20s. The ITO/c-TiO_2/m-TiO_2/$MAPbI_3$ glass substrates were then dried at 100 ℃ for 10 minutes. A 0.02 ml solution of spiro-MeOTAD was spin-coated over the perovskite bearing substrated at 3500 rpm for 35s. The spiro-MeOTAD deposited solution was obtained by dissolving 0.072g of spiro-MeOTAD (Sigma-Aldrich) in 1 ml chlorobenzene (Sigma-Aldrich) solvent. This was followed by the addition of 0.029 ml 4-*tert*-butyl pyridine (Sigma-Aldrich) and 0.018 ml (0.52g) lithium bis(trifluoromethanesulfonyl)imide in 1 ml acetonitrile (Sigma-Aldrich) solutions. The counter electrode was obtained by using silver (Ag) ink on an opposite ITO substrate. Approximately 80 % of the ITO substrate was covered with a deposition mask and a conductive Ag ink (Sigma-Aldrich) was deposited over the exposed area via doctor blade technique. The solar cells were assembled by preheating the TiO_2 coated substrates at 100 ℃ for 5 minutes thereafter clamped with the opposite Ag coated electrodes. The fabricated cells were then heated at 100 ℃ for 15 minutes to form solar cells with device architecture of ITO/c-TiO_2/m-TiO_2/$MAPbI_3$/Ag/ITO. **Figure 3.2** shows a schematic diagram of the final devices.

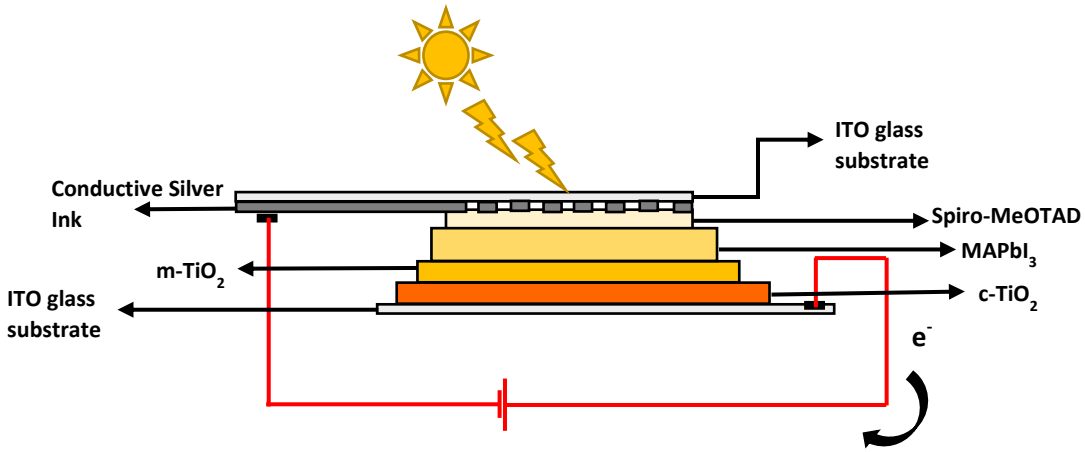

Figure 3.2: Schematic representation of the fabricated solar cell with device architecture ITO/c-TiO_2/m-TiO_2/$MAPbI_3$/Spiro-MeoTAD/Conductive Ag ink/ITO.

3.3 Characterization techniques

3.3.1 X-ray diffraction (XRD

X-ray diffraction (XRD) is a non-destructive technique used to characterize the crystal structure of either crystalline or amorphous thin film and powder samples. From the collected XRD data the characteristic structural parameters such as phase structure, purity, crystalline size, crystallinity, orientations, crystal stress, strain, defects, and lattice parameters can be determined [1]. At first, the XRD probes the crystal structure of the sample with an X-ray beam of a single wavelength (λ). The crystal structure of a sample consists of a periodic array of atoms forming atomic planes separated by a distance (d). When the incident beam strikes the atomic planes, X-rays are elastically scattered at a specific diffraction angle (θ) by electron clouds around atoms in each atomic plane as shown in **Figure 3.3**. The diffractometer measures the scattered X-rays as a function of diffraction angle. Sharp prominent X-ray diffraction peaks occur at specific diffraction angles due to constructive interference from the periodic crystal structure of a crystalline sample whereas amorphous samples do not produce any diffraction peaks due to the randomly orientated crystal structure. Diffractions from the atomic planes are observed only when the scattered monochromatic beam satisfy Bragg's law given by equation 1 below:

$$n\lambda = 2d\sin(\theta) \tag{1}$$

Bragg's law defined the relationship between X-ray wavelength, the distance between planes, and diffraction angle. Whereby n- represents integer numbers, λ- X-ray diffraction wavelength, d- the distance between the atomic planes, and θ- diffraction angle.

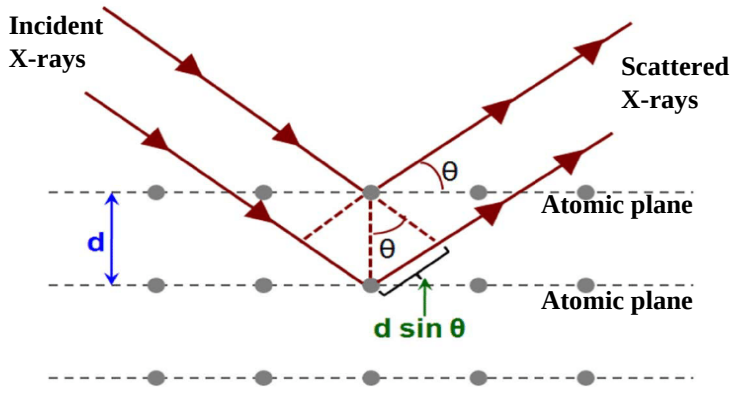

Figure 3.3: Schematic representation of Bragg's law for X-ray diffraction [2].

The resulting diffractogram is a characteristic diffraction pattern to the unknown sample crystal structure. Therefore, the diffractogram is compared with standard diffraction lines from the XRD database. With the knowledge of d-values, relative peak intensity, full width at half maximum (FWHM). The percentage purity of a sample can be determined from the proportion of impurities, the degree of crystallinity can be determined from the peak broadness and peak intensities, the lattice parameter a, b and c can be determined from the d-spacing, and the material average crystallin size can be calculated from and FWHM using equations 2, called the Debye-Scherrer equation:

$$D = \frac{k\lambda}{\beta\mathrm{Cos}(\theta)} \tag{2}$$

From the Scherrer equation, D represents the crystalline size, *K*- Scherrer constant ($K = 0.9$), λ- x-ray wavelength, β represents the full width at half maximum (FWHM) of a diffraction peak located at angle 2θ diffraction angle.

Experimental setup

The crystal structure and crystalline size of the synthesized TiO_2 nanoparticles were determined using a Bruker-AXS D8 Advance XRD diffractometer (Bruker Corporation of Germany) operating at 40 kV/4 Ma and Cu Kα = 0.15406 nm with a 2θ diffraction angle in the range of 20 to 80°.

3.3.2 Scanning Electron Microscopy (SEM)

Scanning electron microscopy (SEM) is a powerful characterization technique used for microscopic surface imaging of samples. It produces high-resolution images revealing features of up to 5 to 1 nanometer on the surface of a sample. SEM is very useful in studying the surface structure of nanomaterials [3,4]. Its principal basis of operation uses an electron beam generated from a tungsten (W) or lanthanum hexaboride (LaB_6) filament to probe the surface of a sample. **Figure 3.4** demonstrates the SEM basis of operation up to data acquisition. The instrument is equipped with an electromagnetic condenser and objective lenses which focus the high-energy electron beam into a fine probe over the near-surface region [5,6].

The interactions between the electron beam and sample emit low-energy secondary electrons (SE), backscattered electrons (BSE), and x-ray radiations. The emitted signals are collected by the detector, amplified, and fed to a computer that displays microscopic images of the surface structure giving insight information on the sample's topography, morphology, crystalline structure, and chemical composition [7,8]. The SE are excited electrons released from the surface of the sample and BSE are the incident electrons reflected of the nuclei of atoms making up the sample. Therefore, SE micrographs determine the surface topography, morphology (surface texture), and crystalline structure of the analyzed sample, whereas BSE determines elemental chemical composition making the material. X-ray radiations (discussed in EDX below) are also important emissions from the sample used for analytical chemical analysis. These emissions are not detected or form part of SEM surface imaging.

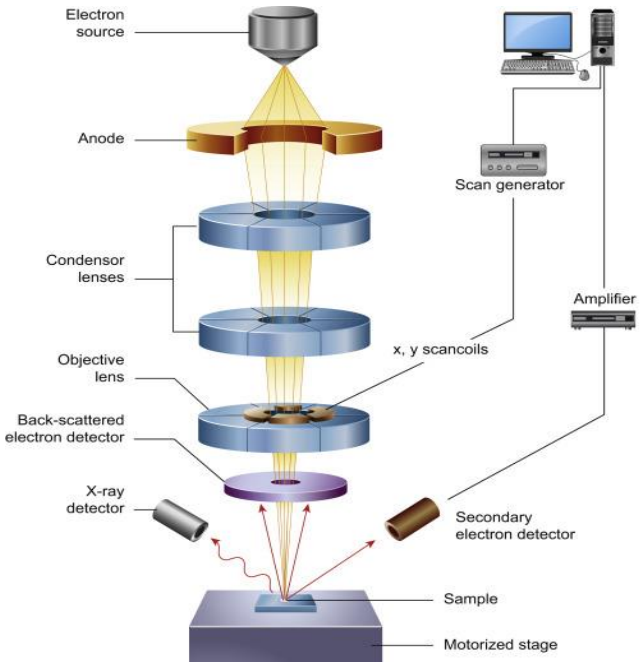

Figure 3.4: Schematic representation of scanning electron microscope instrument setup [6]**.**

Experimental setup

In this study, two different SEM instruments were used in the analysis of TiO_2 nanoparticles and the prepared $TiO_2/MAPbI_3$ heterogeneous thin films: (1) The morphologies and chemical compositions of TiO_2 nanoparticles were obtained using a field emission SEM (FE-SEM) coupled with EDX, Zeiss SEM-Microscopes Crossbeam 540. (2) The surface structure and analytical analysis of $TiO_2/MAPbI_3$ heterogeneous thin-films were studied using a TESCAN VEGAN3 scanning electron microscopy (OXFORD X-MAX^N) coupled with EDX operated at 20 kv. The surface of the samples was sputter-coated with carbon to produce conductive coating onto the samples.

3.3.3 Energy-dispersive X-ray spectroscopy (EDX)

X-ray or photon radiations introduced in scanning electron microscopy (see **Figure 5**) form the basis of energy-dispersive x-ray spectroscopy (EDX). EDX characterization tool is in conjunction with SEM providing qualitative and quantitative analysis of elements present in a sample. X-ray emissions result from electronic transitions from higher to lower shells of atoms making up a material. In EDX, the high-energy incident electron beam excites electrons around the K, L, and M shells of atoms making the sample, leaving behind holes. As electrons from outer/higher atomic shells transition to fill the open vacancies in the inner/lower atomic shells x-ray radiations are emitted from the sample. These electronic transitions are characteristic fingerprints for every element making up the sample. An x-ray spectrum is generated providing quantitative and qualitative details of each chemical element present in a given sample [9].

3.3.4 Fourier-Transform Infrared spectroscopy (FT-IR)

Fourier transform infrared spectroscopy (FT-IR) uses vibrational modes from chemical bonds and functional groups present in organic and inorganic molecules to identify the unknown molecular structure of gaseous, liquid, and solid samples. The technique uses the basis that molecules have unique bond strength, length, and geometries which causes unique stretching and bending vibrational modes characteristic fingerprint to a molecule when infrared radiation is absorption. During sample analysis, IR radiation is directed to a sample by mirrors and lenses, the sample produces an IR spectrum between a region 4000 to 400 cm^{-1} wavenumber, from here the characteristic absorption bands are observed and associated with the corresponding bonds and functional groups. **Figure 3.5** represents FT-IR instrumental setup.

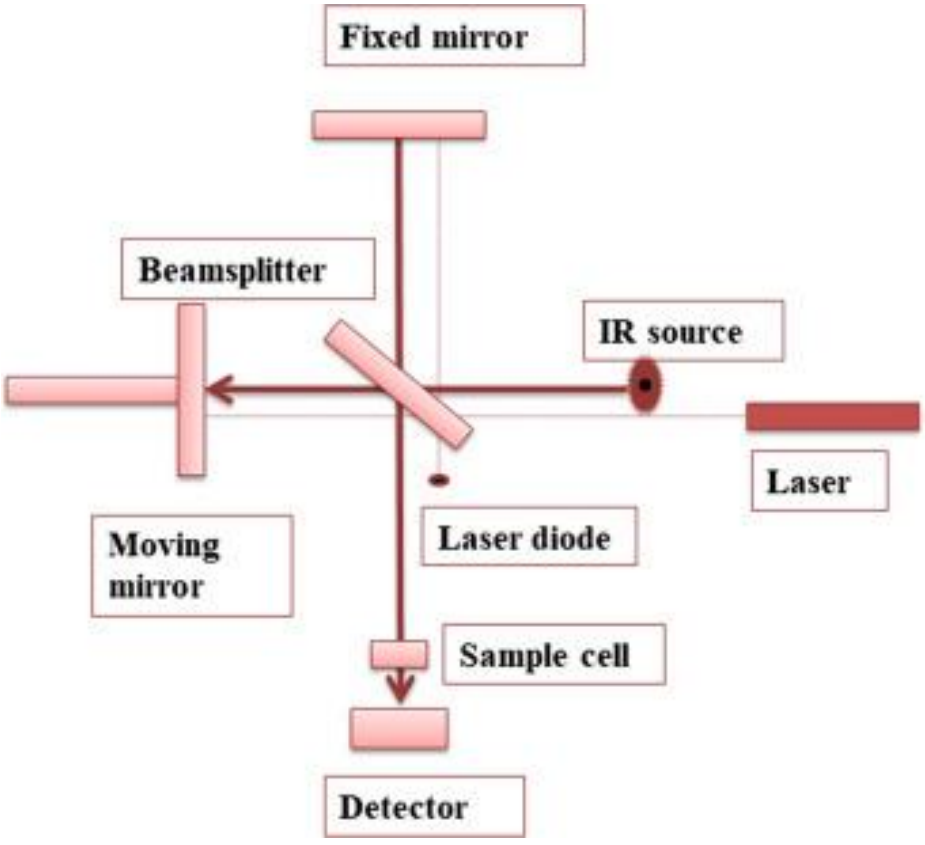

Figure 3.5: Schematic representation of FT-IR instrument setup [10]**.**

Experimental setup

A Perkin-Elmer Spectrum 100 Fourier-transform infrared (FT-IR) spectroscope fitted with an attenuated total reflection (ATR) detector, FT-IR spectrometer was used in this study to identify functional groups.

3.3.5 Ultraviolet-visible spectroscopy (UV-vis)

Ultraviolet-visible spectroscopy (UV-vis) is a non-destructive quantitative characterization technique used to investigate optical properties of a sample such as absorption, transmittance, and reflectance. UV-vis spectroscopy further determines the bandgap energy of semiconducting materials. The technique uses the fact that a sample absorbs a specific wavelength of light in the UV-vis region to excite electrons from the highest occupied molecular orbital (HOMO) to the lowest unoccupied molecular orbital (LUMO). This is interpreted by comparing the light intensity through a sample and reference cell giving rise to the Beer-Lambert law described by equation 3. **Figure 3.6** demonstrates the instrument set and working principle. The spectrophotometer consists of a deuterium and tungsten light source, a monochromator, a beam splitter, a sample cell, reference cells, and detectors. The deuterium and tungsten light sources emit UV (100-400nm) and visible (400-700nm) radiations, respectively. The radiations are directed towards the monochromator. The first monochromator slit ensures that the emitted UV-vis radiations travel parallel towards the diffraction grating. The orientation of the diffraction grating separates the light radiation into several discrete monochromatic beams. The second monochromatic slit allows only one wavelength beam to pass. The beam splitter divides the monochromatic beam into two identical beams of equal intensities. The identical beams are then transmitted through a sample cell and a reference cell. After the beams pass through the sample and reference cells, semiconducting photodetectors (e.g., photodiodes or charge couple devices) covert the light intensities into current signals. The signals are thereafter displayed as a spectrum of percentage transmittance/absorbance against wavelength.

$$e^{-A} = (\frac{I}{I_0}) \tag{3}$$

Equation 3 represents Beer-Lambert law whereby A represents ab

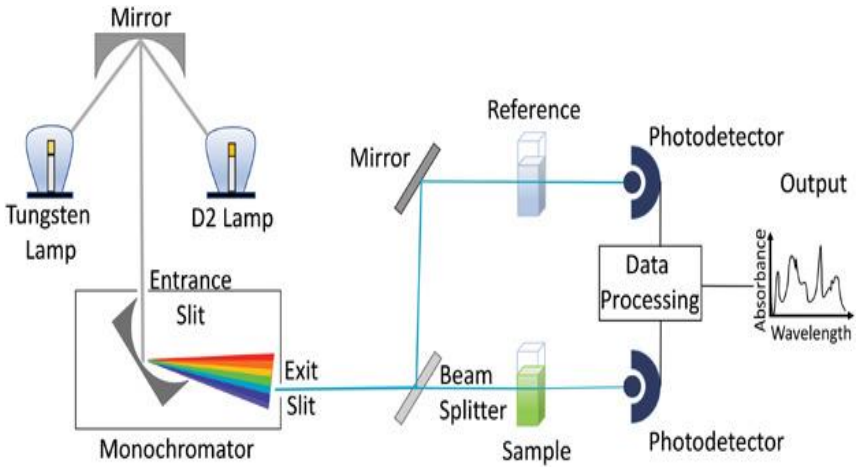

Figure 3.6: Schematic representation of Ultraviolet-visible spectroscope instrument setup [11].

Experimental setup

The optical properties were studied using the Perkin-Elmer Lambda 950 UV-Vis spectrometer. To obtain the UV absorption spectra from UV-Vis spectroscopy analysis, dilute solutions of

TiO_2 nanoparticles were prepared by dispersing TiO_2 nanopowder samples into an ethanol solvent via sonication. A cuvette filled with ethanol was used as a reference cell.

3.3.6 Thermogravimetric Analysis (TGA)

Thermogravimetric analysis (TGA) belongs to a family of thermal analysis techniques. The technique is normally used in polymers, polymer blends, and composites to characterize the thermal behavior and degradation mechanism of a sample at controlled temperatures and atmospheres. During characterization, the mass of the sample is measured as a function of temperature or time at a constant heating rate to high temperatures. TGA analysis can be carried out under a range of atmospheres such as inert atmosphere (N_2) and oxidation atmosphere (O_2). The degradation steps observed in the TGA curve can further be used to quantify constituting materials within a multicomponent sample. **Figure 3.7** demonstrates TGA experimental setup. The heart of the instrument is equipped with a furnace, thermocouple, sample pan (basket) suspended by a wire and connected to a microbalance located above the furnace. During characterization, a computer is connected to a thermocouple and microbalance collects data displaying a TGA curve of mass percentage as a function of temperature or time. Instrument mass calibration is frequently performed to provide reproducible results. Standard metals such as silver and aluminum are supplied along with the instrument for calibration.

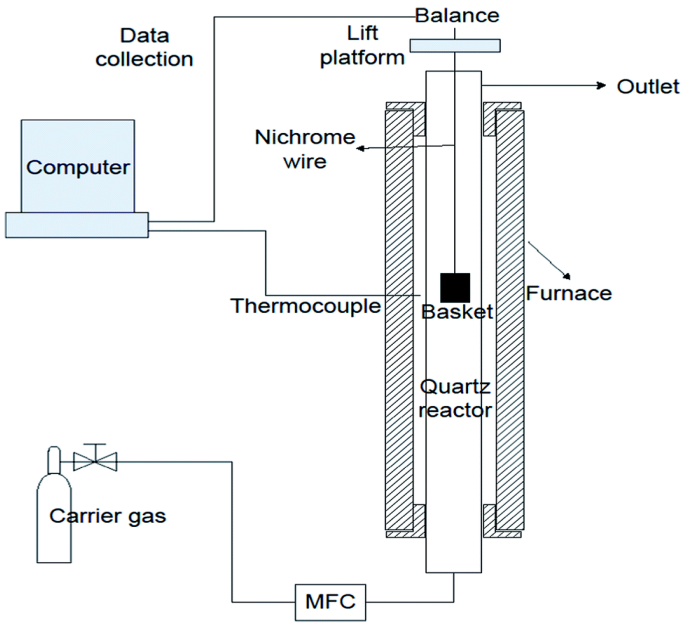

Figure 3.7: Schematic representation of thermogravimetric analyzer instrument set [12].

Experimental setup

To characterize the thermal behavior of the samples Perkin-Elmer STA6000 thermogravimetric analyzer (TGA) was used. 20-25 mg of the photoanode/perovskite was obtained by scraping the $TiO_2/MAPbI_3$ heterogeneous thin films off the ITO conductive substrate. The samples were heated at 10 °Cmin^{-1} from ambient to 800 °C under 20 mLmin^{-1}nitrogen flow.

3.3.7 Photoluminescence spectroscopy (PL)

Photoluminescence spectroscopy (PL) is a non-destructive characterization technique used to probe the electronic structure of materials, more importantly in semiconductor physics. From the obtained PL spectrum, material properties such as bandgap energy, impurity levels, defect states, and recombination pathways are determined. At first, a sample is illuminated with a light source. Photons with sufficient energy from the light source are absorbed by the sample material. The absorbed photon energy causes the excitation of electrons from the valence band to the conduction band. Generally, photoexcited electrons have excess energy which is subsequently lost occupying the lowest energy level from the conduction band. These electrons eventually fall back to the highest energy level in the valence band. The energy released during the conduction band to valence band interband transitions is directly related to the material's bandgap energy also referred to as the forbidden gap, this results in the emission of luminescence photons from the sample. Hence the process of photoexcitation and emission in a sample is referred to as photoluminescence. It is worth noting that at normal conditions electrons are not allowed in the forbidden gap. Intraband transitions are observed from defect levels within the forbidden gap. In metal oxide semiconductors, the bandgap structure can be modified for specific end-use by induction of defect levels such as impurities and oxygen vacancies. This is achieved through doping, alloying, and annealing metal oxides.

Experimental setup

Photoluminescence spectroscopy (PL) characterization was performed on as-prepared TiO_2 nanopowder, annealed TiO_2 nanopowder, and TiO_2/$MAPbI_3$ heterogeneous films under a Carry Eclipse Fluorescence spectrophotometer with a 150W xenon lamp (λ_{ex}= 238 nm).

3.3.8 Solar simulator

The solar simulator is a versatile research and industrial instrument used to characterize the performance of different solar devices such as photovoltaic cells, photochemical batteries, and thermal power generators. The instrument can further be used in research fields studying the behavior of materials under light exposure such as cosmetic products, paints, plastics, and textiles. The instrument is equipped with a xenon light source (150 W) coupled with an AM1.5 filter that produces radiation that is closely related to natural solar radiation. In this study for small lab-based solar cells a Newport Oriel LCS-100 solar simulator, Keithley source meter, and computer software were used to characterize the fabricated device performances. A standard silicon solar cell supplied with the solar simulator was used to calibrate the software, solar simulator, and Keithley source meter. During characterization important electrical parameters such as short circuit current (J_{sc}), open-circuit voltage (V_{oc}), fill factor (FF), shunt resistance (R_{SH}), and series resistance (R_S) data are acquired. The power conversion efficiency is calculated from equation 3 below, whereby "P_{in}" represents power provided by the solar simulator and "A" represents the solar cell active area.

$$\eta = \frac{V_{oc}.J_{sc}.FF}{P_{in}} = \frac{V_{oc}.J_{sc}.FF}{A.1000\ W/m} \quad (3)$$

Figure 3.8 and **equation 4** represent a theoretical single diode model, equivalent to a photovoltaic device used in the electrical parameter analyses.

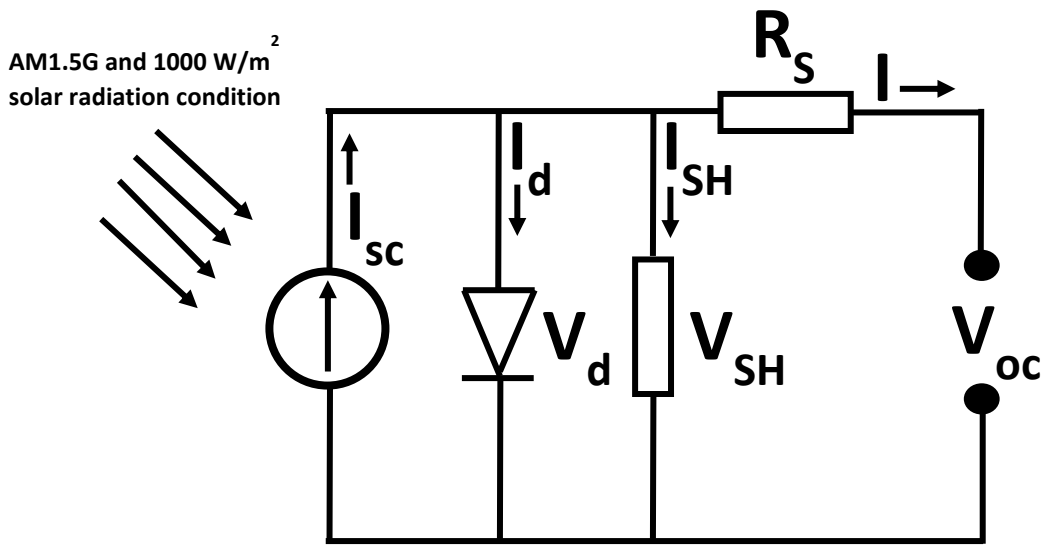

Figure 3.8: Schematic diagram of a single diode model demonstrating the basic operation and origin of photovoltaic parameters.

$$I = I_{sc} - I_o\left\{e^{\left(\frac{q(V_{oc}+IR_s)}{aKT}\right)} - 1\right\} - \frac{V_{oc}+IR_s}{R_{SH}} \quad (4)$$

Experimental setup

The electrical properties of the final devices with an active area of 3 cm^2 = $3x10^{-4}$ m^2 were measured using Newport Oriel LCS-100 solar simulator and Keithley source meter (Keithley 2450) under AM1.5G and 1000 W/m^2 standard irradiation test conditions calibrated from a standard Si-based solar cell.

References

[1] Chauhan, A. (2014) Powder XRD Technique and its Applications in Science and Technology. *Journal of Analytical & Bioanalytical Techniques*, **5**, pp.1-5. https://doi.org/10.4172/2155-9872.1000212

[2] Sulochamadevi, B. (2010) Structure and Regulation of Yeast Glycogen Synthase. *Advances in Neurobiology*, (Doctoral dissertation).

[3] Gimeno Adelantado, J. V., Ferrer Eres, M.A., Valle Algarra, F.M., Peris Vicente, J. and Bosch Reig, F. (2003) Analytical study by SEM/EDX and metallographic

techniques of materials used in the iron production process during the iberian period. *Talanta*, **60**, pp.895-910. https://doi.org/10.1016/S0039-9140(03)00152-8

[4] Sukontapatipark, W., El-Agroudi, M.A., Selliseth, N.J., Thunold, K. and Selvig, K.A. (2001) Bacterial colonization associated with fixed orthodontic appliances. A scanning electron microscopy study. *European Journal of Orthodontics*, **23**, pp.475-484. https://doi.org/10.1093/ejo/23.5.475

[5] Pretorius, E. (2010) Influence of acceleration voltage on scanning electron microscopy of human blood platelets. *Microscopy Research and Technique*, **73**, pp.225-228. https://doi.org/10.1002/jemt.20778

[6] Inkson, B.J. (2016) Scanning Electron Microscopy (SEM) and Transmission Electron Microscopy (TEM) for Materials Characterization. *Materials Characterization Using Nondestructive Evaluation (NDE) Methods*, p. 17-43. https://doi.org/10.1016/B978-0-08-100040-3.00002-X

[7] Vernon-Parry, K.D. (2000) Scanning electron microscopy: An introduction. *III-Vs Review*, **13**, pp.40-44. https://doi.org/10.1016/S0961-1290(00)80006-X

[8] Zhou, W., Apkarian, R., Wang, Z.L. and Joy, D. (2006) Fundamentals of scanning electron microscopy (SEM). *Scanning Microscopy for Nanotechnology: Techniques and Applications*, p. 1-40. https://doi.org/10.1007/978-0-387-39620-0_1

[9] Girão, A.V., Caputo, G. and Ferro, M.C. (2017) Application of Scanning Electron Microscopy–Energy Dispersive X-Ray Spectroscopy (SEM-EDS). *Comprehensive Analytical Chemistry*, **75**, 153-168. https://doi.org/10.1016/bs.coac.2016.10.002

[10] Titus, D., James Jebaseelan Samuel, E. and Roopan, S.M. (2019) Nanoparticle characterization techniques. *Green Synthesis, Characterization and Applications of Nanoparticles*, Elsevier. 303–19. https://doi.org/10.1016/B978-0-08-102579-6.00012-5

[11] Rocha, F.S., Gomes, A.J., Lunardi, C.N., Kaliaguine, S. and Patience, G.S. (2018) Experimental methods in chemical engineering: Ultraviolet visible spectroscopy—UV-Vis. *Canadian Journal of Chemical Engineering*, **96**, pp.2512-2517. https://doi.org/10.1002/cjce.23344

[12] Zhou, H., Long, Y., Meng, A., Chen, S., Li, Q. and Zhang, Y. (2015) A novel method for kinetics analysis of pyrolysis of hemicellulose, cellulose, and lignin in TGA and macro-TGA. *RSC Advances*, **5**, pp.26509-26516. https://doi.org/10.1039/c5ra02715b

Chapter 4

Investigation on structural, morphological, and optical studies of multiphase titanium dioxide nanoparticles

4.1 Overview

Multiphase titanium dioxide (TiO_2) nanoparticles were successfully synthesized using the hydrothermal method. The as-prepared nanoparticles were subjected to different annealing temperatures (T_a) to investigate their effects on the structural, morphological, and opto-chemical properties using X-ray diffraction (XRD), transmission electron microscopy (TEM), Scanning electron microscopy (SEM), Energy dispersive x-ray (EDX) spectroscopy, Fourier transform infrared spectroscopy (FT-IR), and Ultraviolet-visible spectrometry (UV-Vis)

techniques. As T_a is increased from 200 to 1200 °C, the TiO_2 nanoparticles appear to have a stable tetragonal crystal structure throughout the various T_a. XRD measurements indicate an extended presence of mixed anatase-rutile phase composition with a slow phase transformation mechanism. The crystalline size of both the anatase and rutile phase increases from 19 to 38 nm and 18 -57 nm, respectively. The behaviour in the lattice parameter indicates that increasing T_a forces the crystalline structure in both phases to expand. Images from TEM and SEM micrographs reveal a similar morphology in agreement with XRD measurements. The micrographs reveal that increasing T_a increases material porosity and the dispersion of well-defined TiO_2 nanostructure. The EDX spectroscopy confirms the successful synthesis of TiO_2 nanoparticles with the absence of impurities after annealing. FT-IR confirms vibrational modes and bond behaviour associated with the expected titanium and oxygen elements with T_a. The UV-Vis spectroscopy characterizes changes in the multiphase TiO_2 optical properties as the T_a is increased. An intense UV absorption is reported in the results section and its importance in solar cell applications is stated in the conclusion.

Keywords: hydrothermal, nanoparticles, porosity, morphology, annealing, impurities, and bandgap, absorption.

4.2 Introduction

Titanium dioxide (TiO_2), commonly known as titania, is one of the extensively studied metal oxides as it occurs naturally and fortunately available in the three most abundant crystalline phases: rutile, anatase, and brookite [1,2]. Material scientists cannot get over its use in application primarily due to its non-toxicity and compatibility with the environment [3]. There are various synthetic routes applied in an attempt to maximise its applications [4,5]. Those routes lead to well-known nanostructures that include nanosheets, nanoparticles, nanowires, nanorods, and nanotubes [6,7]. Common popular applications of TiO_2 nanostructures include coatings, biosensors, photocatalysis, and photovoltaics (PVs) as semiconducting material [8–10].

TiO_2 is a promising n-type semiconductor responsible for charge selection and transport [11]. Large surface coverage of TiO_2 nanomaterials (NMs) results in high-performance devices due to the material's photostability, slow degradation mechanism, excellent electronic properties and efficiency. The morphology and structure in the NMs differ with the type of TiO_2 polymorph [12,13]. Among the three abundant phases, the low-temperature brookite phase is limited to practical applications and increases the difficulty to study TiO_2 at extreme temperatures. This indicates that brookite is a less ordered crystallographic phase. In contrast to the brookite phase, rutile is the most studied and thermodynamically stable phase, whereas the anatase phase is metastable with an ease phase transition to the thermodynamically stable rutile phase by thermal treatment [14–16]. **Table 4.1** summarises the variation of lattice parameters with the phase and space groups.

Table 4.1: Properties of brookite, anatase, and rutile titanium dioxide (TiO_2) polymorphic states.

Phase	Space groups	Lattice parameters (Å)			Crystal systems	Thermal stability	Ref
		A	b	c			
Brookite	Pbca	9.18	5.45	5.15	Orthorhombic	Low	[16]
Anatase	$I4_1/amd$	3.78	-	9.52	Tetragonal	low	[16]
Rutile	$P4_2/mnm$	4.59	-	2.96	Tetragonal	High	[17]

The metastable anatase phase is the most preferred in PVs due to its balance in surface area and crystallinity which results in unique properties such as the low recombination rates, high conductivity, and in particular excellent morphologies required for solar cell applications [17–20]. In PVs such as dye-sensitized solar cells (DSSCs), organic solar cells (OSCs), and the emerging hybrid perovskite solar cells (PSCs) TiO_2 photoanodes are widely fabricated and reported in a porous structure on transparent conductive oxide (TCO) substrates as structural support for light active materials for a proper charge selection, reduction in diffusion length and maximum electron transfer to the external circuit [21–23].

To improve PV performance, studies on TiO_2 NMs have focused on what effect does extreme conditions such as temperature, pressure, and pH have on TiO_2 nanoparticles (NPs). Short- and long-range phase transitions are reported in response to the type and magnitude of condition the material is subjected to [15,20]. New interesting physical and chemical properties materialize as the particle size of TiO_2 is substantially reduced to nanometre scales. This is accompanied by changes in the crystal structure, morphology, and optical properties. Recently annealing (T_a) of synthesized TiO_2 is the leading approach in altering its nanostructure and subsequently changing its functional chemical and physical properties such as surface free energy, phase composition, crystallinity, lattice structure, crystalline size, particle size, pore size, material purity, bandgap structure, and photocatalytic properties [24–26].

Therefore, optimizing TiO_2 NPs optical, crystal, and morphological properties is required to intensify and extend the material's application as a photoanode in solar cell devices. In a recent study, Muthee *et al* [27] investigated the effect of T_a on TiO_2 NPs in a temperature range of 450-750 ℃ prepared by sol-gel technique. The synthesized TiO_2 NPs appears to be amorphous. Lower T_a encourages anatase-phase formation at 450 ℃. Further annealing initiates TiO_2 anatase to rutile phase transition with a complete rutile-phase formation at 650 ℃. Characterization of the material shows T_a increases the NPs degree of crystallinity, crystalline, and particle size, and decreases the material-specific surface area and bandgap structure. Bakri et al [28] reported a similar trend in TiO_2 thin films prepared by sol-gel dip coating. Hossain et al [29] prepared mixed-phase anatase: rutile-TiO_2 thin-films via the low-temperature sol-gel method of mixing two titanium precursors. Their reported surface morphology reveals a high level of spherical NP agglomeration. In another study, Sarode *et al* [30] reported that annealing of the spherical TiO_2 NP morphology results in a less agglomerated surface structure, forming spaces of pores within the material's nanocrystalline morphology. Such nanoporous morphologies are required in photoanodes of TiO_2 NPs to increase the surface contact area and also act as a structural scaffold for light-active materials in solar cell devices [31]. In addition,

it is observed that increasing T_a alters the TiO_2 bandgap structure by decreasing the bandgap energy, this behaviour is further associated with the increase in crystalline size and a decrease in specific surface area. The effect of annealing TiO_2 thin films has mainly been reported on sol-gel techniques with a subsequent end-use in applications in either anatase or rutile-phase [32,33]. Synergistic properties are reported in applications (e.g., photocatalytic reactions and PVs) using mixed-phase anatase: rutile TiO_2 NPs [34,35]. However high efficiencies in PV cells are subjected to a careful optimization of TiO_2 phase composition/phase content [36,37]. In this study, mixed-phase TiO_2 nanopowder was synthesized by hydrothermal technique and annealed at temperatures from 200 to 1200 ℃. A similar preparation route has already been reported for solar cell applications by Malevu *et al* [38] and Ntsikelelo *et al* [39].

In the hydrothermal preparation method, TiO_2 results in well crystalline anatase: rutile mixed-phase material at a relative ratio. Despite the difference in phases, post-T_a treatment of TiO_2 NPs from hydrothermal increases crystallinity and improves surface morphology by inducing particle aggregation and growth similar to reports in sol-gel technique [40,41]. However, the hydrothermal method is advantageous due to the production of particles that are superior in crystal perfection and grain boundaries with an effective anatase/rutile-(A/R) interface electron transfer for solar energy conversion [42]. In literature studies, there is limited research effort on the effect of T_a on mixed (A: R) phase TiO_2 NPs prepared from hydrothermal. Among the studies of TiO_2 synthesis, it is apparent that phase existence in TiO_2 NPs depends on the preparation technique, preparation conditions, titanium precursor, alkoxide precursor solvent, and/or the inorganic acid catalyst [43]. Although in each preparation technique, the first formation of nanocrystalline A-phase from the amorphous state is evident, this is attributed to the TiO_2 NPs to favour the less constrained crystal structure and the low surface energy A-phase [26]. Subsequently followed by (A to R)-phase transition at high temperatures. In the sol-gel technique (uses titanium + alkoxide precursor), R-phase is only found at elevated temperatures (T_a) [27]. Apart from T_a TiO_2 NPs from sol-gel preparation, R-phase formation can occur at low-temperature conditions in the hydrothermal method (uses titanium + inorganic acid catalyst). In this case, the immense pressure in the hydrothermal preparation of crystalline TiO_2 NPs promotes rutile crystal formation by precipitating the material from the sol [44]. In a work done by Wu *et al* [12] a small fraction of the brookite (B)-phase is reported to occur in hydrothermal preparation in the absence of the inorganic acid catalyst and low concentrations of the strong acids encourages A, B, and R-phase coexistence. However, the B-phase is substantially reduced to null at higher concentrations of the acid catalyst.

This study, therefore, investigates the effect of T_a on structural, morphological, and optical properties of multiphase (A: R) TiO_2 nanopowder synthesized by hydrothermal method for solar cell applications. The obtained nanocrystals were annealed at various temperatures to evaluate the effect of T_a on nanostructure crystallinity, crystallite size, phase composition, morphology, and optical properties. The hydrothermal synthesis results in a pure multiphase TiO_2 NM with anatase and rutile-phase competing phenomenon. The material shows a tunable wide-bandgap structure and extended anatase (A) to rutile (R) phase transition. The degree of crystallinity increased due to the induced crystal growth. The surface morphology shows that T_a tailers the multiphase TiO_2 nanoparticles surface structure by increasing the porosity required for PV applications.

4.3 Methods

The TiO_2 nanoparticles were synthesized using the hydrothermal method. Chemical reagents used during preparation were used as supplied from the manufacture without any further purification. The gel was prepared by mixing 45 mL of deionized water with 15 mL of hydrochloric acid (Sigma-Aldrich) under constant stirring for 5 min in a fume hood. 2 mL of titanium (IV) isopropoxide (Sigma-Aldrich) was added to the solution under a constant stirring for 10 min. The mixture was transferred into a preheated Teflon lined stainless steel autoclave oven at 100 ℃ for 2 hours (hrs) and then allowed to cool at room temperature before centrifugation. The collected white particles were washed several times using deionized water and finally vacuum dried. The as-prepared nano-powders were divided into five samples, placed in a furnace and annealed for 2 hrs in an open-air atmosphere at different T_a of 200, 400, 800, 1000, and 1200 ℃. Thereafter the samples were placed under characterization using various techniques described below.

4.4 Characterization

The crystal structure and crystalline size were determined using a Bruker-AXS D8 Advance XRD diffractometer (Bruker Corporation of Germany) operating at 40 kV/4 Ma and Cu Kα = 0.15406 nm with a 2θ diffraction angle in the range of 20 to 80°. TEM (TEM, JEOL JEM-2100) was used to examine the average particle size of the nanocrystalline TiO_2. Before TEM analyses, TiO_2 NPs were uniformly dispersed in ethanol using a sonicator for 30 min. This was followed by drop-casting onto a carbon-coated copper grid and drying at room temperature (RT) before loading in the chamber. The morphologies and chemical compositions were obtained using a field emission SEM (FE-SEM) coupled with EDX, Zeiss SEM-Microscopes Crossbeam 540. FT-IR spectroscopy using a Perkin-Elmer spectrum 100 FTIR spectrophotometer was used to determine functional groups from powder TiO_2 nanomaterial. The optical properties were studied using the Perkin-Elmer Lambda 950 UV-Vis spectrometer.

4.5 Results and Discussion

4.5.1 X-ray diffraction (XRD)

Figure 4.1 shows the XRD characteristic pattern of the as-prepared TiO_2 NPs. The NPs are identified to have multiple nanophases at a relative ratio [45,46]. Both rutile (R) (indicated by *) and anatase (A) (indicated by #) phases are present in the as-prepared TiO_2 sample in **Figure 4.1 (a)**. The diffraction peaks corresponding to the A-phase as per JCPDS no. 21-1272 are assigned to (101), (103), (004), (210), (200), (105), (215), (204), (116), and (220) crystallographic planes [47,48]. The presence of R-phase at a small peak ratio is observed at

peaks associated with the (110), (200), (211) and (310) crystallographic planes as per JCPDS no. 21-1276 [49,50]. The peak ratio of A relative to R present in the as-prepared TiO_2 sample is determined to be 3:1 using peaks associated with the planes described above. No additional phases are observed from the diffraction pattern.

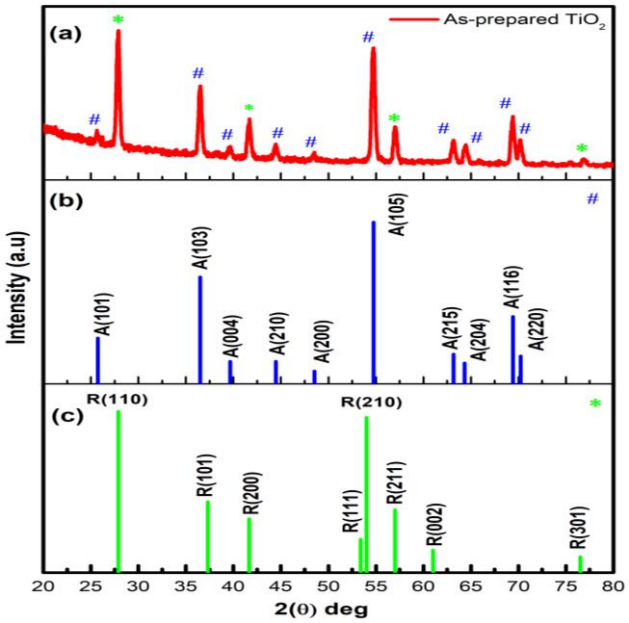

Figure 4.1: XRD pattern of the as-prepared TiO_2 NPs with crystal structure matched from standard JCPDS database. (a) XRD pattern of as-prepared TiO_2 sample, (b). anatase standard JCPDS no. 21-1272, and (c) rutile standard JCPDS no. 21-1276.

The XRD patterns in **Figure 4.2** show the crystal phase behaviour of the as-prepared TiO_2 NPs at various T_a ranging from 200 - 1200 °C. No generation of new peaks associated with other TiO_2 phases (e.g., brookite phase) is observed throughout various T_a. This suggests that the TiO_2 NPs retain a tetragonal crystal structure throughout different T_a. Moreover, this outcome further justifies the good stability in the TiO_2 lattice structure [14]. The lattice parameter (for A-phase) ***a***, ***b***, and ***c*** in which ***a*** = ***b***, were calculated using equation (1) [47]. The equation allows the use of any (hkl) values in the lattice parameter determination. The results are presented in **Table 4.2**.

$$\frac{1}{d_{hkl}^2} = \frac{h^2 + k^2}{a^2} + \frac{l^2}{c^2} \qquad (1)$$

Herein, the complex (103) and (105) crystal planes with *d*-spacing of d_{103} = 2.462 Å and d_{105} = 1.677 Å are used, which represent the intense and characteristic peaks of the more dominant A-phase in the multiphase TiO_2 NPs. Also considering that calculations that use complex miller indices can cater for simple miller indices such as (hk0) and (00l). Substitution of the above (hkl) values and *d*-spacing in equation (1), both unknown ***a*** and ***c*** remain as shown in equations (2) and (3) respectively.

For the (103) plane with d_{103} = 2.462 Å spacing,

$$\frac{1}{a^2} = \frac{1}{h_{103}^2 + k_{103}^2}\left(\frac{1}{d_{103}^2} - \frac{l_{103}^2}{c^2}\right) \qquad (2)$$

and for the (105) plane with d_{105} = 1.678 Å spacing,

$$\frac{l_{105}^2}{c^2} = \frac{1}{d_{105}^2} - \frac{1}{a^2}(h_{105}^2 + k_{105}^2) \quad (3)$$

Substitution of equation (2) into (3) and solving the resulting expression leads to:

$$\frac{1}{c^2} = \frac{\frac{1}{d_{105}^2} - (\frac{1}{d_{103}^2})(\frac{h_{105}^2 + k_{105}^2}{h_{103}^2 + k_{103}^2})}{l_{105}^2 - l_{103}^2(\frac{h_{105}^2 + k_{105}^2}{h_{103}^2 + k_{103}^2})} \quad (4)$$

Equation (4) applies to any miller indices in the XRD patterns and results in approximately equal ***a*** and ***c*** values with negligible standard deviation. Using the (103) and (105) planes the lattice constants are obtained as shown in **Table 4.2** with results that are comparable to those previously reported in the literature [51,52]. A similar approach is undertaken in lattice parameter determination for the R-phase using peaks associated with R (110) and R (211) crystal planes.

As illustrated in **Figure 4.2 and Table 4.2**, the observed decrease in peak broadness (FWHM) of the A (105) and R (110) dominate peaks indicates that the degree of crystallinity in the TiO_2 NPs increases with an increase in T_a [53]. Additionally, the rise and fall in peak intensities indicate that T_a initiates phase transition in the multiphase TiO_2 samples with the onset of A to R-phase transition occurring at $T_a \geq 400$ °C. A similar phase transition behaviour is reported by Byrne *et al* in traditional single-phase TiO_2 NPs. [54]. Furthermore, the NPs experience induced crystal growth as T_a is increased above 400 °C [52,55].

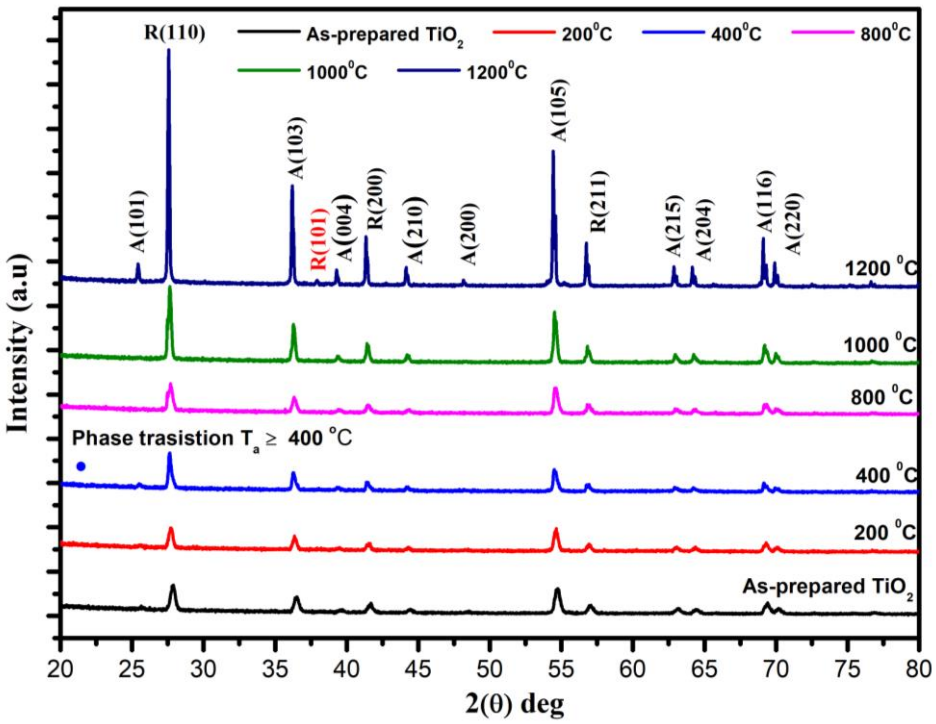

Figure 4.2: XRD patterns of the as-prepared TiO_2 (black) and annealed TiO_2 samples at 200 °C (red), 400 °C (blue), 800 °C (pink), 1000 °C (green), and 1200 °C (dark blue).

Table 4.2: Tabulated XRD results showing the effect of T_a on A (105) and R (110) crystallographic planes.

Sample (s)	A (105)					R (110)				
	2(θ)°	FWHM (°)	D (nm)	Lattice parameter		2(θ)°	FWHM (°)	D (nm)	Lattice parameter	
				a (Å)	c (Å)				a (Å)	c (Å)
As-prepared	54.7	0.42	19	4.16	9.16	27.9	0.43	18	4.53	2.68
200 ℃	54.6	0.38	21	4.21	9.16	27.7	0.41	19	4.55	2.66
400 ℃	54.5	0.35	22	4.21	9.18	27.6	0.26	31	4.57	2.65
800 ℃	54.5	0.37	21	4.20	9.17	27.7	0.46	17	4.56	2.65
1000 ℃	54.5	0.27	29	4.22	9.18	27.6	0.29	27	4.57	2.66
1200 ℃	54.4	0.21	38	4.25	9.19	27.5	0.14	57	4.58	2.66

As presented in **Table 4.2**, the average crystalline size (D) estimated using Scherrer equation (5) increases with an increase in T_a for both A and R-phases. This justifies the increase in peak intensities observed in **Figure 4.2**. Literature studies report that TiO_2 samples at T_a greater than 600 ℃ display a decrease in A and an increase in R lattice parameter, similarly a decrease in A crystalline size and an increase in R crystalline size, followed by end of phase transition at 800 ℃ [56,57]. However, the experimental data reported in **Table 4.2** in this work does not correlate with the previous literature. The unusual TiO_2 lattice behaviour is explained by that the nanocrystalline A-phase is highly stable and therefore results in a slow A to R-phase transition with the R-phase becoming more dominant at T_a= 1200 ℃ as confirmed by the appearance of R (101) peak [39,58].

$$D = \frac{K\lambda}{\beta cos\theta} \tag{5}$$

From the Scherrer equation (5) K represents Scherrer constant (K = 0.9), λ represents x-ray wavelength, β represents full width at half maximum (FWHM) in units of radians, and θ represents Bragg's diffraction angle in units of degrees. To further characterize the crystal phase behaviour in the multiphase TiO_2 NPs the XRD patterns in **Figure 4.2** were utilized to give better insights into phase transition with changes in T_a. The impact of T_a on phase composition is more pronounced at A (105) and R (110) characteristic peaks. The phase ratio of A to R in the multiphase TiO_2 NPs at various T_a is calculated from equations (6) and (7), given by [59]:

$$f_A = \frac{1}{1 + 1.26(\frac{I_R}{I_A})} X\ 100 \tag{6}$$

$$f_R = 100 - f_A \tag{7}$$

Whereby the calculated f_A and f_R represents phase composition of anatase and rutile, respective and their corresponding peak intensities at various T_a are given by I_A and I_R. **Figure 4.3** shows

the graphical effect of T_a on TiO_2 phase composition. **Figure 4.3** depicts a similar trend in TiO_2 (A to R)-phase composition previously reported in the literature [29]. Initially, the A-phase ratio is higher than the R-phase. In this study increasing T_a shows a pronounced inverse phase ratio behaviour ($f_R \propto \frac{1}{f_A}$) throughout the various T_a indicating that the A to R-phase transition is a nucleation and growth process. Increasing T_a to 200 ℃ substantially decreases the A-phase content. However, a noticeable change in phase behaviour is observed at T_a= 400 ℃ confirming the proposed onset of phase transition reported in **Figure 4.2**. At this point (T_a > 400 ℃), the phase composition shows an irregular trend with a slight increase in A-phase content followed by R-phase formation becoming more dominant at T_a= 800 to 1200 ℃. This observed slight increase in the A-phase and the R-phase formation has been previously reported in the literature by Ding *et al* [60] as a TiO_2 A and R-phase competing phenomenon.

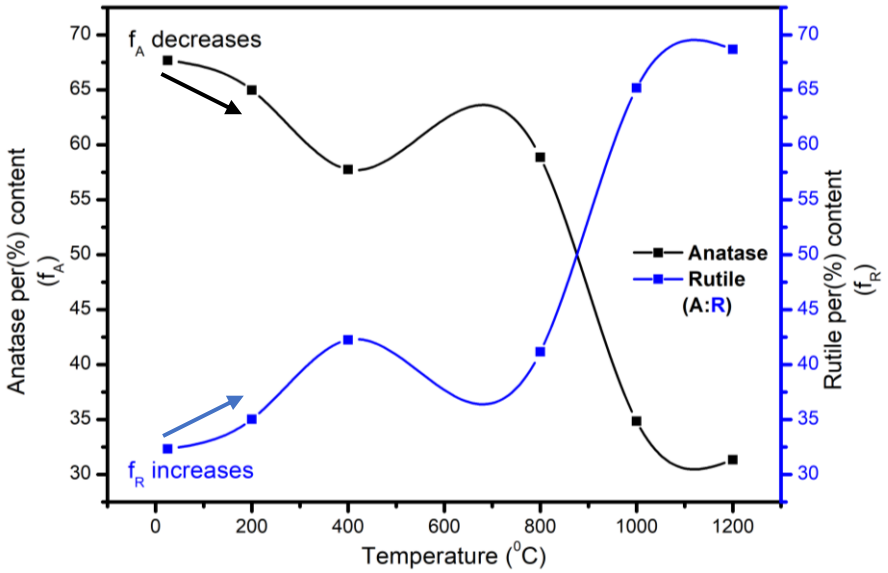

Figure 4.3: Percentage phase content of anatase and rutile at various Ta in the TiO_2 NPs.

Figure 4.4 (a) and (b) illustrates magnified XRD patterns at selected R (110) and A (105) crystallographic planes, respectively. In both magnified parts a distinctive shift in peak position to lower diffraction angles is observed with increasing T_a. This signifies that there are changes in lattice parameters in both the A and R-phase. This is in good agreement with results reported in **Table 4.2,** that the increase in T_a increases lattice parameters in both A and R-phases and also indicates that the increase in material crystalline size (D) in both phases is due to thermal expansion [61].

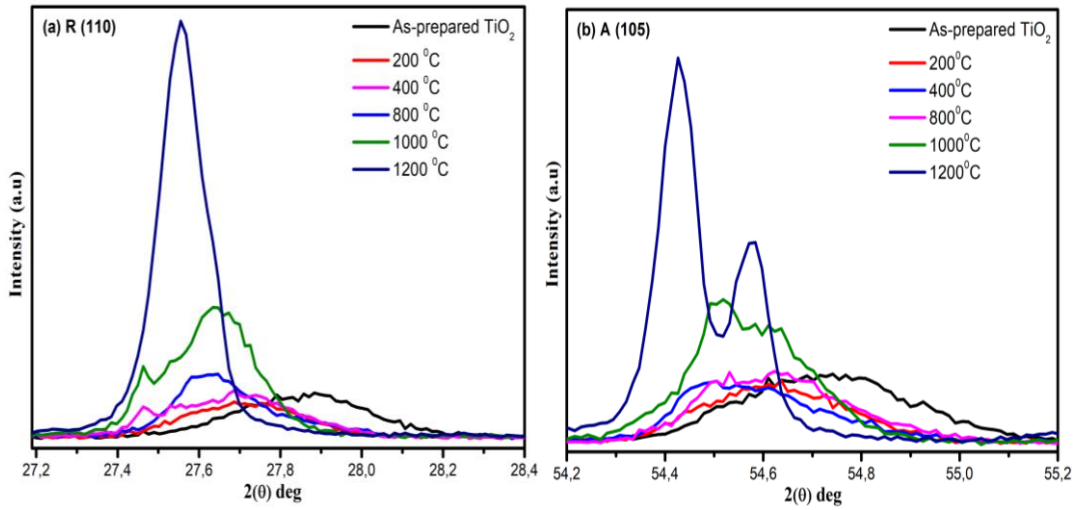

Figure 4.4: Magnified XRD patterns at peaks assigned to the (a) R (110), (b) A (105) crystallographic planes.

4.5.2 Transmission Electron Microscopy

Figure 4.5 shows magnified TEM images used to investigate the effect of T_a on the as-prepared TiO_2 particle size. From literature studies, the observed contrast in colour and non-uniform particle size in microscopic imaging of the multiphase TiO_2 samples are distinctive features demonstrating A and R-phase identification [45,62]. From **Figure 4.5 (a)** and **(b)**, the TiO_2 NPs annealed at 200 ℃ in **Figure 4.5 (b)** show the same morphology as the as-prepared TiO_2 in **Figure 4.5 (a)**. A similar trend is noted from the XRD spectra indicating that the as-prepared and annealed TiO_2 at 200 ℃ samples have the same degree of crystallinity indicated by the comparable peak intensities. Additionally, the increase in particle size with the increasing T_a is consistent with the increase in crystalline size determined from XRD analysis. The as-prepared TiO_2 sample shows a high particle agglomeration at a relatively small surface area which reduces particle size. In a similar study Pal *et al* [57] reported that at low T_a, particles with undefined shape and size in the TiO_2 NMs are loosely packed together forming thermally unstable particle agglomerates in the TiO_2 NM. Following careful interpretation from the TEM images, such unstable morphology is also observed in this study and annealing of the TiO_2 NM allows the cluster to separate and grow into well-defined nanostructures as shown in **Figure 4.5 (f)**. The measured average particle size from the as-prepared and annealed TiO_2 samples is shown to increase from 188 to 489 nm, respectively.

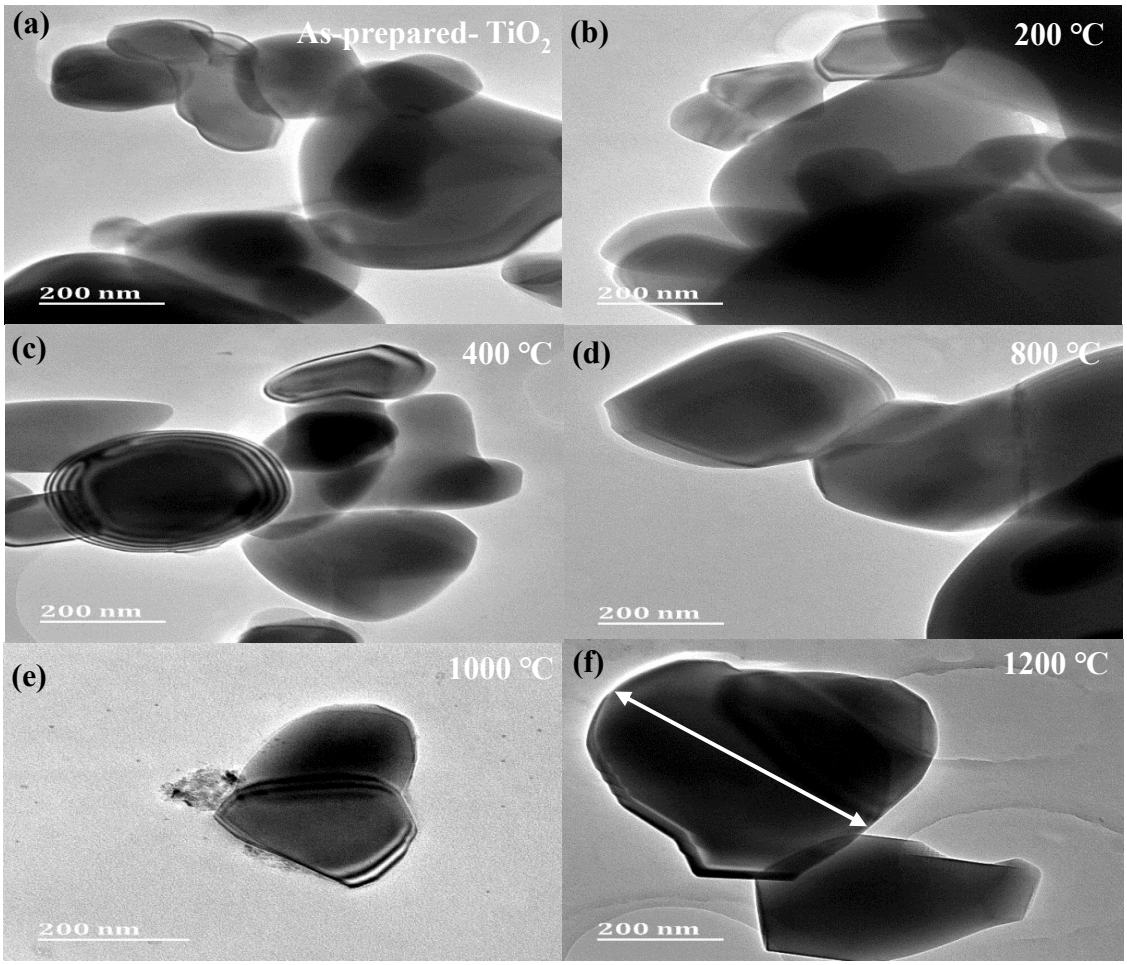

Figure 4.5: TEM images of as-prepared and annealed TiO_2 powder samples. (a), As-prepared TiO_2, (b) 200 ℃, (c) 400 ℃, (d) 800 ℃, (e) 1000 ℃ and (f) 1200 ℃.

4.5.3 Scanning Electron Microscopy (SEM)

Figure 4.6 shows SEM micrographs of the prepared samples. Imaging in SEM reveals a similar nanostructure reported in TEM. At low T_a, SEM micrographs show a surface structure with a uniform particle distribution of unevenly shaped NPs from the multiphase TiO_2 NM. The as-prepared and annealed TiO_2 sample at T_a = 200 ℃ shows a similar morphology. Increasing T_a to 400 ℃, the morphology in the NM appears to coarsen indicating the onset of phase transition described in XRD analysis. The effect of T_a has significant changes in the morphology as it leads to the development of nanosphere structures as marked (with cycles) in **Figure 4.6 (f)** and the development of dark regions for TiO_2 NPs annealed at 800 to 1200 ℃ indicating porosity [63,64]. This suggests that the increase in T_a assist the TiO_2 material to overcome internal stresses and other forces in the nanostructure as a result of the occurrence of phase transition [15]. The increasing porosity in the surface morphology is attributed to the separation in the TiO_2 NP cluster with the increase in T_a discussed in the TEM analysis. The surface structure attained in the TiO_2 at high T_a is unique for solar cells applications, as there are appreciable spatial gaps (high porosity) between the NPs indicating a mesoporous scaffold

morphology widely reported, that in turn will increase the interfacial contact with the photoactive layer. Similar results have been reported by Malevu *et al* [38].

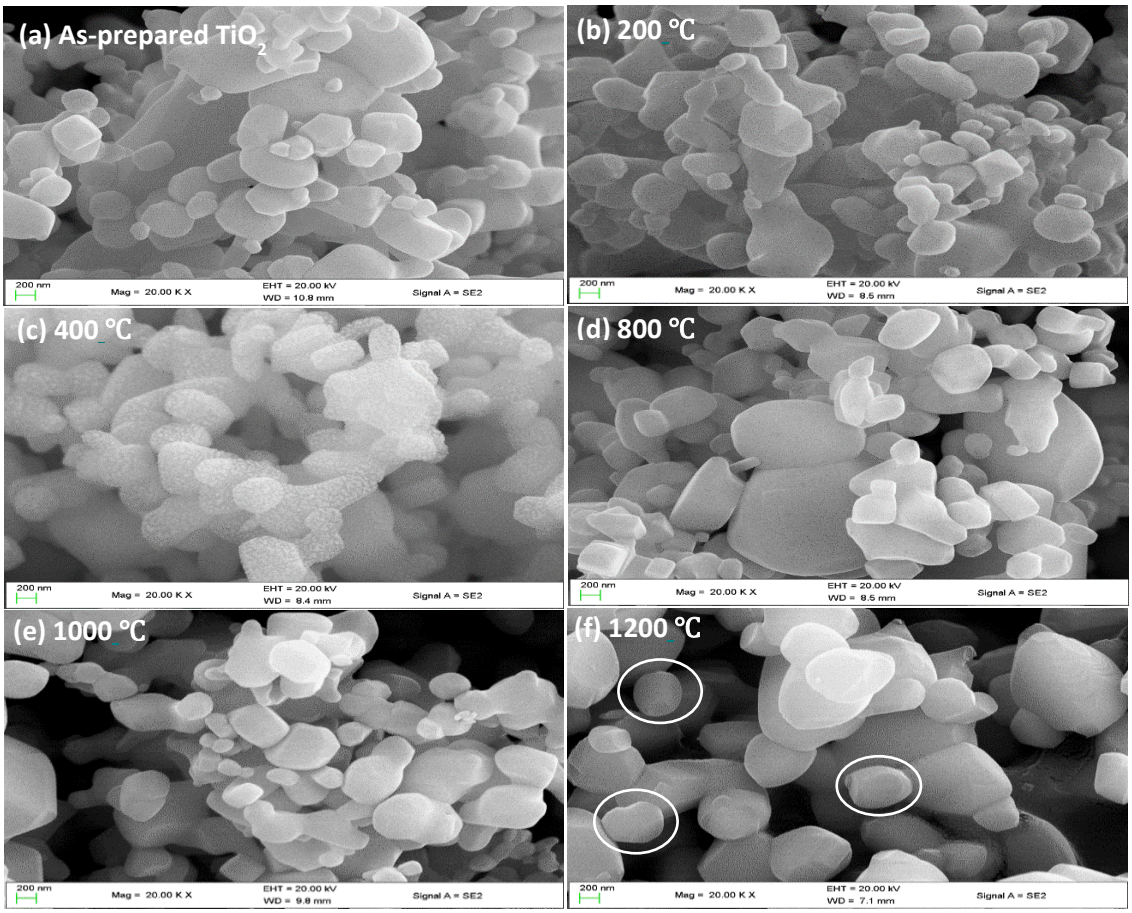

Figure 4.6: SEM micrographs showing arrangement of morphology in the as-prepared and annealed TiO_2 samples. (a) As-prepared TiO_2, (b) 200 ℃, (c) 400 ℃, (d) 800 ℃, (e) 1000 ℃ and (f) 1200 ℃.

4.5.4 Energy dispersive x-ray (EDX) spectroscopy

Figure 4.7 and **Table 4.3** represents the TiO_2 energy dispersive x-ray (EDX) spectroscopy results. The EDX analysis revealed successful synthesis of TiO_2 samples composed mainly of expected titanium (Ti) and oxygen (O) elements in their innermost energy level, with zero presence of impurities. The EDX spectrum shows the presence of carbon (C) element attributed to carbon coating before sample characterization.

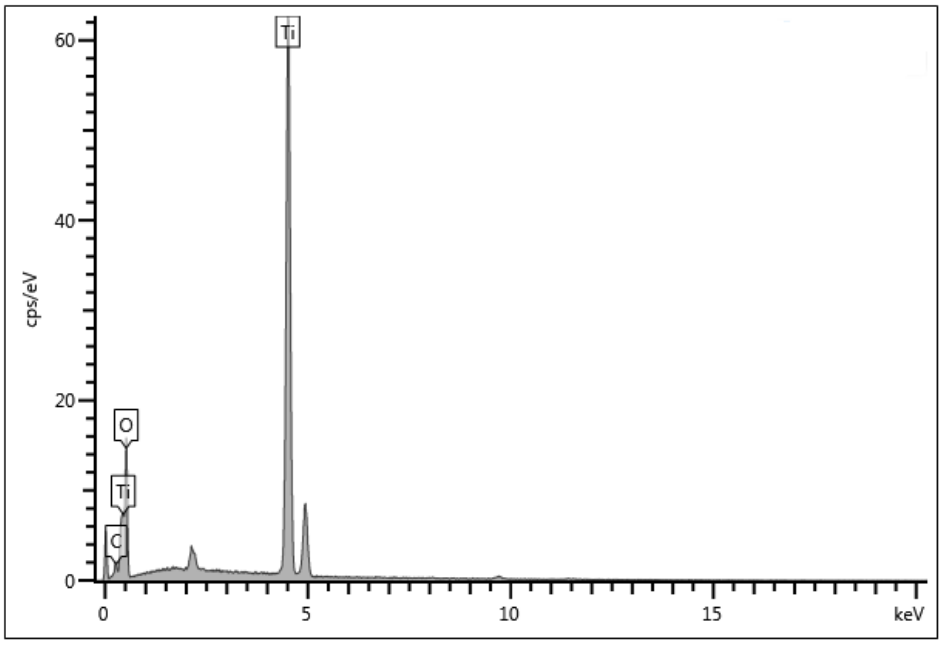

Figure 4.7: EDX spectrum of as-prepared TiO_2.

Table 4.3: Tabulated TiO_2 elemental composition.

As-prepared-TiO_2	O	Ti	Total
wt%	42.93	57.07	100.00

4.5.5 Fourier Transform Infrared (FT-IR) spectroscopy

FT-IR spectroscopy was used to identify functional groups from the hydrothermally prepared TiO_2 powder samples. The activity of the FT-IR spectra for the as-prepared and annealed TiO_2 samples was recorded in the wavenumber range of 250 to 4000 cm^{-1} as shown in **Figure 4.8**. Regions of interest from the multiphase TiO_2 NPs are identified at 414.94 to 860.07, 1220.97, 1367.80, 1745.57, and 2924.79 cm^{-1}. The characteristic broadband indicated by dotted lines from 414.94 to 860.07 cm^{-1} is associated with bond stretching and bending vibrations of the Ti-O-Ti framework in the TiO_6 tetragonal chemical structure [65]. The vibrational band that appears at 1745.57 cm^{-1} is attributed to the bond stretching mode from the hydroxyl (-OH) group and absorbed water (H-O-H) molecules on the TiO_2 surface during sample preparation [66,67]. Peaks centred at 1220.97 and 1367.80 cm^{-1} are assigned to Ti-O-Ti bending modes associated with rutile (R) and anatase (A)-phase respectively. The presence of organic residue is observed by the absorption band centred at 2924.79 cm^{-1} [68]. It is observed that the broad absorption peak centred at 414.94 to 860.07 cm^{-1} decreases in intensity and increases in peak broadness as T_a is gradually increased indicating the presence of phase change in the material [39].

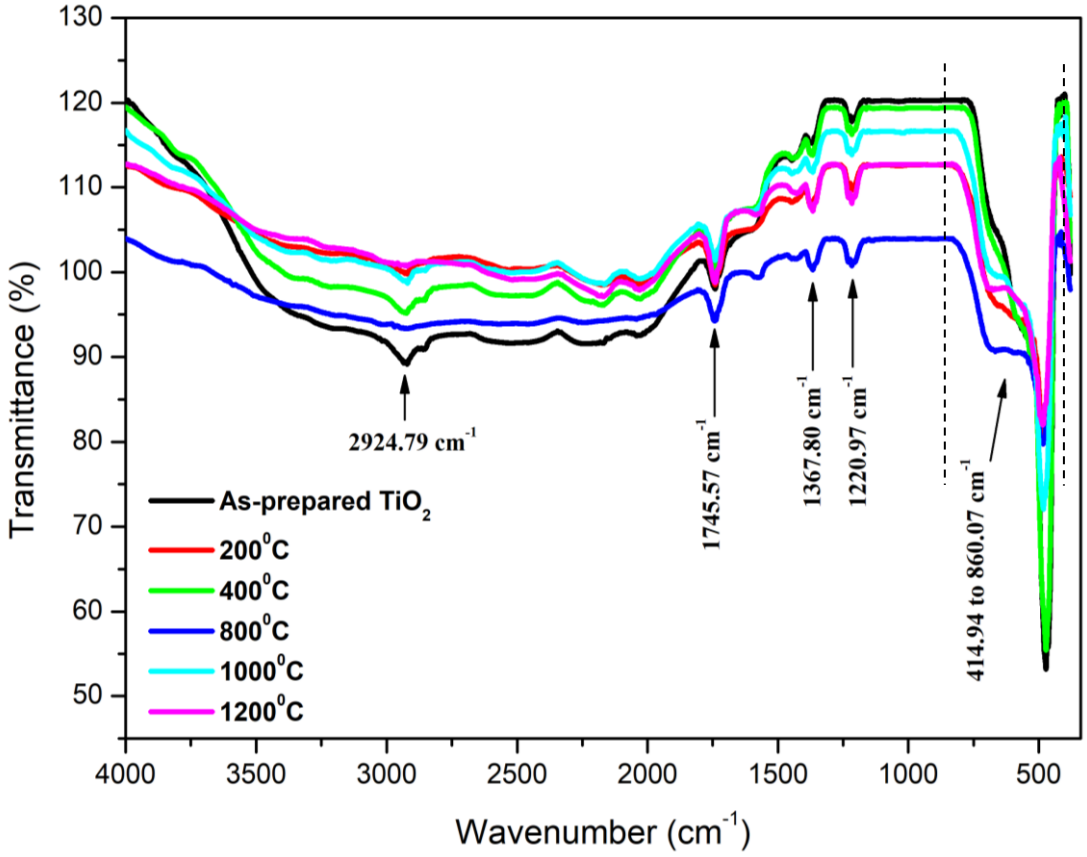

Figure 4.8: FT-IR response of powder TiO_2 samples with various T_a.

4.5.6 Ultraviolet-visible (UV-Vis) spectroscopy

UV-Vis spectroscopy was used to characterize the effect of T_a on TiO_2 optical properties. **Figure 4.9 (a)** shows the absorption spectra of the as-prepared and annealed TiO_2 samples measured from 200 to 700 nm wavelengths. The samples exhibit a slight red shift in absorption edge at various T_a with strong absorption in the UV region. Furthermore, it is observed from the absorption spectra that there is a slight increase followed by an apparent decrease in optical absorption with increasing T_a. The TiO_2 absorption is enhanced by T_a with a maximum absorbance recorded for the sample annealed at 800 ℃. From literature studies, it is reported that the A-phase is more photoactive than the R-phase [69]. Therefore, the trend in absorption spectra reported above indicates that the absorption coefficient of the multiphase (A: R) TiO_2 is significantly changed by T_a due to phase transition in the material towards the less photoactive R-phase. Similar results have been reported by Ntsikelelo *et al* [39]. In addition to the optical property studies, bandgap energies (E_g) of the as-prepared and annealed TiO_2 samples were determined by the Tauc plot in **Figure 4.9 (b)** given by equation (6) which plots the material's absorption coefficient $(\alpha h\nu)^n$ against photon energy ($h\nu$) [63]:

$$(\alpha h\nu)^n = A(h\nu - E_g) \qquad (6)$$

Where α is the absorption coefficient, hν is the photon energy, A is a constant, and n can either be 0.5 or 2 for a direct or indirect bandgap transition, respectively.

Table 4.4 summarises E_g values obtained from the linear fit in **Figure 4.9 (b)**. The as-prepared TiO_2 sample presents a direct bandgap energy of 3.03 eV [70]. Annealing of the as-prepared TiO_2 samples at 200, 400, 800, 1000, and 1200 °C reduces E_g significantly. This decrease in optical bandgap structure with the increase in T_a is associated with the expanding crystal structure discussed in XRD measurements. Thus, annealing of the multiphase TiO_2 samples shows successful tunability in metal oxide wide-bandgap structure.

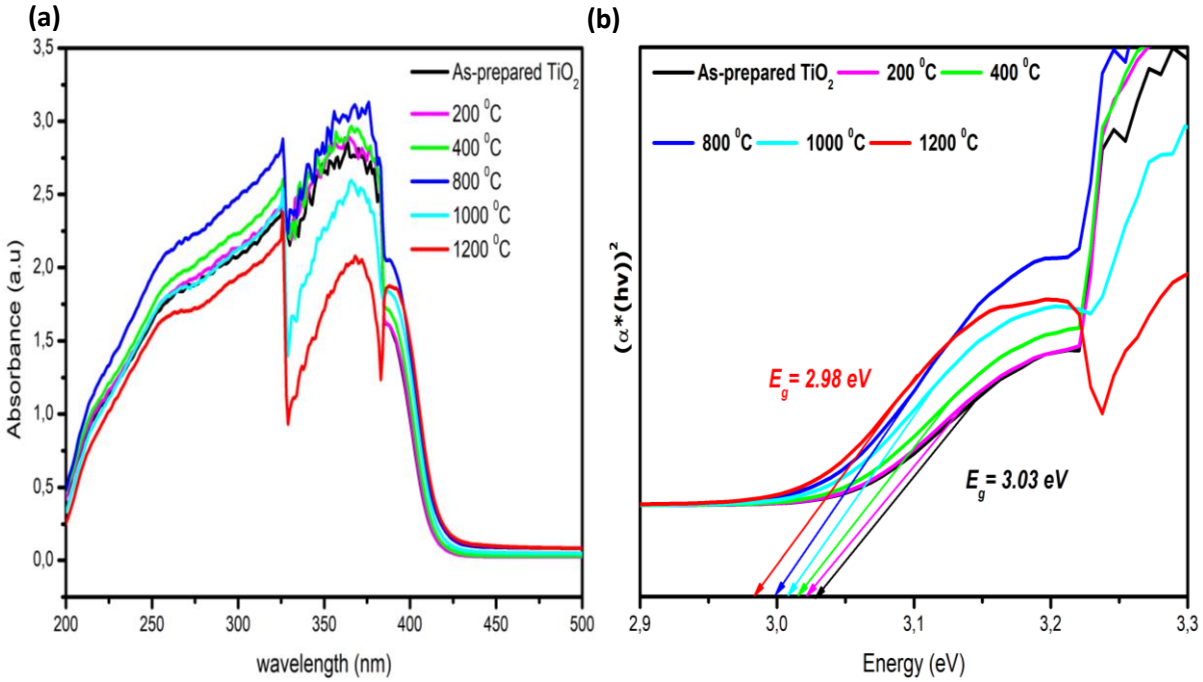

Figure 4.9: (a) Uv-vis absorption spectra and (b) bandgap energy estimates from a direct bandgap transition.

Table 4.4: Summary of bandgap energy determined from Figure 4.9 for the as-prepared and annealed TiO_2 samples.

Temperature (°C)	Bandgap E_g (eV)
As-prepared TiO_2	3.03
200	3.02
400	3.01
800	3.00
1000	3.01
1200	2.98

4.6 Conclusion

In this study mixed-phase, TiO_2 NPs which are termed multiphase TiO_2 NPs were synthesized by the hydrothermal preparation method. It is reported from literature studies that multiphase TiO_2 NPs that consist of a mixture of A and R-phase present inherent properties resulting in synergy. The obtained TiO_2 NPs were annealed at a temperature (T_a) range of 200 to 1200 °C. The samples were later placed under XRD, TEM, FE-SEM, EDX, FT-IR, and UV-Vis spectroscopy characterization to investigate the effect of T_a on structural, morphological, and optical properties in the multiphase TiO_2 material. The XRD analysis of the multiphase material exhibit good structural stability due to elevated A-R phase transition. TEM and SEM microscopic images show an excellent morphology with a promising interfacial contact point needed in solar cell applications. The microscopic images agree with XRD analysis showing an increase in crystallinity and porosity as T_a is increased. FT-IR and EDX confirmed successful synthesis. UV-Vis spectroscopy determines the optical properties of the multiphase TiO_2 material. It is observed that the material shows a UV absorption centred at 350 nm with an indirect wide-bandgap structure similar to rutile. This indicates that the multiphase TiO_2 material can be used as a blocking layer in photovoltaic (PV) devices that are susceptible to degradation by UV radiation. In addition, T_a tunes the material wide-bandgap which will, in turn, reduce recombination rates from narrow bandgap photoactive layers and thus increase PV efficiencies.

ACKNOWLEDGEMENTS

I acknowledge the South African National Research Foundation through the Thuthuka programme (Grant No: 121877) for the financial support throughout the course of the study. This work was not going to be successful without the financial assistance provided.

References

[1] Buddington, A.F. and Lindsley, D.H. (1964) Iron-titanium oxide minerals and synthetic equivalents. *Journal of Petrology*, **5**, pp.310-357. https://doi.org/10.1093/petrology/5.2.310

[2] Hoffmann, M.R., Martin, S.T., Choi, W. and Bahnemann, D.W. (1995) Environmental Applications of Semiconductor Photocatalysis. *Chemical Reviews*, **95**, pp.69-96. https://doi.org/10.1021/cr00033a004

[3] Reddy, K.M., Manorama, S. V. and Reddy, A.R. (2003) Bandgap studies on anatase titanium dioxide nanoparticles. *Materials Chemistry and Physics*, **78**, pp.239-245. https://doi.org/10.1016/S0254-0584(02)00343-7

[4] Chen, X. and Mao, S.S. (2007) Titanium dioxide nanomaterials: Synthesis, properties, modifications and applications. Chem. Rev. p. pp.2891-2959. https://doi.org/10.1021/cr0500535

[5] Ramimoghadam, D., Bagheri, S. and Abd Hamid, S.B. (2014) Biotemplated synthesis of anatase titanium dioxide nanoparticles via lignocellulosic waste material. *BioMed*

Research International, **2014**. https://doi.org/10.1155/2014/205636

[6] Peng, T., Zhao, D., Dai, K., Shi, W. and Hirao, K. (2005) Synthesis of titanium dioxide nanoparticles with mesoporous anatase wall and high photocatalytic activity. *Journal of Physical Chemistry B*, **109**, pp.4947-4952. https://doi.org/10.1021/jp044771r

[7] Shen, S., Chen, J., Wang, M., Sheng, X., Chen, X., Feng, X. et al. (2018) Titanium dioxide nanostructures for photoelectrochemical applications. Prog. Mater. Sci. p. pp.299-385. https://doi.org/10.1016/j.pmatsci.2018.07.006

[8] Yuan, S., Chen, W. and Hu, S. (2005) Fabrication of TiO2 nanoparticles/surfactant polymer complex film on glassy carbon electrode and its application to sensing trace dopamine. *Materials Science and Engineering C*, **25**, pp.479-485. https://doi.org/10.1016/j.msec.2004.12.004

[9] Schneider, J., Matsuoka, M., Takeuchi, M., Zhang, J., Horiuchi, Y., Anpo, M. et al. (2014) Understanding TiO 2 Photocatalysis: Mechanisms and Materials. **114**, pp.9919-9986. https://doi.org/10.1021/cr5001892

[10] Barbé, C.J., Arendse, F., Comte, P., Jirousek, M., Lenzmann, F., Shklover, V. et al. (1997) Nanocrystalline titanium oxide electrodes for photovoltaic applications. *Journal of the American Ceramic Society*, **80**, pp.3157-3171. https://doi.org/10.1111/j.1151-2916.1997.tb03245.x

[11] Joanni, E., Savu, R., de Sousa Góes, M., Bueno, P.R., de Freitas, J.N., Nogueira, A.F. et al. (2007) Dye-sensitized solar cell architecture based on indium-tin oxide nanowires coated with titanium dioxide. *Scripta Materialia*, **57**, pp.277-280. https://doi.org/10.1016/j.scriptamat.2007.03.051

[12] Wu, M., Lin, G., Chen, D., Wang, G., He, D., Feng, S. et al. (2002) Sol-hydrothermal synthesis and hydrothermally structural evolution of nanocrystal titanium dioxide. *Chemistry of Materials*, **14**, pp.1974-1980. https://doi.org/10.1021/cm0102739

[13] Nadzirah, S. and Hashim, U. (2013) Annealing effects on titanium dioxide films by Sol-Gel spin coating method. *Proceedings - RSM 2013: 2013 IEEE Regional Symposium on Micro and Nano Electronics*, p. 159–62. https://doi.org/10.1109/RSM.2013.6706497

[14] Rashidzadeh, M. (2008) Synthesis of high-thermal stable titanium dioxide nanoparticles. *International Journal of Photoenergy*, **2008**. https://doi.org/10.1155/2008/245981

[15] Swamy, V., Kuznetsov, A., Dubrovinsky, L.S., Caruso, R.A., Shchukin, D.G. and Muddle, B.C. (2005) Finite-size and pressure effects on the Raman spectrum of nanocrystalline anatase TiO2. *Physical Review B - Condensed Matter and Materials Physics*, **71**, p.184302. https://doi.org/10.1103/PhysRevB.71.184302

[16] Gupta, S.M. and Tripathi, M. (2011) A review of TiO2 nanoparticles. Chinese Sci. Bull. p. pp.1639-1657. https://doi.org/10.1007/s11434-011-4476-1

[17] Bai, Y., Mora-Seró, I., De Angelis, F., Bisquert, J. and Wang, P. (2014) Titanium dioxide nanomaterials for photovoltaic applications. Chem. Rev. p. pp.10095-10130. https://doi.org/10.1021/cr400606n

[18] Park, N.G., Van De Lagemaat, J. and Frank, A.J. (2000) Comparison of dye-sensitized rutile- and anatase-based TiO2 solar cells. *Journal of Physical Chemistry B*, **104**,

pp.8989-8994. https://doi.org/10.1021/jp994365l

[19] Liu, G., Yang, H.G., Pan, J., Yang, Y.Q., Lu, G.Q.M. and Cheng, H.M. (2014) Titanium dioxide crystals with tailored facets. Chem. Rev. p. pp.9559-9612. https://doi.org/10.1021/cr400621z

[20] Li, B., Wang, X., Yan, M. and Li, L. (2003) Preparation and characterization of nano-TiO2 powder. *Materials Chemistry and Physics*, **78**, pp.184-188. https://doi.org/10.1016/S0254-0584(02)00226-2

[21] Mohammed, A.A., Ahmad, A.S.S. and Azeez, W.A. (2015) Fabrication of Dye Sensitized Solar Cell Based on Titanium Dioxide (TiO2). *Advances in Materials Physics and Chemistry*, **05**, p.361. https://doi.org/10.4236/ampc.2015.59036

[22] Oh, H., Krantz, J., Litzov, I., Stubhan, T., Pinna, L. and Brabec, C.J. (2011) Comparison of various sol-gel derived metal oxide layers for inverted organic solar cells. *Solar Energy Materials and Solar Cells*, **95**, pp.2194-2199. https://doi.org/10.1016/j.solmat.2011.03.023

[23] Heo, J.H., Im, S.H., Noh, J.H., Mandal, T.N., Lim, C.S., Chang, J.A. et al. (2013) Efficient inorganic-organic hybrid heterojunction solar cells containing perovskite compound and polymeric hole conductors. *Nature Photonics*, **7**, pp.486-491. https://doi.org/10.1038/nphoton.2013.80

[24] Harizanov, O. and Harizanova, A. (2000) Development and investigation of sol-gel solutions for the formation of TiO2 coatings. *Solar Energy Materials and Solar Cells*, **63**, pp.185-195. https://doi.org/10.1016/S0927-0248(00)00008-8

[25] Sarah, M.S.P., Musa, M.Z., Asiah, M.N. and Rusop, M. (2010) Electrical conductivity characteristics of TiO2 thin film. *2010 International Conference on Electronic Devices, Systems and Applications, ICEDSA 2010 - Proceedings*, p. 361–4. https://doi.org/10.1109/ICEDSA.2010.5503040

[26] Hanaor, D.A.H. and Sorrell, C.C. (2011) Review of the anatase to rutile phase transformation. J. Mater. Sci. p. pp.855-874. https://doi.org/10.1007/s10853-010-5113-0

[27] Muthee, D.K. and Dejene, B.F. (2021) Effect of annealing temperature on structural, optical, and photocatalytic properties of titanium dioxide nanoparticles. *Heliyon*, **7**, p.e07269. https://doi.org/10.1016/j.heliyon.2021.e07269

[28] Bakri, A.S., Sahdan, M.Z., Adriyanto, F., Raship, N.A., Said, N.D.M., Abdullah, S.A. et al. (2017) Effect of annealing temperature of titanium dioxide thin films on structural and electrical properties. *AIP Conference Proceedings*, p. 030030. https://doi.org/10.1063/1.4968283

[29] Khalid Hossain, M., Pervez, M.F., Mia, M.N.H., Tayyaba, S., Jalal Uddin, M., Ahamed, R. et al. (2017) Annealing temperature effect on structural, morphological and optical parameters of mesoporous TiO2 film photoanode for dye-sensitized solar cell application. *Materials Science- Poland*, **35**, pp.868-877. https://doi.org/10.1515/msp-2017-0082

[30] Sarode, M.T., Shelke, P.N., Gunjal, S.D., Khollam, Y.B., Takwale, M.G., Jadkar, S.R. et al. (2012) Effect of annealing temperature on optical properties of titanium dioxide thin films prepared by sol-gel method. *International Journal of Modern Physics:*

Conference Series, **06**, pp.13-18. https://doi.org/10.1142/s2010194512002863

[31] Lian, Q., Mokhtar, M.Z., Lu, D., Zhu, M., Jacobs, J., Foster, A.B. et al. (2020) Using Soft Polymer Template Engineering of Mesoporous TiO2Scaffolds to Increase Perovskite Grain Size and Solar Cell Efficiency. *ACS Applied Materials and Interfaces*, **12**, pp.18578-18589. https://doi.org/10.1021/acsami.0c02248

[32] Mechiakh, R., Sedrine, N. Ben, Naceur, J. Ben and Chtourou, R. (2011) Elaboration and characterization of nanocrystalline TiO2 thin films prepared by sol-gel dip-coating. *Surface and Coatings Technology*, **206**, pp.243-249. https://doi.org/10.1016/j.surfcoat.2011.06.053

[33] Kim, D.J., Hahn, S.H., Oh, S.H. and Kim, E.J. (2002) Influence of calcination temperature on structural and optical properties of TiO2 thin films prepared by sol-gel dip coating. *Materials Letters*, **57**, pp.355-360. https://doi.org/10.1016/S0167-577X(02)00790-5

[34] Andronic, L., Andrasi, D., Enesca, A., Visa, M. and Duta, A. (2011) The influence of titanium dioxide phase composition on dyes photocatalysis. *Journal of Sol-Gel Science and Technology*, **58**, pp.201-208. https://doi.org/10.1007/s10971-010-2378-3

[35] Yun, T.K., Park, S.S., Kim, D., Shim, J.H., Bae, J.Y., Huh, S. et al. (2012) Effect of the rutile content on the photovoltaic performance of the dye-sensitized solar cells composed of mixed-phase TiO2 photoelectrodes. *Dalton Transactions*, **41**, pp.1284-1288. https://doi.org/10.1039/c1dt11765c

[36] Guimarães, R.R., Parussulo, A.L.A., Toma, H.E. and Araki, K. (2016) Enlightening the synergic effect of anatase/rutile mixtures in solar cells. *Electrochimica Acta*, **188**, pp.523-528. https://doi.org/10.1016/j.electacta.2015.12.040

[37] Li, G., Richter, C.P., Milot, R.L., Cai, L., Schmuttenmaer, C.A., Crabtree, R.H. et al. (2009) Synergistic effect between anatase and rutile TiO2 nanoparticles in dye-sensitized solar cells. *Dalton Transactions*, pp.10078-10085. https://doi.org/10.1039/B908686B

[38] Malevu, T.D., Mwankemwa, B.S., Motloung, S. V., Tshabalala, K.G. and Ocaya, R.O. (2019) Effect of annealing temperature on nano-crystalline TiO2 for solar cell applications. *Physica E: Low-Dimensional Systems and Nanostructures*, **106**, pp.127-132. https://doi.org/10.1016/j.physe.2018.10.028

[39] Ntsikelelo, M.P., Thembinkosi, M.D., Koao, L.F., Setumo, M. V. and Tshwafo, M.E. (2020) Transformation from anatase to rutile titania using hydrothermal method: Investigation of morphology and thermal stability. *Sensors and Materials*, **32**, pp.1511-1522. https://doi.org/10.18494/SAM.2020.2649

[40] Sönmezoğlu, S., Çankaya, G. and Serin, N. (2012) Phase transformation of nanostructured titanium dioxide thin films grown by sol-gel method. *Applied Physics A: Materials Science and Processing*, **107**, pp.233-241. https://doi.org/10.1007/s00339-011-6749-6

[41] Cano-Casanova, L., Amorós-Pérez, A., Lillo-Ródenas, M.Á. and Román-Martínez, M. del C. (2018) Effect of the preparation method (sol-gel or hydrothermal) and conditions on the TiO2 properties and activity for propene oxidation. *Materials*, **11**, p.2227. https://doi.org/10.3390/ma11112227

[42] Li, G., Ciston, S., Saponjic, Z. V., Chen, L., Dimitrijevic, N.M., Rajh, T. et al. (2008) Synthesizing mixed-phase TiO2 nanocomposites using a hydrothermal method for photo-oxidation and photoreduction applications. *Journal of Catalysis*, **253**, pp.105-110. https://doi.org/10.1016/j.jcat.2007.10.014

[43] Wang, C.C. and Ying, J.Y. (1999) Sol-gel synthesis and hydrothermal processing of anatase and rutile titania nanocrystals. *Chemistry of Materials*, **11**, pp.3113-3120. https://doi.org/10.1021/cm990180f

[44] Matthews, A. (1976) The crystallization of anatase and rutile from amorphous titanium dioxide under hydrothermal conditions. *American Mineralogist*, **61**, pp.419-424.

[45] Ohno, T., Sarukawa, K., Tokieda, K. and Matsumura, M. (2001) Morphology of a TiO2 photocatalyst (Degussa, P-25) consisting of anatase and rutile crystalline phases. *Journal of Catalysis*, **203**, pp.82-86. https://doi.org/10.1006/jcat.2001.3316

[46] Xiong, Z., Wu, H., Zhang, L., Gu, Y. and Zhao, X.S. (2014) Synthesis of TiO2 with controllable ratio of anatase to rutile. *Journal of Materials Chemistry A*, **2**, pp.9291-9297. https://doi.org/10.1039/c4ta01144a

[47] Muniz, E.C., Góes, M.S., Silva, J.J., Varela, J.A., Joanni, E., Parra, R. et al. (2011) Synthesis and characterization of mesoporous TiO2 nanostructured films prepared by a modified sol-gel method for application in dye solar cells. *Ceramics International*, **37**, pp.1017-1024. https://doi.org/10.1016/j.ceramint.2010.11.014

[48] Wei, X., Zhu, G., Fang, J. and Chen, J. (2013) Synthesis, characterization, and photocatalysis of well-dispersible phase-pure anatase TiO2 nanoparticles. *International Journal of Photoenergy*, **2013**. https://doi.org/10.1155/2013/726872

[49] Mahmoud, H.A., Narasimharao, K., Ali, T.T. and Khalil, K.M.S. (2018) Acidic peptizing agent effect on anatase-rutile ratio and photocatalytic performance of TiO2 nanoparticles. *Nanoscale Research Letters*, **13**, pp.1-13. https://doi.org/10.1186/s11671-018-2465-x

[50] Alsaiari, M.A., Alhemiary, N.A., Umar, A. and Hayden, B.E. (2020) Growth of amorphous, anatase and rutile phase TiO2 thin films on Pt/TiO2/SiO2/Si (SSTOP) substrate for resistive random access memory (ReRAM) device application. *Ceramics International*, **46**, pp.16310-16320. https://doi.org/10.1016/j.ceramint.2020.03.188

[51] Zhang, H. and Banfield, J.F. (2014) Structural characteristics and mechanical and thermodynamic properties of nanocrystalline TiO2. Chem. Rev. p. pp.9613-9644. https://doi.org/10.1021/cr500072j

[52] Diebold, U. (2003) The surface science of titanium dioxide. Surf. Sci. Rep. p. pp.53-229. https://doi.org/10.1016/s0167-5729(02)00100-0

[53] Yang, T.Y., Lin, H.M., Wei, B.Y., Wu, C.Y. and Lin, C.K. (2003) UV enhancement of the gas sensing properties of nano-TiO2. *Reviews on Advanced Materials Science*, **4**, pp.48-54.

[54] Byrne, C., Fagan, R., Hinder, S., McCormack, D.E. and Pillai, S.C. (2016) New approach of modifying the anatase to rutile transition temperature in TiO2 photocatalysts. *RSC Advances*, **6**, pp.95232-95238. https://doi.org/10.1039/c6ra19759k

[55] Sabyrov, K., Burrows, N.D. and Penn, R.L. (2013) Size-dependent anatase to rutile phase transformation and particle growth. *Chemistry of Materials*, **25**, pp.1408-1415.

https://doi.org/10.1021/cm302129a

[56] Selman, A.M. and Husham, M. (2016) Calcination induced phase transformation of TiO2 nanostructures and fabricated a Schottky diode as humidity sensor based on rutile phase. *Sensing and Bio-Sensing Research*, **11**, pp.8-13. https://doi.org/10.1016/j.sbsr.2016.09.003

[57] Pal, M., Serrano, J.G., Santiago, P. and Pal, U. (2007) Size-controlled synthesis of spherical TiO2 nanoparticles: Morphology, crystallization, and phase transition. *Journal of Physical Chemistry C*, **111**, pp.96-102. https://doi.org/10.1021/jp0618173

[58] Zhou, W., Gai, L., Hu, P., Cui, J., Liu, X., Wang, D. et al. (2011) Phase transformation of TiO2 nanobelts and TiO 2(B)/anatase interface heterostructure nanobelts with enhanced photocatalytic activity. *CrystEngComm*, **13**, pp.6643-6649. https://doi.org/10.1039/c1ce05638g

[59] Spurr, R.A. and Myers, H. (1957) Quantitative Analysis of Anatase-Rutile Mixtures with an X-Ray Diffractometer. *Analytical Chemistry*, **29**, pp.760-762. https://doi.org/10.1021/ac60125a006

[60] Ding, X.Z. and Liu, X.H. (1998) Correlation between anatase-to-rutile transformation and grain growth in nanocrystalline titania powders. *Journal of Materials Research*, **13**, pp.2556-2559. https://doi.org/10.1557/JMR.1998.0356

[61] SHI, L. and WENG, D. (2008) Highly active mixed-phase TiO2 photocatalysts fabricated at low temperatureand the correlation between phase compositionand photocatalytic activity. *Journal of Environmental Sciences*, **20**, pp.1263-1267. https://doi.org/10.1016/S1001-0742(08)62219-6

[62] Baiju, K. V., Zachariah, A., Shukla, S., Biju, S., Reddy, M.L.P. and Warrier, K.G.K. (2009) Correlating photoluminescence and photocatalytic activity of mixed-phase nanocrystalline titania. *Catalysis Letters*, **130**, pp.130-136. https://doi.org/10.1007/s10562-008-9798-5

[63] Prasad, K., Pinjari, D. V., Pandit, A.B. and Mhaske, S.T. (2010) Phase transformation of nanostructured titanium dioxide from anatase-to-rutile via combined ultrasound assisted sol-gel technique. *Ultrasonics Sonochemistry*, **17**, pp.409-415. https://doi.org/10.1016/j.ultsonch.2009.09.003

[64] Ahmad, M.K., Rasheid, N.A., Ahmed, A.Z., Abdullah, S. and Rusop, M. (2008) Effect of Annealing Temperature on Titanium Dioxide Thin Films Prepared by Sol Gel Method. **1017**, pp.109-113. https://doi.org/10.1063/1.2940607

[65] Zhao, Y., Li, C., Liu, X., Gu, F., Jiang, H., Shao, W. et al. (2007) Synthesis and optical properties of TiO2 nanoparticles. *Materials Letters*, **61**, pp.79-83. https://doi.org/10.1016/j.matlet.2006.04.010

[66] Bagheri, S., Shameli, K. and Abd Hamid, S.B. (2013) Synthesis and characterization of anatase titanium dioxide nanoparticles using egg white solution via Sol-Gel method. *Journal of Chemistry*, **2013**. https://doi.org/10.1155/2013/848205

[67] Pulišová, P., Boháček, J., Šubrt, J., Szatmáry, L., Bezdička, P., Večerníková, E. et al. (2010) Thermal behaviour of titanium dioxide nanoparticles prepared by precipitation from aqueous solutions. *Journal of Thermal Analysis and Calorimetry*, p. pp.607-613. https://doi.org/10.1007/s10973-010-0893-7

[68] Mugundan, S., Rajamannan, B., Viruthagiri, G., Shanmugam, N., Gobi, R. and Praveen, P. (2015) Synthesis and characterization of undoped and cobalt-doped TiO2 nanoparticles via sol–gel technique. *Applied Nanoscience (Switzerland)*, **5**, pp.449-456. https://doi.org/10.1007/s13204-014-0337-y

[69] Luttrell, T., Halpegamage, S., Tao, J., Kramer, A., Sutter, E. and Batzill, M. (2015) Why is anatase a better photocatalyst than rutile? - Model studies on epitaxial TiO2 films. *Scientific Reports*, **4**, pp.1-8. https://doi.org/10.1038/srep04043

[70] Scanlon, D.O., Dunnill, C.W., Buckeridge, J., Shevlin, S.A., Logsdail, A.J., Woodley, S.M. et al. (2013) Band alignment of rutile and anatase TiO2. *Nature Materials*, **12**, pp.798-801. https://doi.org/10.1038/nmat3697

Chapter 5

Investigating the Morphology, Optical, and Thermal properties of Multiphase-TiO_2/$MAPbI_3$ Heterogeneous Thin-Films for Solar Cell Applications.

5.1 Overview

In this chapter multiphase TiO_2 nanoparticles were used in the fabrication of perovskite solar cells to investigate the effect of annealing TiO_2/phase composition on device performance. The TiO_2 nanopowders were synthesized by hydrothermal and annealed from 200 to 1200 ℃ as described in the previous chapter. The calculated anatase and rutile phase ratio in the multiphase TiO_2 nanoparticles is estimated to be 68/32, 65/35, 46/54, 60/40, 36/64, 34/66 for the as-prepared TiO_2 and annealed TiO_2 samples at 200, 400, 800, 1000, and 1200 ℃, respectively. The nanoparticles possess a mesoporous surface structure. Increasing the annealing temperature brings about changes in material merit properties such as porosity, particle size, crystallinity, and optical properties. Without any further treatment, heterogeneous thin films of TiO_2/$MAPbI_3$ were fabricated and characterized by scanning electron microscopy (SEM), fourier transform infrared spectroscopy (FT-IR), thermogravimetric analysis (TGA), and Photoluminescence spectroscopy (PL). The final devices were assembled by a simple and unique technique using conductive silver ink as a counter electrode. SEM micrographs and corresponding EDX images investigate $MAPbI_3$ crystal formation on the mesoporous TiO_2 surface structure. EDX spectra reveal excellent qualitative and quantitative analysis corresponding to the SEM images in the TiO_2/$MAPbI_3$ heterogeneous thin films. TGA characterization reveals that the TiO_2/$MAPbI_3$ thin films are thermally stable recording a maximum of 15.7 % mass loss at 800 ℃ elevated temperatures. PL characterizes the effect of multiphase TiO_2 phase transformation on the TiO_2/$MAPbI_3$ recombination efficiencies. A maximum of 6% power conversion efficiency is achieved for devices with an active area of $3x10^{-4}$ m^2 demonstrating that the synthesized multiphase TiO_2 nanoparticles are promising for large surface area manufacturing.

5.2 Introduction

P and N-type semiconducting transition metal oxides are extensively studied and put in use in third-generation solar cells ranging from dye-sensitized solar cells (DSSCs), quantum dot solar cells (QDSCs), organic solar cells (OSCs), and perovskite solar cells (PSCs) [1–3]. Thin films of TiO_2, ZnO, V_2O_5, MoO, CuO, NiO_2 are used due to their nanostructural properties to facilitate charge extraction and transport from photoactive hybrid materials [4–7]. The mesoporous structure in titanium dioxide (TiO_2) makes TiO_2 a successful n-type photoanode

electrode in photovoltaics (PVs). This unique TiO_2 morphology appears to serve as a host/absorber matrix for light active materials on its surface in DSSCs, QDSCs, and PSCs which increases the metal oxide/light active material intermediate contact [8,9]. Tailoring the structure, morphology, and optical properties of metal oxides is key to optimizing the performance of solar cell devices [10–12]. Changes in TiO_2 merit properties such as phase composition, degree of crystallinity, porosity, crystalline size, particle size, and bandgap structure are significant to improve hybrid solar cell's photocurrent, open-circuit voltage, and energy conversion efficiencies.

Similar to DSSCs, TiO_2 thin films are coated over conductive glass substrates, annealed, and stained with a light-sensitive ABX_3 perovskite material in PSCs. The annealing process is known to transform TiO_2 into a crystalline and conductive electron transport layer (ETL), remove residual impurities, precursor solvents, and encourage brookite, anatase, and rutile phase formation. In addition, significant research has demonstrated that annealing alters TiO_2 merit properties which subsequently influence the metal oxide/light active interface properties [13,14]. In PVs anatase TiO_2 is the most preferred phase due to its higher open-circuit voltage, photoactivity, and surface area than rutile-based PV cells [15]. An important concept that has not received much attention is the use of mixed-phase (anatase: rutile) TiO_2 nanoparticles (NPs) in PSCs. Extensive research on mixed-phase TiO_2 photoanode has been carried out in DSSCs. The majority of these studies observe synergy at less than 20% rutile phase formation [16,17]. Material characterization results reveal that changes in phase composition bring about changes in TiO_2 merit properties such as crystallinity, morphology, and optical properties of the photoanode [18]. Similar changes in this work are already discussed in chapter 4 and are included in chapter 5 to demonstrate the influence of multiphase-TiO_2 ETL on PSCs performance. Existing studies on mixed-phase TiO_2 achieve phase composition through a mixture of two-phase different titanium precursors (e.g., P25 and P90), the addition of phase controlling agents/additives (e.g., CH_3COOH, EDTA, and $(NH_4)_2SO$), and annealing TiO_2 NPs [16,17,19–21]. Li *et al* [17] fabricated mixed-phase TiO_2 photoelectrodes based on phase pure anatase and rutile TiO_2. The author's results demonstrate that the addition of small rutile phase content into anatase enhances the photoelectrode absorption coefficient improving the photocurrent density and efficiency in comparison to the phase pure PV cells. In an additional study, Yun *et al* [16] prepared mixed-phase TiO_2 NPs by $(NH_4)_2SO_2$ hydrolysis. The concentration of the sulfate ion successfully tunes anatase and rutile phase composition. The author's characterization results indicate that the improved photocurrent and efficiencies in comparison to pure phase devices are attributed to high light scattering by large rutile particles. However, large amounts of rutile phase content decrease surface area and as a consequence dramatically reduce the device's performance. In a similar research work, Ruan *et al* [19] supplement the explanation of synergy in mixed-phase TiO_2 by symbiosis in anatase and rutile surface morphologies which facilitates maximum interparticle charge transfer.

The above synthesis of mixed-phase TiO_2 NPs results in two distinctive rod-like and spherical morphologies associated with rutile and anatase phases, respectively, with rutile morphology relative to anatase decreasing solar cell performances due to its low surface area and packing structure both phenomena decreasing the electron collection in the devices. Therefore, in this study mesoporous multiphase-TiO_2 NPs are used to investigate the influence of phase composition on PSC performance. The phase transformation is achieved through annealing TiO_2 NPs from 200 to 1200 ℃. Scanning electron microscopy coupled with energy-dispersive

x-ray spectroscopy (SEM-EDX) was used to investigate the perovskite $MAPbI_3$ crystal formation and interaction with TiO_2 ETL. Fourier transform infrared spectroscopy (FT-IR) was used to confirm functional groups within the multiphase-TiO_2/$MAPbI_3$ heterogeneous thin films. Thermogravimetric analysis (TGA) was used to determine the thermal behavior and confirm the existence of heterogeneous TiO_2 and $MAPbI_3$ mixture from the TGA degradations steps within a temperature range of 0 to 800 ℃. Photoluminescence spectroscopy (PL) was used to study recombination efficiencies. The increasing TiO_2 particle size and rutile phase increase photoexcitation and efficient electron extraction from the $MAPbI_3$ light active material. A detailed explanation on the effect of annealing/phase composition on the PSC IV performance is given. Maximum efficiency of up to 6.7% is reported, attributed to factors discussed in SEM and PL.

5.3 Methods

5.3.1 Perovskite solar cell (PSCs) device fabrication

ITO glass substrates (Sigma-Aldrich) were first cleaned with a detergent and ultrasonicated three times using water, isopropanol, and ethanol for 20 minutes separately. The glass substrates were later allowed to dry at ambient atmosphere thereafter subjected to UV-Ozone cleaning for a period of 15 minutes. To form a dense compact TiO_2 blocking layer, the UV-Ozone cleaned substrates were coated with a 0.15 M titanium diisopropoxide bis(acetylacetonate) (75% in isopropanol, Sigma-Aldrich) in 1-butanol by spin-coating at 2000 rpm for 20s which were then heated at 100 ℃ for 5 min. After the coated glass substrates were allowed to cool at room temperature the process was repeated two times using a 0.3 M titanium diisopropoxide bis(acetylacetonate). Following the three-times coating of titanium diisopropoxide bis(acetylacetonate) the glass substrates were then heated at 250 ℃ for 15 minutes and allowed to cool at room temperature. A few micrometer thick layer of mesoporous-TiO_2 photoelectrode was formed from a paste of the synthesized TiO_2 from the previous chapter. Pastes of TiO_2 were obtained by dissolving the synthesized and annealed TiO_2 nanopowders in ethanol (Sigma-Aldrich). The micrometer thick layers were coated over the compact layer using the doctor blade technique thereafter the substrates were heated at 250 ℃ for 45 minutes. From here the substrates/photoelectrodes were treated with a 0.02 M $TiCl_4$ (98%, Sigma-Aldrich) solution maintained at 80 ℃ for 10 minutes, washed with deionized water, and dried at 100 ℃ in an open atmosphere. A single halide perovskite layer of $CH_3NH_3PbI_3$-($MAPbI_3$) was formed by two-step spin coating of PbI_2 and MAI at ambient conditions (relative humidity= 45-60%) to form TiO_2/$MAPbI_3$ heterogeneous thin films. Firstly, a solution of 0.02 ml of 1 M PbI_2 (4.61g) in a solvent mixture of DMF: DMSO (3:1) prepared at 70 ℃ was spin-coated over the mesoporous TiO_2 layers at 3000 rpm for 10s without loading time. The ITO/c-TiO_2/m-TiO_2/PbI_2 glass substrates were then dried at 100 ℃ for 10 minutes and allowed to cool to room temperature. The perovskite layer was completed by spin-coating 0.2 ml of 0.038 M CH_3NH_3I at 4000 rpm for 20s with a loading time of 20s. The ITO/c-TiO_2/m-TiO_2/$MAPbI_3$ glass substrates were then dried at 100 ℃ for 10 minutes. A 0.02 ml solution of spiro-MeOTAD was spin-coated over the perovskite bearing substrated at 3500 rpm for 35s. The spiro-MeOTAD deposited solution was obtained by dissolving 0.072g of spiro-MeOTAD (Sigma-Aldrich) in 1 ml chlorobenzene (Sigma-Aldrich) solvent. This was followed

by the addition of 0.029 ml 4-*tert*-butyl pyridine (Sigma-Aldrich) and 0.018 ml (0.52g) lithium bis(trifluoromethanesulfonyl)imide in 1 ml acetonitrile (Sigma-Aldrich) solutions. The counter electrode was obtained by using silver (Ag) ink on an opposite ITO substrate. Approximately 80 % of the ITO substrate was covered with a deposition mask and a conductive Ag ink (Sigma-Aldrich) was deposited over the exposed area via doctor blade technique. The solar cells were assembled by preheating the TiO_2 coated substrates at 100 ℃ for 5 minutes thereafter clamped with the opposite Ag coated electrodes. The fabricated cells were then heated at 100 ℃ for 15 minutes to form solar cells with device architecture of ITO/c-TiO_2/m-TiO_2/$MAPbI_3$/Ag/ITO. A total of six (6) devices are reported by varying only the mesoporous TiO_2 electron transport layer and remaining layers are kept constant. For consistency the resulting devices were designated as follows:

Table 5.1: Solar cell naming.

Devices
As-prep TiO_2/$MAPbI_3$
200 ℃/$MAPbI_3$
400 ℃/$MAPbI_3$
800 ℃/$MAPbI_3$
1000 ℃/$MAPbI_3$
1200 ℃/$MAPbI_3$

5.4 Characterization

To determine the surface morphology of TiO_2/$MAPbI_3$ heterogeneous thin-films, a TESCAN VEGAN3 scanning electron microscopy (OXFORD X-MAX^N) coupled with EDX operated at 20 kv was used and the analysis was done at room temperature. The surface of the samples was sputter-coated with carbon for 9.9s to produce conductive coating onto the samples. To characterize the thermal behavior of the samples Perkin-Elmer STA6000 thermogravimetric analyzer (TGA) was used. 20-25 mg of the photoanode/perovskite was obtained by scraping the TiO_2/$MAPbI_3$ heterogeneous thin films off the ITO conductive substrate. The samples were heated at 10 ℃min^{-1} from ambient to 800 ℃ under 20 mLmin^{-1}nitrogen flow. A Perkin-Elmer Spectrum 100 Fourier-transform infrared (FT-IR) spectroscope fitted with an attenuated total reflection (ATR) detector, FT-IR spectrometer was used in this study to identify functional groups in the TiO_2/$MAPbI_3$ heterogeneous thin films. The infrared (IR) spectra were recorded between 4000 and 650 cm^{-1} at a resolution of 4 cm^{-1}. Photoluminescence spectroscopy (PL) characterization was performed on as-prepared TiO_2 nanopowder, annealed TiO_2 nanopowder, and TiO_2/$MAPbI_3$ heterogeneous films under a Carry Eclipse Fluorescence spectrophotometer with a 150W xenon lamp (λ_{ex}= 238 nm). The electrical properties of the final devices with an active area of 3 cm^2 = 3x10^{-4} m^2 were measured using Newport Oriel LCS-100 solar simulator and Keithley source meter (Keithley 2450) under AM1.5G and 1000 W/m^2 standard irradiation test conditions calibrated from a standard Si-based solar cell.

5.5 Results and discussion

5.5.1 Scanning Electron Microscopy

Figure 5.1 (a) to (f) shows low magnification SEM surface morphology of the as-prep TiO_2/$MAPbI_3$ and annealed heterogeneous thin films, respectively. The two-step method results in the formation of perovskite crystals. The surface images depict that annealing the multiphase-TiO_2 nanopowder has a strong influence on $MAPbI_3$ crystals formation over the TiO_2 surface structure. The images show two distinctive morphologies; (1) nanometer-sized TiO_2 NPs and (2) relatively large $MAPbI_3$ crystals. Similar perovskite crystal morphology is reported by Christians *et al* [22] from the two-step $MAPbI_3$ deposition method. It is observed that the increased annealing temperature in the multiphase-TiO_2 NPs encourages a non-uniform $MAPbI_3$ crystal dispersion increasing the distribution over the nanoporous TiO_2 surface. Im *et al* [23] demonstrated comparable perovskite crystal growth. From all the SEM images the $MAPbI_3$ crystals are of the same size due to the consistent preparation method.

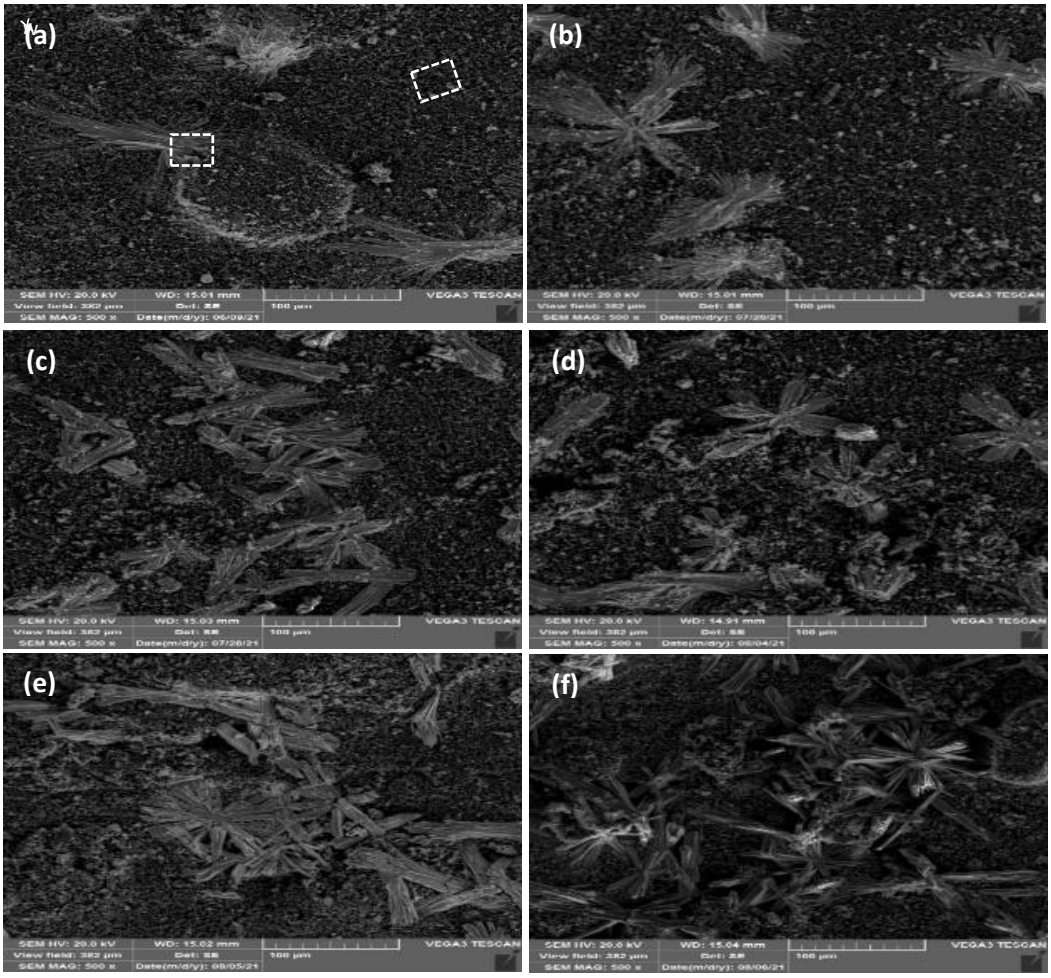

Figure 5.1: Low magnification SEM micrographs presenting the surface morphology of the (a) As-prep TiO_2/$MAPbI_3$, (b) 200°C/$MAPbI_3$ (c) 400°C/$MAPbI_3$, (d) 800°C/$MAPbI_3$, (e) 1000°C/$MAPbI_3$, and (f) 1200°C/$MAPbI_3$ heterogeneous thin-films.

Figure 5.2 shows high magnification SEM micrographs and the corresponding SEM-EDX micrographs of TiO_2/$MAPbI_3$ heterogeneous thin-films used to investigate $MAPbI_3$ crystal formation onto the mesoporous TiO_2 NPs on a particular/selected region marked by white dotted squares in **Figure 5.1 (a)**. The observed morphology from the magnified SEM image in **Figure 5.2 (a)** shows an incomplete or initial stage of perovskite crystal formation. This is confirmed by the corresponding SEM-EDX micrograph presented in **Figure 5.2 (b)** demonstrating the presence of C, Pb, and I perovskite main elements. The EDX image illustrates that the $MAPbI_3$ precursor solutions successfully penetrated TiO_2 pores subsequently crystallizing towards the mesoporous TiO_2 surface during the evaporation of the deposition solvents, charging up TiO_2 NPs at localized sites. A similar ETL and light active material interaction have been previously reported for low light absorption coefficient dye molecules over nanoporous TiO_2 photoanode by Hossain *et al* [24]. It is anticipated in this study that the TiO_2 surface charging leads to possible perovskite nucleating (or crystallization) sites depending on the $MAPbI_3$ surface charging density leading to the heterogeneous morphology shown in **Figure 5.2 (c)** illustrating a cluster of crystals emerging from the surface of the TiO_2 nanoporous host material. Based on the observed $MAPbI_3$ crystal morphology it is noted that there exists a preferred $MAPbI_3$ orientated crystal growth that propagates away from a fixed point source justifying the proposed localized nucleating sites discussed above.

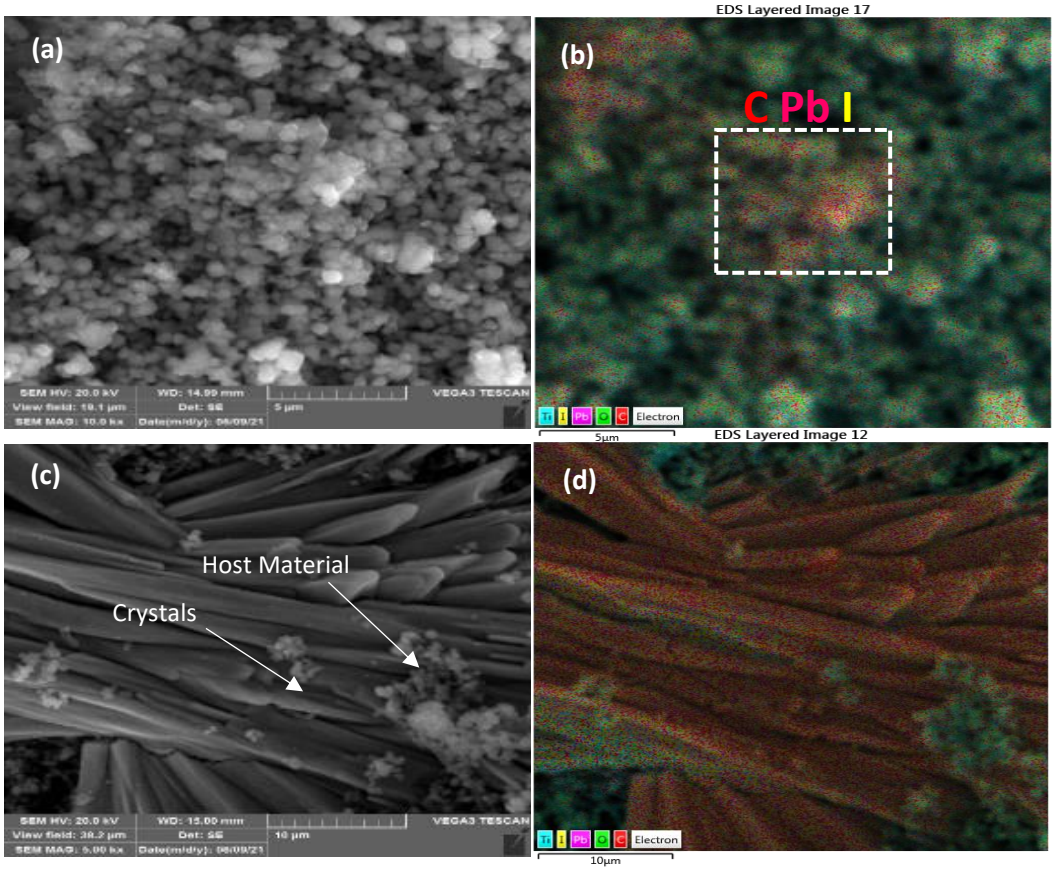

Figure 5.2: High magnification SEM micrographs illustrating (a) surface morphology of As-prep TiO_2/$MAPbI_3$ interaction on ITO substrate, corresponding (b) SEM-EDX mapping image, (c) heterogeneous morphology interaction of $MAPbI_3$ nanocrystals embedded within TiO_2 nanopores, and corresponding (d) SEM-EDX image.

The EDX peak position (keV) and intensities (cps/eV) values provide excellent qualitative and quantitative analysis of the elements present in the TiO_2/$MAPbI_3$ heterogeneous thin films respectively consistent with SEM surface analysis.

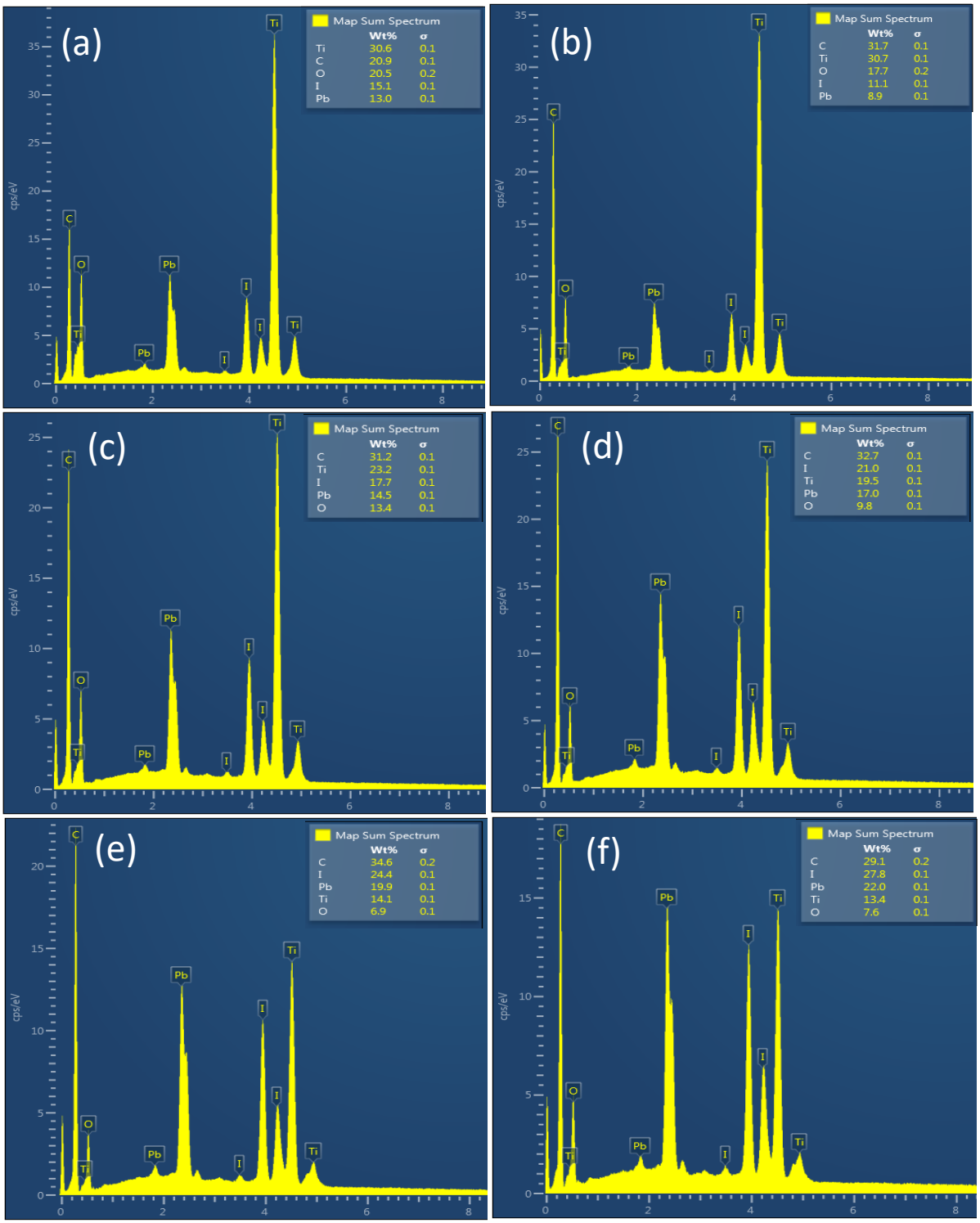

Figure 5.3: EDX spectra for the as prep TiO_2/$MAPbI_3$ (a), 200°C/$MAPbI_3$ (b), 400°C/$MAPbI_3$ (c), 800°C/$MAPbI_3$ (b), 1000°C/$MAPbI_3$ (b), and 1200°C/$MAPbI_3$ heterogeneous thin films.

5.5.2 Fourier Transform Infrared Spectroscopy

FT-IR spectroscopy was used to investigate the compatibility between the TiO_2 NPs and $MAPbI_3$ crystal in the heterogeneous thin films. The activity of the IR-spectra was recorded between 4000 to 500 wavenumber regions. Vibrational modes from the heterogeneous thin films centered at 2902, 2804, 1703, and 709 cm^{-1} were identified and correlated with SEM surface images in **Figure 5.1**. The large absorption bands located at low annealing temperatures at 2902, 2804, and 1703 cm^{-1} are associated with low compatibility between the TiO_2 NPs and $MAPbI_3$ crystals. However, these vibrational bands systematically decrease with increasing TiO_2 annealing temperature, indicating that the interface contact compatibility in the heterogeneous thin films is improved, this can be successfully correlated with the increase in surface coverage from the SEM images. The appearance of a new vibrational mode located at 709 cm^{-1} substantiates enhanced compatibility indicating that a good interface contact has been established.

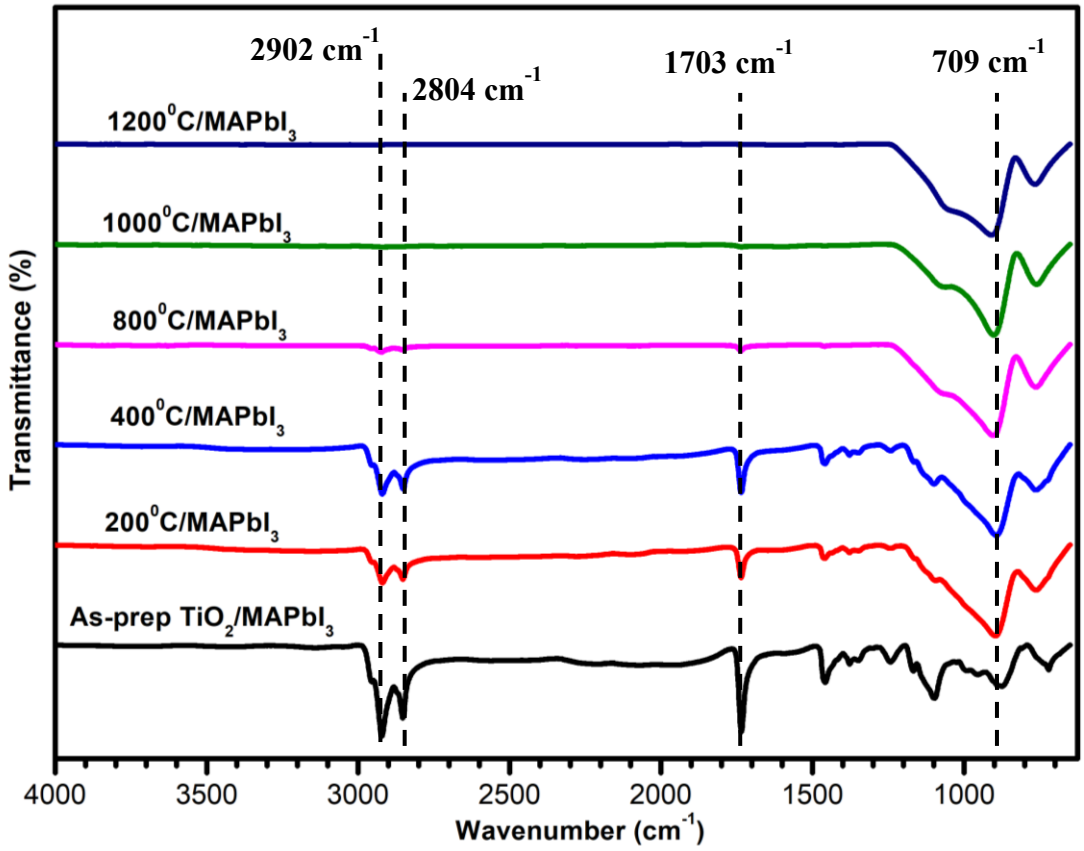

Figure 5.4: FT-IR spectra of the heterogeneous $TiO_2/MAPbI_3$ thin films.

5.5.3 Thermogravimetric Analysis

To understand the thermal behavior and determine the degradation steps from the TiO_2/$MAPbI_3$ perovskite heterogeneous thin films TGA analysis was performed by heating the samples from ambient temperature to 800 ℃ in triplicate, average values are reported in **Table 5.2**. From the percentage mass loss in **Figure 5.5 (a)** it is apparent that all the heterogeneous thin films are thermally stable, recording a maximum mass loss percentage of 15.7% at high temperatures of up to 800 ℃. The as-prep TiO_2/$MAPbI_3$ heterogeneous thin films experience the highest mass loss, recording a final residual mass % at 84.3%. The remaining heterogeneous thin films increase systematically with increasing annealing temperature, exhibiting mass residues greater than 84.3%. A minimum of 2.2% mass loss is recorded for the 1200 ℃/$MAPbI_3$ heterogeneous thin films. This shows that annealing of the TiO_2 nanopowder removes temperature-initiated degrading agents, resulting in thermally stable heterogeneous films. This observation is further depicted by the decreasing peak intensities in the DTGA graphs of **Figure 5.5 (b)**. This systematic increase in the residual mass % in the heterogeneous films is further correlated to the TiO_2 phase transformation. TiO_2 NPs are naturally characterized by thermal transitions from the metastable phases to the stable rutile phase. Therefore, samples annealed at higher temperatures possess the thermodynamically stable rutile phase, whereas samples at lower annealing temperature are metastable anatase phase. Hence the 2.2% mass loss belongs to the heterogeneous samples bearing more stable-TiO_2 NPs. In **Figure 5.5 (a)** (TGA) and **(b)** (DTGA), TiO_2/$MAPbI_3$ heterogeneous thin films decompose through three degradation mechanisms located at temperatures ≥ 106, 438, and 513 ℃. The first and small degradation step located at ~106 ℃ is associated with the evaporation of absorbed water molecules on the surface of TiO_2 NPs, the second degradation step approximated at 438 ℃ is associated with the characteristic TiO_2 anatase to rutile phase transition [25]. As expected in both events, the mass loss % is significantly reduced with increasing annealing temperature as outlined above and summarized in **Table 5.2**. The third degradation step results from the decomposition of the $MAPbI_3$ perovskite by desorption of volatile MAI organic group [26].

Table 5.2: Presents DTGA peak temperatures, TGA degradation steps, and total mass loss from the TiO_2/$MAPbI_3$ heterogeneous thin films.

Samples	Degradation steps			Total Average mass (%) loss
	H_2O evaporation	A-R phase transition	MAI volatilization	
DTGA Temperatures (℃)	≥ 106.2	≥ 437.5	≥ 512.5	-
As-pre TiO_2/$MAPbI_3$	1.7%	9.5%	4.5%	15.7%
200/$MAPbI_3$	0.5%	8.3%	4.4%	13.2%
400/$MAPbI_3$	0%	6.9%	2.8%	9.7%
800/$MAPbI_3$	0%	4.5%	1.9%	6.4%
1000/$MAPbI_3$	0%	3.5%	1.2%	4.7%
1200/$MAPbI_3$	0%	1.8%	0.4%	2.2%

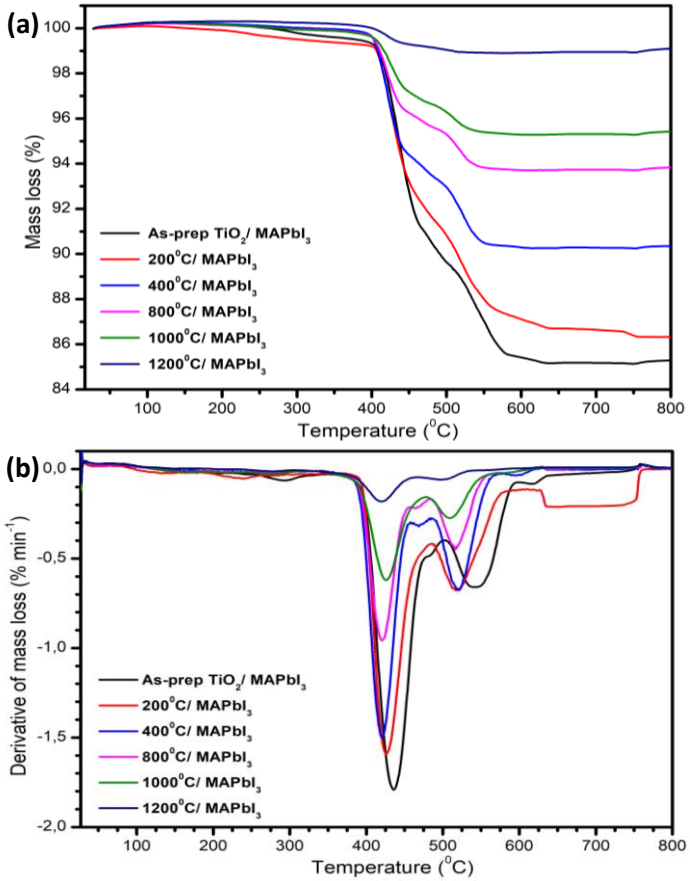

Figure 5.5: (a) TGA and (b) DTGA graphs present the effect of annealing TiO_2 NPs on the thermal degradation behavior of the resulting TiO_2/$MAPbI_3$ heterogeneous thin films.

5.5.4 Photoluminescence Spectroscopy

Photoluminescence (PL) is used to characterize photogenerated recombination pathways caused by defect levels within the bandgap structure of a semiconductor and the resulting PL peak emissions indicate the recombination of excitons, electrons, and holes between the conduction band and valence band. TiO_2 NPs are characterized by PL peak emissions caused by oxygen vacancies, surface states, free and bound exciton recombinations [20,21,27]. The emission spectra in **Figure 5.6 (a), (b), and (c)** present PL peak emissions in 300-700 nm range obtained from the excitation wavelength of λ_{ex}= 238 nm for the a-prep TiO_2 nanopowder **(a)**, annealed TiO_2 nanopowders **(b)**, and as-prep TiO_2/$MAPbI_3$ and annealed heterogeneous thin films **(c)**. The peak emissions were analyzed to investigate the effect of annealing/phase transformation on the recombination efficiencies. The deconvoluted gaussian fit for the as-prep TiO_2 nanopowder in **Figure 5.6 (a)** shows characteristic peak emissions centered at λ_{em}= 426, 466, 501, and 537 nm, a similar PL spectrum has previously been reported by Tsega *et al* [27] and Acchutharaman *et al* [21]. The prominent emissions located at 426 and 466 nm are associated with the oxygen vacancy and surface state dominant defect levels in the TiO_2 forbidden gap, whereas the shoulder peak emissions at high wavelengths of 501 and 537 nm are associated with the free edge and bound exciton minority recombinations. **Figure 5.6 (b)** demonstrates the effect of annealing multiphase-TiO_2 on the material's recombination rates,

insert of **Figure 5.6 (b**) (normalized peak intensities) presents similar peak emissions reported in **Figure 5.6 (a)** indicating that throughout the annealing process the peak emissions result from intrinsic trapping sites within the forbidden gap of multiphase-TiO_2. From **Figure 5.6 (b)** it is observed that by increasing annealing temperature, the multiphase-TiO_2 NPs undergo PL quenching. This is observed by the decreasing trend in peak intensities determined as follows from the samples: as-prep TiO_2 → 200 ℃ → 400 ℃ indicating that the intrinsic recombination rates (or concentration of defect levels) from oxygen vacancies, surface states, and excitons are significantly reduced, similar observation has been reported by Fan *et al* [20] in mixed-phase TiO_2 NPs and is ascribed to the increase in TiO_2 degree of crystallinity and the desorption of oxygen molecules reducing TiO_2 dominant defect levels. However, with a further increase in annealing temperature, a counteractive phenomenon emerges substantially increasing the peak intensities dramatically. This apparent change in behavior from the PL peak emissions is attributed to the multiphase-TiO_2 phase transition and an increase in TiO_2 particle size. Comparable results are reported by Yun *et al* [16] and Ruan *et al* [19] demonstrating that more rutile phase formation and large particle size results in a low electron mobile phase and increased light-scattering, respectively. Providing an efficient charge carrier recombination pathway.

Figure 5.6 (c) depicts PL peak emissions from the as-prep TiO_2/$MAPbI_3$ and annealed heterogeneous thin films. A new dominant peak emission in all the heterogeneous films located at 540 nm appears, this shows that an intermediate contact is established between the ETLs and the light active material, therefore such recombination rate is attributed to TiO_2 ETL and $MAPbI_3$ interface electron decaying pathway. For comparison, it is observed that all the maximum peak intensities of the TiO_2/$MAPbI_3$ heterogeneous thin films are significantly reduced when compared to the maximum peak intensity of the as-prep TiO_2 nanopowder reported in **Figure 5.6 (a)** indicating that the incorporation of the light active $MAPbI_3$ perovskite material encourages maximum electron collection as a result of minimum photon emissions. A systematic decrease in TiO_2/$MAPbI_3$ PL peak emission is observed with increasing annealing temperature/rutile phase content. This unusual trend highlights synergy from the multiphase-TiO_2 material influencing the overall photogenerated electron collection. The synergy results from the large photon scattering caused by the large particle size which contributes to large photoexcitation in the perovskite material.

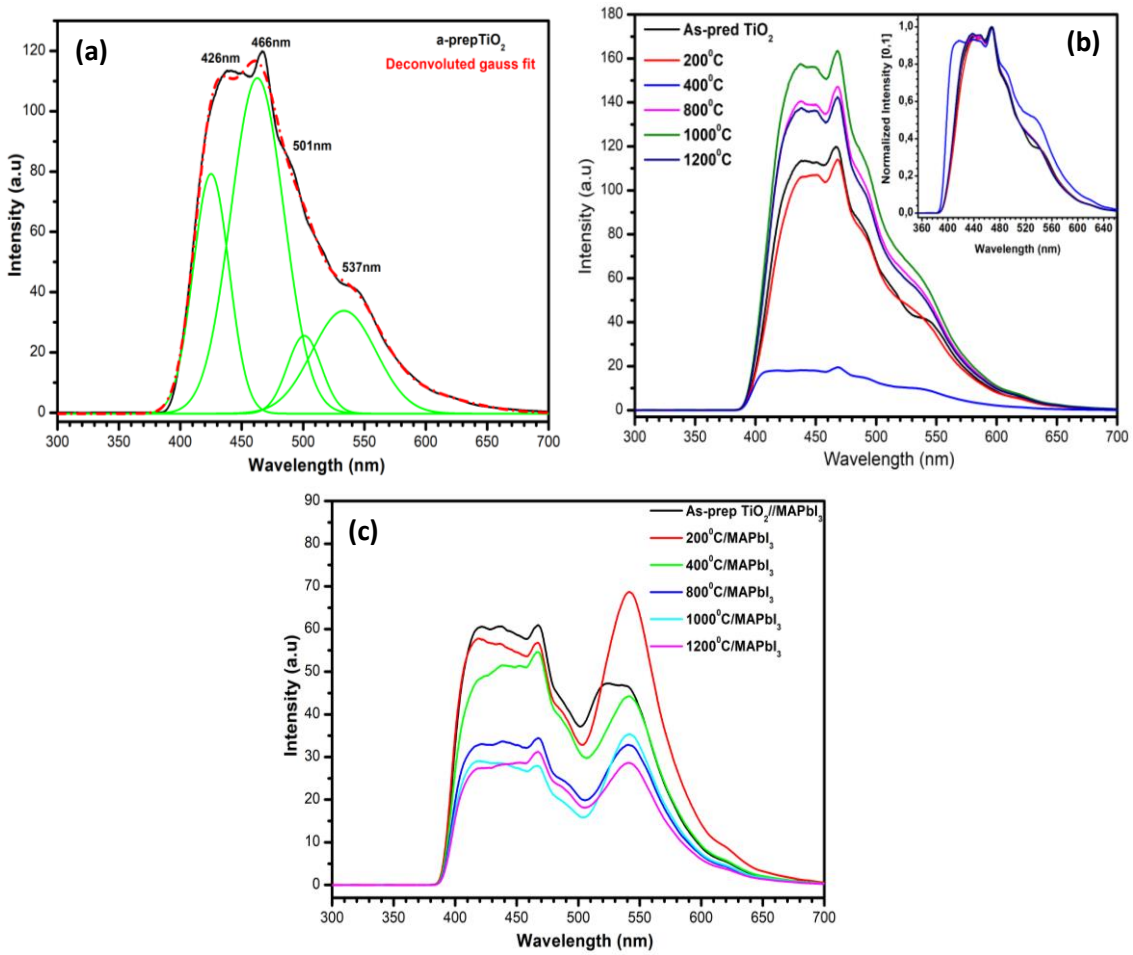

Figure 5.6: Presents PL peak emissions of the (a) as-prep TiO_2 nanopowder, (b) annealed TiO_2 nanopowders, and (c) as-prep TiO_2/$MAPbI_3$ and annealed heterogeneous thin films at λ_{ex}= 238 nm excitation wavelength.

5.5.5 Electrical Characterization

Figure 5.7 depicts a simplified schematic image of the devices. **Figure 5.8** shows IV characterization curves measured under AM1.5G and 1000 W/m^2 standard illumination conditions. **Table 5.3** summarizes electrical average parameter values with standard deviations from the three best cells for each sample. The power conversion efficiency of the devices given in **Table 5.3** is calculated from **equation 1**. From the IV curves in **Figure 5.8** and **Table 5.3,** it is observed that there is a prominent increase in current density (J_{sc}) and power conversion efficiency (η) from the PSCs with increasing rutile phase content and annealing temperature. This observation is correlated with the increasing $MAPbI_3$ surface coverage morphology (SEM) over the large multiphase-TiO_2 NPs, and the evident decrease in photoluminescence emissions (PL) in **Figure 5.6 (c),** resulting in enhanced J_{sc} and η. This indicates that the increase in the rutile phase establishes an efficient electron transfer from the photoexcited perovskite material into the conduction band of the anatase phase. A maximum of 6.7% efficiency is achieved for the solar cells fabricated from the 1000 °C/$MAPbI_3$ heterogeneous thin films. Therefore the IV characterization demonstrates that although the rutile phase is characterized

by slow electron mobility resulting in increased multiphase-TiO_2 recombination rates as shown in **Figure 5.6 (b)** the increasing PSC performance with increasing rutile content demonstrates that rutile is a high electron harvesting phase that extracts maximum photogenerated electrons from the perovskite material into the more electron mobile anatase phase decreasing the recombinations as shown by **Figure 5.6 (c)**. This is followed by a significant decrease to 5.1% efficiencies as rutile becomes the more dominant phase indicating that phase optimization in the multiphase-TiO_2 NPs is required for optimal PSC performances.

$$\eta = \frac{V_{oc}.J_{sc}.FF}{P_{in}} = \frac{V_{oc}.J_{sc}.FF}{A.1000\ W/m} \quad (1)$$

Equation 1 is used in the calculation of the power conversion efficiency (η), whereby V_{oc} represents open-circuit voltage, J_{sc} represents short circuit current density, FF represents the fill factor, A represents the active area of the solar cells, and P_{in} represents the maximum power from the solar simulator lamp.

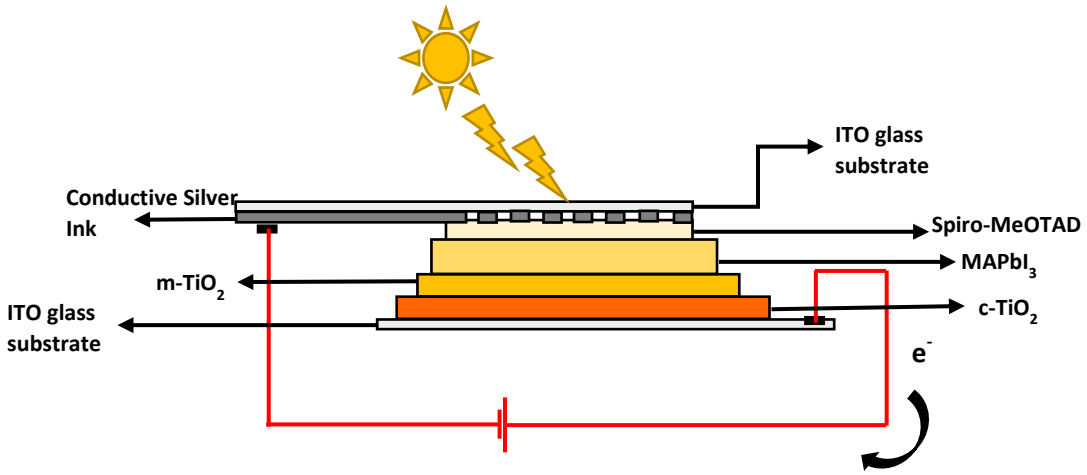

Figure 5.7: Schematic representation of the fabricated solar cell with device architecture ITO/c-TiO_2/m-TiO_2/$MAPbI_3$/Spiro-MeoTAD/Conductive Ag ink/ITO.

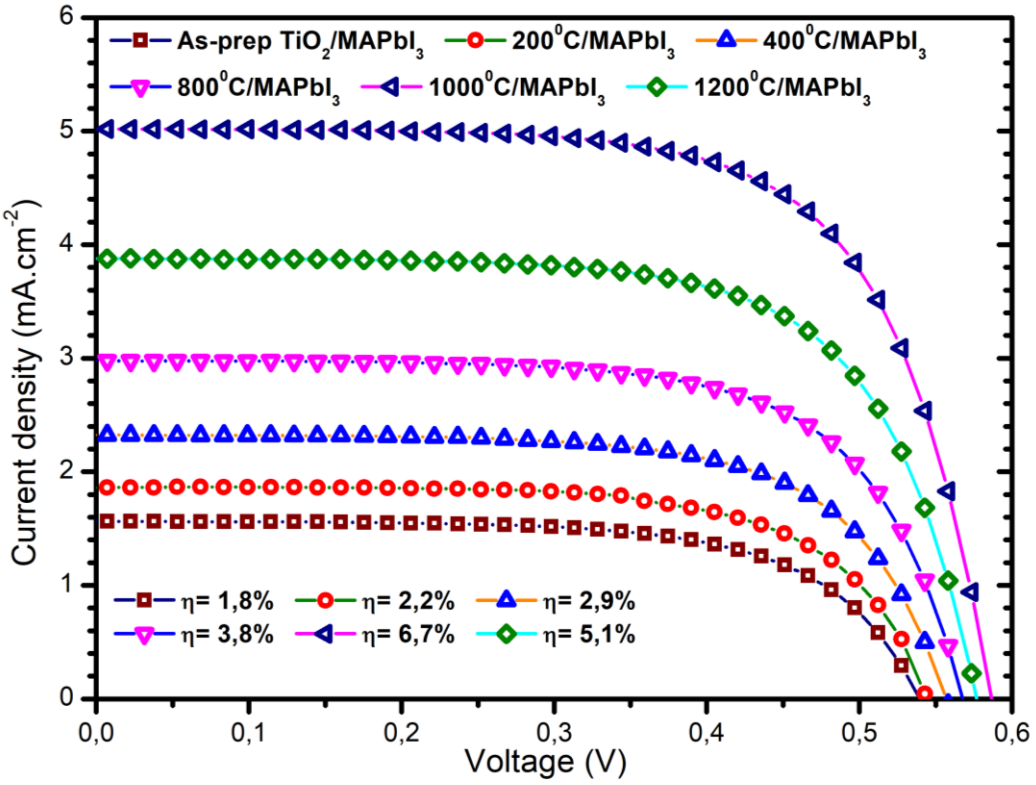

Figure 5.8: IV characterization curves.

Table 5.3: Photovoltaic parameters for the PSCs with device architecture ITO/c-TiO_2/m-TiO_2/$MAPbI_3$/Spiro-MeoTAD/Conductive Ag ink/ITO.

Device	Phase composition (A/R)	V_{oc} (V)	J_{sc} ($mA.cm^{-2}$)	FF (%)	η (%)
As-pre TiO_2/$MAPbI_3$	68/32	0.53 ±0.02	1.57 ±0.15	65.7 ±0.028	1.82 ±0.55
200/$MAPbI_3$	65/35	0.54 ±0.02	1.86 ±0.13	66.5 ±0.015	2.22 ±0.42
400/$MAPbI_3$	46/54	0.56 ±0.02	2.31 ±0.11	66.8 ±0.023	2.88 ±0.58
800/$MAPbI_3$	60/40	0.57 ±0.02	2.98 ±0.18	67.4 ±0.021	3.82 ±0.72
1000/$MAPbI_3$	36/64	0.59 ±0.02	5.02 ±0.16	68.1 ±0.025	6.72 ±0.68
1200/$MAPbI_3$	34/66	0.58 ±0.02	3.89 ±0.17	68.0 ±0.018	5.11 ±0.64

5.6 Conclusion

In this study, the use of multiphase TiO_2 nanoparticles proved to be an excellent mediator for maximum electron collection of the light-active $MAPbI_3$ perovskite material to the ITO glass substrate. Heterogeneous thin films of TiO_2 and $MAPbI_3$ for solar cells were successfully fabricated from doctor blade and two-step spin coating methods. The morphology, compatibility, thermal, and optical properties of the multiphase $TiO_2/MAPbI_3$ thin films were carefully characterized by scanning electron microscopy (SEM), Fourier transform infrared spectroscopy (FT-IR), thermogravimetric analysis (TGA), and photoluminescence spectroscopy (PL). SEM surface imaging indicates that the increase in annealing temperature from the multiphase-TiO_2 NPs encourages a non-uniform $MAPbI_3$ crystal dispersion increasing the surface coverage over the nanoporous TiO_2. SEM-EDX micrographs of $TiO_2/MAPbI_3$ heterogeneous thin-films were further used to study the $MAPbI_3$ crystal formation onto the mesoporous TiO_2 NPs. The SEM-EDX micrographs reveal that the $MAPbI_3$ crystal formation mechanism involved TiO_2 pore filling (nucleation) followed by crystallization (growth) during the evaporation of the deposition solvents. FT-IR spectroscopy was used to study the interface compatibility between TiO_2 NPs and $MAPbI_3$ crystals. A good correlation is observed between FT-IR vibrational modes and $MAPbI_3$ surface coverage discussed in SEM surface images. Increasing annealing enhances the interface contact between TiO_2 NPs and $MAPbI_3$ crystals. TGA was used to determine the thermal behavior in the $TiO_2/MAPbI_3$ perovskite heterogeneous thin films. The thermal analysis reveals that the $TiO_2/MAPbI_3$ thin films are thermally stable recording a maximum of 15.7 % mass loss at elevated temperatures. PL spectroscopy was used to study the effect of annealing on recombination efficiencies of TiO_2 NPs and the fabricated $TiO_2/MAPbI_3$ heterogeneous thin films. The formation of an interface contact between the TiO_2 and perovskite was further observed by the formation of a new dominant PL peak emission in all the heterogeneous films. A systematic decrease in $TiO_2/MAPbI_3$ PL peak emission is observed with increasing annealing temperature/rutile phase content. This unusual trend highlights synergy from the multiphase-TiO_2 material influencing the overall photogenerated electron collection. Finally, perovskite solar cells of device structure ITO/c-TiO_2/m-TiO_2/$MAPbI_3$/Spiro-MeoTAD/Conductive Ag ink/ITO were fabricated and their performance was evaluated using the Keithley solar simulator. A maximum of 6.7% efficiency is achieved for the solar cells fabricated from the 1000 ℃/$MAPbI_3$ heterogeneous thin films.

Reference

[1] Kojima, A., Teshima, K., Shirai, Y. and Miyasaka, T. (2009) Organometal Halide Perovskites as Visible-Light Sensitizers for Photovoltaic Cells. UTC. **10**, 43. https://doi.org/10.1021/ja809598r

[2] O'Regan, B. and Grätzel, M. (1991) A low-cost, high-efficiency solar cell based on dye-sensitized colloidal TiO2 films. *Nature*, **353**. https://doi.org/10.1038/353737a0

[3] Im, J.-H., Lee, C.-R., Lee, J.-W., Park, S.-W. and Park, N.-G. 6.5% efficient perovskite quantum-dot-sensitized solar cell †. https://doi.org/10.1039/c1nr10867k

[4] Tiwana, P., Docampo, P., Johnston, M.B., Snaith, H.J. and Herz, L.M. (2011) Electron mobility and injection dynamics in mesoporous ZnO, SnO 2, and TiO2 films used in dye-sensitized solar cells. *ACS Nano*, **5**. https://doi.org/10.1021/nn201243y

[5] Arbab, E.A.A. and Mola, G.T. (2016) V2O5 thin film deposition for application in organic solar cells. *Applied Physics A: Materials Science and Processing*, **122**. https://doi.org/10.1007/s00339-016-9966-1

[6] Hou, Y., Du, X., Scheiner, S., McMeekin, D.P., Wang, Z., Li, N. et al. (2017) A generic interface to reduce the efficiency-stability-cost gap of perovskite solar cells. *Science*, **358**. https://doi.org/10.1126/science.aao5561

[7] Juma, A.O., Arbab, E.A.A., Muiva, C.M., Lepodise, L.M. and Mola, G.T. (2017) Synthesis and characterization of CuO-NiO-ZnO mixed metal oxide nanocomposite. *Journal of Alloys and Compounds*, **723**. https://doi.org/10.1016/j.jallcom.2017.06.288

[8] Choi, J.J., Yang, X., Norman, Z.M., Billinge, S.J.L. and Owen, J.S. (2014) Structure of methylammonium lead iodide within mesoporous titanium dioxide: Active material in high-performance perovskite solar cells. *Nano Letters*, **14**. https://doi.org/10.1021/nl403514x

[9] Zukalovà, M., Zukal, A., Kavan, L., Nazeeruddin, M.K., Liska, P. and Grätzel, M. (2005) Organized mesoporous TiO2 films exhibiting greatly enhanced performance in dye-sensitized solar cells. *Nano Letters*, **5**. https://doi.org/10.1021/nl051401l

[10] Kumar, S.S., Rubio, E.J., Noor-A-Alam, M., Martinez, G., Manandhar, S., Shutthanandan, V. et al. (2013) Structure, morphology, and optical properties of amorphous and nanocrystalline gallium oxide thin films. *Journal of Physical Chemistry C*, **117**. https://doi.org/10.1021/jp311300e

[11] Chen, X. and Mao, S.S. (2007) Titanium dioxide nanomaterials: Synthesis, properties, modifications and applications. Chem. Rev. p. pp.2891-2959. https://doi.org/10.1021/cr0500535

[12] Park, N.G., Van De Lagemaat, J. and Frank, A.J. (2000) Comparison of dye-sensitized rutile- and anatase-based TiO2 solar cells. *Journal of Physical Chemistry B*, **104**, pp.8989-8994. https://doi.org/10.1021/jp994365l

[13] Hsu, C.H., Chen, K. Te, Huang, P.H., Wu, W.Y., Zhang, X.Y., Wang, C. et al. (2020) Effect of annealing temperature on spatial atomic layer deposited titanium oxide and its application in perovskite solar cells. *Nanomaterials*, **10**. https://doi.org/10.3390/nano10071322

[14] Malevu, T.D., Mwankemwa, B.S., Motloung, S. V., Tshabalala, K.G. and Ocaya, R.O. (2019) Effect of annealing temperature on nano-crystalline TiO2 for solar cell applications. *Physica E: Low-Dimensional Systems and Nanostructures*, **106**, pp.127-132. https://doi.org/10.1016/j.physe.2018.10.028

[15] Cahen, D., Hodes, G., Grätzel, M., Guillemoles, J.F. and Riess, I. (2000) Nature of Photovoltaic Action in Dye-Sensitized Solar Cells. *Journal of Physical Chemistry B*, **104**. https://doi.org/10.1021/jp993187t

[16] Yun, T.K., Park, S.S., Kim, D., Shim, J.H., Bae, J.Y., Huh, S. et al. (2012) Effect of the rutile content on the photovoltaic performance of the dye-sensitized solar cells composed of mixed-phase TiO2 photoelectrodes. *Dalton Transactions*, **41**, pp.1284-

1288. https://doi.org/10.1039/c1dt11765c

[17] Li, G., Richter, C.P., Milot, R.L., Cai, L., Schmuttenmaer, C.A., Crabtree, R.H. et al. (2009) Synergistic effect between anatase and rutile TiO2 nanoparticles in dye-sensitized solar cells. *Dalton Transactions*, pp.10078-10085. https://doi.org/10.1039/B908686B

[18] Sengupta, D., Das, P., Mondal, B. and Mukherjee, K. (2016) Effects of doping, morphology and film-thickness of photo-anode materials for dye sensitized solar cell application - A review. Renew. Sustain. Energy Rev. https://doi.org/10.1016/j.rser.2016.01.104

[19] Ruan, P., Qian, J., Xu, Y., Xie, H., Shao, C. and Zhou, X. (2013) Mixed-phase TiO2 nanorods assembled microsphere: Crystal phase control and photovoltaic application. *CrystEngComm*, **15**. https://doi.org/10.1039/c3ce40351c

[20] Fan, Y.H., Ho, C.Y. and Chang, Y.J. (2017) Enhancement of dye-sensitized solar cells efficiency using mixed-phase TiO2 nanoparticles as photoanode. *Scanning*, **2017**. https://doi.org/10.1155/2017/9152973

[21] Acchutharaman, K.R., Santhosh, N., Isaac Daniel, R., Senthil Pandian, M. and Ramasamy, P. (2021) Enhanced electron harvesting in next generation solar cells by employing TiO2 nanoparticles prepared through hydrolysis catalytic process. *Ceramics International*,. https://doi.org/10.1016/j.ceramint.2021.04.131

[22] Christians, J.A., Miranda Herrera, P.A. and Kamat, P. V. (2015) Transformation of the excited state and photovoltaic efficiency of CH3NH3PbI3 perovskite upon controlled exposure to humidified air. *Journal of the American Chemical Society*, **137**. https://doi.org/10.1021/ja511132a

[23] Im, J.H., Jang, I.H., Pellet, N., Grätzel, M. and Park, N.G. (2014) Growth of CH3 NH3 PbI3 cuboids with controlled size for high-efficiency perovskite solar cells. *Nature Nanotechnology*, **9**, 927–32. https://doi.org/10.1038/nnano.2014.181

[24] Hossain, M.K., Pervez, M.F., Mia, M.N.H., Mortuza, A.A., Rahaman, M.S., Karim, M.R. et al. (2017) Effect of dye extracting solvents and sensitization time on photovoltaic performance of natural dye sensitized solar cells. *Results in Physics*, **7**. https://doi.org/10.1016/j.rinp.2017.04.011

[25] Pulišová, P., Boháček, J., Šubrt, J., Szatmáry, L., Bezdička, P., Večerníková, E. et al. (2010) Thermal behaviour of titanium dioxide nanoparticles prepared by precipitation from aqueous solutions. *Journal of Thermal Analysis and Calorimetry*, p. pp.607-613. https://doi.org/10.1007/s10973-010-0893-7

[26] Dang, Y., Liu, Y., Sun, Y., Yuan, D., Liu, X., Lu, W. et al. (2015) Bulk crystal growth of hybrid perovskite material CH3NH3PbI3. *CrystEngComm*, **17**. https://doi.org/10.1039/c4ce02106a

[27] Tsega, M. and Dejene, F.B. (2017) Influence of acidic pH on the formulation of TiO2 nanocrystalline powders with enhanced photoluminescence property. *Heliyon*, **3**. https://doi.org/10.1016/j.heliyon.2017.e00246

.